



저작자표시-비영리 2.0 대한민국

이용자는 아래의 조건을 따르는 경우에 한하여 자유롭게

- 이 저작물을 복제, 배포, 전송, 전시, 공연 및 방송할 수 있습니다.
- 이차적 저작물을 작성할 수 있습니다.

다음과 같은 조건을 따라야 합니다:



저작자표시. 귀하는 원저작자를 표시하여야 합니다.



비영리. 귀하는 이 저작물을 영리 목적으로 이용할 수 없습니다.

- 귀하는, 이 저작물의 재이용이나 배포의 경우, 이 저작물에 적용된 이용허락조건을 명확하게 나타내어야 합니다.
- 저작권자로부터 별도의 허가를 받으면 이러한 조건들은 적용되지 않습니다.

저작권법에 따른 이용자의 권리는 위의 내용에 의하여 영향을 받지 않습니다.

이것은 [이용허락규약\(Legal Code\)](#)을 이해하기 쉽게 요약한 것입니다.

[Disclaimer](#)



공학박사 학위논문

고용량 층상구조 산화물 및 유기 화합물
리튬 이차전지 양극 소재에 관한 연구

**High-capacity layered oxides and organic compounds as
cathode materials for lithium rechargeable batteries**

2015년 2월

서울대학교 대학원

재료공학부

홍 지 현

고용량 층상구조 산화물 및 유기 화합물 리튬 이차전지 양극 소재에 관한 연구

지도 교수 강 기 석

이 논문을 공학박사 학위논문으로 제출함
2015년 2월

서울대학교 대학원
재료공학부
홍지현

홍지현의 박사 학위논문을 인준함
2015년 2월

위원장 박병우 (인)

부위원장 강기석 (인)

위원 남기태 (인)

위원 박찬범 (인)

위원 조성백 (인)

Abstract

High-capacity layered oxides and organic compounds as cathode materials for lithium rechargeable batteries

Jihyun Hong

Department of Materials Science and Engineering

The Graduate School

Seoul National University

Lithium rechargeable batteries power most portable electronic devices mainly due to their capability of offering the high energy density compared to other energy storage systems. Recently, the large-scale applications of lithium rechargeable batteries such as electric vehicles (EVs) and stationary power backups have moved in the center of interests coinciding with the large demands on the sustainable energy storage technologies. However, the currently available lithium rechargeable batteries are not sufficient for the large-scale applications in terms of the energy density, cost, life time, and safety. To address this issue, intensive scientific efforts have been made in exploring new cathode materials that can substitute current cathode materials including LiCoO_2 and LiFePO_4 .

Among various cathode materials reported so far, layered Li-excess transition metal oxides and organic compounds have received wide attention of the materials scientists due to their capability of reversibly storing and

delivering large quantity of energy in the small weight of the compounds. Despite their high energy density, the energy storage mechanisms of the layered Li-excess nickel-manganese oxides and organic compounds are not clearly understood yet. The lack of understanding on the materials makes the origin of poor electrochemical performances such as power capability and cycle stability more ambiguous and limits their practical applications. In this respect, here, in-depth study is performed to understand the energy storage mechanisms of the high-capacity electrode materials by using the combination of experimental analyses and DFT calculations. Furthermore, the strategies to improve their battery performances are demonstrated.

The layered Li-excess transition metal oxides exhibit large capacity (~230 mAh g⁻¹) which exceeds the amount of available redox couples in the pristine compounds when they are charged to high voltage beyond the plateau at 4.5~4.6 V accompanied with oxygen gas evolution. Moreover, this class of materials suffers gradual voltage decay during repeated electrochemical cycling. However, the detailed reactions of oxygen in the batteries after the first charge process and the origins of the voltage decay have not been clearly revealed. In this thesis, the role and effects of oxygen evolved from the layered Li-excess transition metal oxides during electrochemical cycling are proposed and the strategy to protect the surface of electrode materials from the acidic byproducts was briefly introduced. Furthermore, it is proposed that the compositional optimization of the Li-excess compounds effectively suppress the voltage decay increasing the energy storage efficiency.

The organic compounds have a great potential to achieve large specific capacity due to the absence of the heavy transition metal ions in their structure

and the capability of multi-electron transfer. Inspired by the biologically occurring redox-active organic cofactors incorporated in the sequential energy transduction reactions, here I propose a new class organic electrode compounds. The organic compounds containing pteridine redox center are demonstrated as sustainable cathode materials: flavin-derivatives. Through the computational material design, I have discovered the simpler compounds containing pteridine redox moiety which are alloxazine and lumazine. Furthermore, a strategy is proposed for optimizing the electrochemical performances of these biological redox units achieving excellent rate capability and cycle stability.

Keywords: Lithium rechargeable batteries, cathode, positive electrodes, layered, Li-excess, organic electrodes

Student Number: 2011-30195

Contents

Chapter 1 Introduction	1
1.1 Motivation and outlines	1
1.2 References	4
Chapter 2 Layered Li-excess nickel-manganese oxides	6
2.1 Role of oxygen evolution from layered Li-excess nickel-manganese oxides	6
2.1.1 Research background	6
2.1.2 Experimental details	8
2.1.3 Results and discussion	10
2.1.4 Conclusion	34
2.1.5 References	38
2.2 High energy layered Li-excess nickel-manganese oxide electrodes without voltage decay	43
2.2.1 Research backgorund	43
2.2.2 Experimental details	46
2.2.3 Results and discussion	49
2.2.4 Conclusion	100
2.2.5 References	101
Chapter 3 Biologically inspired organic compounds	105
3.1 Energy storage in biologically inspired organic electrode materials	105
3.1.1 Research background	105
3.1.2 Computational details	110

3.1.3 Results and discussion	111
3.1.4 Conclusion	124
3.2.5 References.....	126
3.2 Pteridine redox cofactors for rechargeable batteries.....	130
3.2.1 Research background	130
3.2.2 Experimental and computational details.....	131
3.2.3 Results and discussion	133
3.2.4 Conclusion	182
3.2.5 References.....	184
Chapter 4 Conclusion.....	188
Chapter 5 Abstract in Korean.....	192
Chapter 6 Acknowledgements.....	195
Curriculum Vitae	196

List of Tables

Table 2.1	The detailed data for the structural refinement of LLNMO using XRD patterns	56
Table 2.2	The detailed data for the structural refinement of LLNMO using ND patterns.....	57
Table 2.3	The atomic positions and occupancies in LL226 using ND patterns.....	58
Table 2.4	The atomic positions and occupancies in LL235 using ND patterns.....	59
Table 2.5	The atomic positions and occupancies in LL244 using ND patterns.....	60
Table 2.6	Proposed mechanism of structural evolution and capacity activation in LL226, LL235, and LL244	99
Table 3.1	The major bond lengths measured from the DFT calculations.	117
Table 3.2	The major bond length change in lumiflavine measured from the structures shown in Figure 3.8.....	122

List of Figures

Figure 2.1	XRD pattern of the synthesized layered Li-excess nickel-manganese oxide $\text{Li}_{1.2}\text{Ni}_{0.2}\text{Mn}_{0.6}\text{O}_2$	12
Figure 2.2	Charge/discharge profile (top) and the DEMS ion intensities for $m/z = 32, 28$, and 44 of the layered Li-excess transition metal oxide cathode material upon electrochemical cycling.....	13
Figure 2.3	FTIR spectra of the layered Li-excess transition metal oxide electrode at the end of charging (red, 4.8 V) and discharging (blue, 2.0 V) for the first few electrochemical cycles...	15
Figure 2.4	FTIR spectra of the cycled electrodes without oxygen evolution at the first charge, such as LiCoO_2 and $\text{LiNi}_{0.5}\text{Mn}_{0.5}\text{O}_2$	17
Figure 2.5	FTIR spectra of $\text{Li}_{1.2}\text{Ni}_{0.2}\text{Mn}_{0.6}\text{O}_2$ electrodes at as-prepared state (red), fully discharged state (2.0 V) after charged to 4.4 V (blue), and fully discharged state after charged to 4.8 V (black)	18
Figure 2.6	XPS (a) C 1s (b) O 1s and (c) Li 1s spectra of the surface of the pristine electrode (dotted line), surface (red line) and core (yellow line) of the electrode after 1st discharge, and surface (blue line) and core (green line) of the electrode after 2nd charge.....	20
Figure 2.7	HRTEM image of fully discharged LLNMO after five repeated cycles (2.0 – 4.8 V).	21
Figure 2.8	XPS O 1s depth profile of fully discharged LLNMO after five repeated cycles (2.0 – 4.8 V).....	24
Figure 2.9	Atomic concentration obtained by quantitative analysis of XPS depth profiling of the electrode after cell operation	

	(Etch rate: 10 nm s ⁻¹).....	26
Figure 2.10	Raw data of Mn 2p and Ni 2p XPS depth profiling spectra of the electrode after 5 cycles.....	27
Figure 2.11	Mn-to-Ni ratio obtained by quantitative analysis of XPS depth profiling of the electrode after cell operation (Etch rate: 10 nm s ⁻¹).....	28
Figure 2.12	Line EDS analysis of the cycled electrode milled by FIB using a gallium ion beam.....	29
Figure 2.13	XPS (a) Li 1s, (b) F 1s, and (c) P 2p spectra of as-prepared Li-excess transition metal oxide electrode (red) and the fully-discharged electrode after five electrochemical cycles (blue).....	31
Figure 2.14	Scheme of the proposed mechanism of the successive reactions inside the closed system originated from the oxygen evolution out of the layered Li-excess metal oxides...	37
Figure 2.15	a) Crystal structure of LiMO ₂ (M= Ni, Mn) with $R\bar{3}m$ symmetry and b) Li ₂ MnO ₃ with C2/m symmetry.....	50
Figure 2.16	XRD patterns of pristine LL226 (black), LL235 (red), and LL244 (blue).....	52
Figure 2.17	ND patterns of pristine LL226 (black), LL235 (red), and LL244 (blue).....	53
Figure 2.18	Simulated neutron diffraction patterns of LL226 (black), LL235 (red), and LL244 (blue).....	54
Figure 2.19	Lattice parameters of LL226, LL235, and LL244 observed by XRD and ND analyses.....	61
Figure 2.20	Rietveld refinements of the a, b, c) XRD patterns and d, e, f) ND patterns of LL226, LL235, and LL244 (left to	

right).....	62
Figure 2.21 XANES a) Ni K-edge spectra, and b) XANES Mn K-edge spectra of pristine LL226 (black), LL235 (red), and LL244 (blue).....	63
Figure 2.22 a) Charge/discharge profiles and b) differential capacity curves of LL226 (black), LL235 (red), and LL244 (blue) of the first cycle.....	65
Figure 2.23 a) Charge/discharge profiles and b) differential capacity curves of LL226 (black), LL235 (red), and LL244 (blue) of the fifth cycle.....	67
Figure 2.24 a) Capacity contributions on discharge above 3.4 V (black) and below 3.4 V (grey), and b) average potential (energy/capacity) of charge and discharge processes of the LLNMOs.....	68
Figure 2.25 XRD patterns of LL226 (black), LL235 (red), and LL244 (blue) after five electrochemical cycles.....	70
Figure 2.26 a) Peak ratio of (104)/(101) (black) and (104)/(003) (red) of LLNMOs before and after cycling, b) simulated XRD patterns of LLNMO with no transition metal ions in lithium layers (black), with 6 % nickel (blue) migration or manganese migration (red) into Li layers.....	71
Figure 2.27 Lattice parameters of LLNMOs before (black) and after (red) cycling obtained by Rietveld refinements.....	73
Figure 2.28 Raman spectra of LLNMOs before (bottom) and after five cycles (top).....	74
Figure 2.29 Raman spectra of LLNMOs before (black) and after five cycles (red) compared with spinel $\text{Li}_{1+x}\text{Mn}_2\text{O}_4$ (blue).....	86
Figure 2.30 a) HR-TEM images and b) corresponding SAED patterns	

(bottom) of as-prepared LL226 along $[100]_R$ direction which is parallel to $[0-10]_M$ direction of monoclinic $C2/m$	76
Figure 2.31 HR-TEM images and corresponding SAED patterns of a, b) LL226 along $[-441]_R$ direction which is parallel to $[10-1]_M$ direction of $C2/m$, and c, d) as-prepared LL244 along $[-441]_R$ direction.....	79
Figure 2.32 a) SAED pattern of LL226 after five cycles along $[-441]_R$ direction which is parallel to $[10-1]_M$ of monoclinic $C2/m$ and $[001]_C$ of cubic $Fd\text{-}3m$ (spinel phase). b-d) HR-TEM images and corresponding FFT patterns (inset) of local regions of the particle.....	80
Figure 2.33 Structural differences between the layered $(110)_R//(020)_M$ planes and spinel $(220)_C$ plane.....	82
Figure 2.34 a) SAED pattern and b) HR-TEM image and corresponding FFT patterns (inset) of LL244 after five cycles along $[-441]_R$ direction.....	83
Figure 2.35 Mn K-edge XANES spectra of LL226 (black), LL235 (red), and LL244 (blue) at a) charged state (4.8 V) and b) discharged state (2.0 V).....	85
Figure 2.36 Mn K-edge XANES spectra of a) LL226, b) LL235, and c) LL244 electrodes at pristine (black), charged to 4.8 V (red), and discharged to 2.0 V (blue).....	86
Figure 2.37 XPS Mn 2p spectra of a) LL226, b) LL244. Black, red, blue spectra (from top to bottom) represent the observed spectra of pristine LLNMO, surface of cycled LLNMO, and etched plane (surface + bulk properties) of LLNMO electrodes, respectively.....	88
Figure 2.38 Ni K-edge XANES spectra of LL226, LL235, LL244 at a)	

charged state and b) discharged state.....	89
Figure 2.39 Ni K-edge XANES spectra of a) LL226, b) LL235, and c) LL244 electrodes at pristine (black), charged to 4.8 V (red), and discharged to 2.0 V (blue).....	90
Figure 2.40 XPS Ni 2p spectra of a) LL226, b) LL244. Black, red, blue spectra represent the observed spectra of pristine LLNMO, surface of cycled LLNMO, and etched plane (surface + bulk properties) of LLNMO electrodes, respectively.....	91
Figure 2.41 The ratio of manganese to nickel quantified with XPS spectra.....	93
Figure 2.42 A model composite structure with nanometer-sized layered and spinel phases (top) and the oxidation states of the nickel and manganese composing the structure (bottom).....	95
Figure 2.43 Proposed capacity activation and structural evolution mechanism of LLNMOs with high-manganese-content (left) and high-nickel-content (right).....	96
Figure 3.1 Biochemical energy transduction in mitochondria (left panel) where flavins work as a redox center to store energy from nutrients into high-energy ATP. For synthetic energy device applications (right panel), flavins serve as an active material that reversibly takes up and releases electrons and lithium ions during electrochemical energy storage... ..	108
Figure 3.2 Different redox states of flavin-derivative molecules with indications of redox-active moieties upon electron uptake.....	109
Figure 3.3 DFT energies calculated for various $\text{Fl}_{\text{rad}}\text{Li}$ forms of riboflavin.....	112
Figure 3.4 DFT energies calculated for various $\text{Fl}_{\text{red}}\text{Li}_2$ forms of riboflavin.....	113

Figure 3.5	Calculated Mulliken charge changes of atoms in a riboflavin molecule during lithium coupled reduction process.....	116
Figure 3.6	Differential capacity (dQ/dV) curves of Li/lumiflavine cell calculated from the data shown in ref.19 showing two distinctive redox peaks confirming that the redox behavior of lumiflavine follows that of riboflavin.....	119
Figure 3.7	DFT energies calculated for various a) $\text{Fl}_{\text{rad}}\text{Li}$ and b) $\text{Fl}_{\text{red}}\text{Li}_2$ forms of lumiflavine. $\text{Fl}_{\text{rad}}\text{Li}$ with N5-Li1 bond and $\text{Fl}_{\text{red}}\text{Li}_2$ with N5-Li1/N1-Li2 bonds were energetically most stable for lumiflavine, in accordance with the results for riboflavin.....	120
Figure 3.8	DFT calculation results on lumiflavine 3D structure and bonding nature during battery operation.....	121
Figure 3.9	Mulliken charge changes in a lumiflavine molecule during Li-coupled reduction process.....	123
Figure 3.10	Molecular structures of pteridine derivatives as bioinspired redox compounds for energy storage.....	134
Figure 3.11	Redox mechanism of flavins inspired by biological energy transduction.....	135
Figure 3.12	Reversible tautomerism of LC, which is a structural isomerism from alloxazine to isoalloxazine.....	137
Figure 3.13	Cyclic voltammograms (CV) of pteridine derivatives measured in DMF solutions containing TBAP (black) and LiClO_4 (red) as electrolytes.....	138
Figure 3.14	Capacity-voltage profiles and the corresponding differential capacity plots (inset) of LC/Li cells.....	140
Figure 3.15	Capacity-voltage profile of a LC electrode obtained at high	

temperature (60° C).....	141
Figure 3.16 GITT profiles of the LC/Li cells under an intermittent discharge/charge for 1 hour at a low current rate of 10.0 mA g ⁻¹ with relaxation periods maintained for 5 hours.....	143
Figure 3.17 <i>ex situ</i> XRD analysis for LC electrodes at as-prepared (black), fully discharged (red), and fully recharged (blue) states.....	146
Figure 3.18 <i>Ex situ</i> XPS analysis of LC electrodes at different states of charge during battery cycling.....	147
Figure 3.19 <i>Ex situ</i> FTIR spectra of LC electrodes during electrochemical cycling which is reversibly switching upon reduction and oxidation of the LC.....	148
Figure 3.20 <i>Ex situ</i> emission spectra are reversibly switching upon reduction and oxidation of the LC which is indicative of the redox stability of alloxazinic systems and the tautomerism of LC during battery cycling.....	151
Figure 3.21 DFT calculation on LC during redox reactions. HOMO plots of LC and doubly reduced LC tautomers.....	152
Figure 3.22 HOMO plots of tetravalent anion lumichrome (LC)....	153
Figure 3.23 DFT energy comparison for various forms of [LC]Li (upper) and [LC]Li ₂ (lower) upon two lithium coupled-two electron reduction.....	154
Figure 3.24 DFT calculation for comparing two tautomer forms of [LC]Li in solvents. In polar solvent, isoalloxazinic form of [LC]Li is more stable than alloxazinic form, and <i>vice versa</i> in non-polar solvent.....	157
Figure 3.25 Changes in Mulliken charge of atoms (a, b) and bond lengths (c) in lumichrome molecules during discharge in	

	non-polar (ϵ : 3.04) and polar solvents (ϵ : 78.4) during Li-coupled reduction processes.....	158
Figure 3.26	HOMO plots for the doubly reduced species of ALX and LMZ. Black arrows indicate the proton which is bound to N1 or N10.....	159
Figure 3.27	DFT energies for lithiated alloxazine molecules with various configurations.....	160
Figure 3.28	DFT energies for lithiated lumazine molecules with various configurations.....	161
Figure 3.29	HOMO plots of tetravalent anion pteridine derivatives, ALX and LMZ.	162
Figure 3.30	Capacity-voltage profiles of ALX electrode at room temperature (black) and 60°C (red).....	163
Figure 3.31	Capacity-voltage profiles of LMZ electrode at room temperature (black) and 60°C (red).....	164
Figure 3.32	Differential capacity (dQ/dV) curves for alloxazine and lumazine electrodes.....	165
Figure 3.33	GITT profiles of the ALX/Li cells (top) and LMZ/Li cells (bottom).....	166
Figure 3.34	Photographs and SEM images for modified pteridine electrodes.....	170
Figure 3.35	X-ray diffraction patterns of pristine LC powder, LC electrode made of PTFE and super P, SWNT film, and LC-SWNT hybrid electrode.....	171
Figure 3.36	Differential capacity (dQ/dV) curves for LC and ALX hybrid electrodes.....	172
Figure 3.37	Capacity-voltage profiles of LC-CNT hybrid electrodes (LC hybrid) at various current rates and a pristine LC electrode at a 1C rate.....	173

Figure 3.38	Capacity-voltage profiles of ALX-CNT hybrid electrodes (ALX hybrid) at various current rates and a pristine ALX electrode at a 1C rate.....	174
Figure 3.39	Capacity-voltage profile of the CNTs electrode without active materials at 250 mA g ⁻¹	175
Figure 3.40	Capacity retention of the LC hybrid and ALX hybrid at 1.0 A g ⁻¹ and 2.0 A g ⁻¹ for 200 cycles.....	177
Figure 3.41	Capacity retentions of pristine electrodes of LC, ALX, and LMZ.....	178
Figure 3.42	Capacity retention of the LC hybrid and ALX hybrid at 5.0 A g ⁻¹ and 10.0 A g ⁻¹ for 500 cycles.....	179
Figure 3.43	Capacity-voltage profiles of pristine pteridine derivatives at 20 mA g ⁻¹ in sodium rechargeable batteries.....	180
Figure 3.44	Capacity-voltage profiles pteridine hybrid electrodes at 50 mA g ⁻¹ in sodium rechargeable batteries.....	181

Chapter 1. Introduction

1.1 Motivation and outlines

Breakthrough enhancement of the energy density of current lithium-ion batteries is one of the grand challenges in green energy technologies such as electric automobiles and large-scale power backups.¹⁻³ To address this issue, it is required to develop better electrode materials which are capable of storing and reversibly releasing more energy into/out of lighter mass. Most of currently commercialized electrode materials deliver less than one lithium ion per transition metal ion, which limits the theoretical capacity.³⁻⁵ Therefore, it is necessary to explore of new electrode materials that offer a higher reversible energy densities based on new energy storage mechanisms.

Among the various cathode materials that have been studied to date, the layered Li-excess transition metal oxides ($\text{Li}[\text{Li}_x\text{Ni}_y\text{Mn}_{(1-x-y)}]\text{O}_2$, $0 < x < 0.33$, $0 < y < 0.5$ hereafter called LLNMO), are of particular interest due to their extraordinarily high reversible capacities ($> 230 \text{ mAh g}^{-1}$) and relatively high operating voltage ($\sim 3.6 \text{ V vs. Li/Li}^+$ on average).⁶ In typical Ni–Mn-based layered materials, the $\text{Ni}^{n+}/\text{Ni}^{4+}$ ($2 \leq n \leq 3$) redox reaction is electrochemically active, *i.e.*, it contributes to the reversible capacity, while electrochemically inactive Mn^{4+} ions stabilize the lattice framework.⁶⁻⁸ Therefore, several research groups have described LLNMO as structurally integrated composites of inactive Li_2MnO_3 and active LiMO_2 , *i.e.*, $z\text{Li}_2\text{MnO}_3-(1-z)\text{LiMO}_2$ ($\text{M} = \text{Ni}$,

Mn, $0 < z < 1$).^{9,10} However, the observed capacity from LLNMO far exceeds the theoretical values based on the redox couples of LiMO₂ components in the materials when the materials are charged beyond a voltage plateau of 4.5-4.6 V accompanied with oxygen gas evolution.^{6,9,10} Furthermore, recent studies have shown that the cathode potential of LLNMO continuously decreases as electrochemical cycle proceeds.^{10,11} To understand and utilize the high reversible capacity of LLNMO, in-depth study is necessary to reveal the underlying energy storage mechanism. In this thesis, the role and effects of oxygen evolved from LLNMO during electrochemical cycling were unveiled and the strategy to protect the surface of electrode materials from the acidic byproducts was briefly proposed. Moreover, it is proposed that the compositional optimization of LLNMO offers highly efficient energy storage capability without voltage decay. The detailed results are discussed in Chapter 2.

Another promising alternative to conventional inorganic electrodes made from limited mineral resources through non-ecological, high-temperature processes, renewable and naturally abundant are organic redox chemicals which have been studied in recent years.¹²⁻¹⁴ As such, intensive efforts have been put toward the development of sustainable batteries. One of the effective ways of exploring the organic electrodes is mimicking biologically occurring redox reactions from nature. In this thesis, the natural redox reaction in biological metabolism has inspired the design of high performance energy storage materials. Flavins and pteridine derivatives which are key redox

elements in cellular energy transduction were exploited as new-type energy storage materials in lithium ion batteries.^{15,16} Moreover, a novel strategy is proposed for tailoring these biological redox units to achieve one of the best electrochemical performances available at this time. The detailed results dealt in Chapter 3 apply unexplored biological redox compounds in synthetic energy storage systems, and advance our understanding of their energy storage mechanisms.

In summary, this thesis deals with two types of alternative electrode materials whose energy storage mechanisms have not been clearly understood: layered Li-excess nickel-manganese oxides and biologically inspired organic compounds. These classes of materials have high potential of utilization in future energy storage devices due to their high capacity while the practical utilization of these materials requires in-depth understanding on the energy storage reactions of the materials. In this respect, the energy storage mechanism of the layered Li-excess nickel-manganese oxides and organic compounds are proposed in detail by using the combination of experiments and DFT calculations. Moreover, the strategies to improve their electrochemical performances are demonstrated. I hope this thesis to be a foundation for development of lithium rechargeable batteries using layered Li-excess transition metal oxides or biologically derived organic compounds as alternative cathode materials.

1.2 References

- 1 Sathiya, M. *et al.* Reversible anionic redox chemistry in high-capacity layered-oxide electrodes. *Nat Mater* **12**, 827-835, doi:10.1038/Nmat3699 (2013).
- 2 Tarascon, J. M. & Armand, M. Issues and challenges facing rechargeable lithium batteries. *Nature* **414**, 359-367, doi:10.1038/35104644 (2001).
- 3 Kang, K. S., Meng, Y. S., Breger, J., Grey, C. P. & Ceder, G. Electrodes with high power and high capacity for rechargeable lithium batteries. *Science* **311**, 977-980, doi:10.1126/science.1122152 (2006).
- 4 Park, Y. U. *et al.* Synthesis of Multicomponent Olivine by a Novel Mixed Transition Metal Oxalate Coprecipitation Method and Electrochemical Characterization. *Chemistry of Materials* **22**, 2573-2581, doi:10.1021/Cm903616d (2010).
- 5 Armand, M. & Tarascon, J. M. Building better batteries. *Nature* **451**, 652-657, doi:10.1038/451652a (2008).
- 6 Lu, Z., MacNeil, D. D. & Dahn, J. R. Layered Cathode Materials $\text{Li}[\text{Ni}_x\text{Li}_{(1/3-2x/3)}\text{Mn}_{(2/3-x/3)}]\text{O}_2$ for Lithium-Ion Batteries. *Electrochemical and Solid-State Letters* **4**, A191-A194, doi:10.1149/1.1407994 (2001).
- 7 Yoon, W.-S., Grey, C. P., Balasubramanian, M., Yang, X.-Q. & McBreen, J. In Situ X-ray Absorption Spectroscopic Study on LiNi0.5Mn0.5O_2 Cathode Material during Electrochemical Cycling. *Chemistry of Materials* **15**, 3161-3169, doi:10.1021/cm030220m (2003).
- 8 Bréger, J. *et al.* Effect of High Voltage on the Structure and Electrochemistry of $\text{LiNi}_{0.5}\text{Mn}_{0.5}\text{O}_2$: A Joint Experimental and

- Theoretical Study. *Chemistry of Materials* **18**, 4768-4781, doi:10.1021/cm060886r (2006).
- 9 Thackeray, M. M. *et al.* Li₂MnO₃-stabilized LiMO₂ (M = Mn, Ni, Co) electrodes for lithium-ion batteries. *Journal of Materials Chemistry* **17**, 3112-3125, doi:10.1039/B702425h (2007).
- 10 Yabuuchi, N., Yoshii, K., Myung, S.-T., Nakai, I. & Komaba, S. Detailed Studies of a High-Capacity Electrode Material for Rechargeable Batteries, Li₂MnO₃–LiCo_{1/3}Ni_{1/3}Mn_{1/3}O₂. *Journal of the American Chemical Society* **133**, 4404-4419, doi:10.1021/ja108588y (2011).
- 11 Hong, J. *et al.* Structural evolution of layered Li_{1.2}Ni_{0.2}Mn_{0.6}O₂ upon electrochemical cycling in a Li rechargeable battery. *Journal of Materials Chemistry* **20**, 10179-10186, doi:10.1039/C0jm01971b (2010).
- 12 Yang, P. D. & Tarascon, J. M. Towards systems materials engineering. *Nat Mater* **11**, 560-563, doi:10.1038/Nmat3367 (2012).
- 13 Tarascon, J. M. Towards Sustainable and Renewable Systems for Electrochemical Energy Storage. *Chemsuschem* **1**, 777-779, doi:10.1002/cssc.200800143 (2008).
- 14 Chen, H. *et al.* From biomass to a renewable Li_xC₆O₆ organic electrode for sustainable Li-ion batteries. *Chemsuschem* **1**, 348-355, doi:10.1002/cssc.200700161 (2008).
- 15 Lee, M. *et al.* Redox Cofactor from Biological Energy Transduction as Molecularly Tunable Energy-Storage Compound. *Angew Chem Int Edit* **52**, 8322-8328, doi:10.1002/anie.201301850 (2013).
- 16 Lee, M. *et al.* Organic Nanohybrids for Fast and Sustainable Energy Storage. *Adv Mater* **26**, 2558-2565, doi:10.1002/adma.201305005 (2014).

Chapter 2. Layered Li-excess nickel-manganese oxides

2.1 Role of oxygen evolution from layered Li-excess nickel-manganese oxides

(The essence of this chapter has been published in Chemistry of Materials.

Reprinted from [J. Hong *et al.* *Chem. Mater.*, 24, 2692 (2012)

DOI:10.1021/cm3005634]. Because this paper has been distributed under a Creative Commons license (Attribution-Noncommercial 2.5), one may reuse the contents for the paper for non-commercial/educational purposes without obtaining additional permission from American Chemical Society, providing that the author and the original source of publication are fully acknowledged.)

2.1.1. Research background

Increasing demand for green energy technologies for automobiles and large-scale power backups has moved Li rechargeable batteries to the center of attention. These batteries exhibit outstanding energy storage performance.^{1,2} However, commercialization of these technologies requires even more advanced Li rechargeable batteries.^{1,3} Specifically, better electrode materials capable of delivering more energy at faster rates are required. Though layered cobalt-based oxides, spinel manganese-based oxides, and olivine iron-based phosphates have been intensively investigated as promising

candidates,⁴⁻⁹ their low energy densities inhibit their application as the power source for new technologies. Therefore, development of new electrode materials that offer a higher reversible energy density is needed.

Among the cathode materials reported so far, the layered Li-excess nickel-manganese oxides ($\text{Li}[\text{Li}_{(1/3-2x/3)}\text{Ni}_x\text{Mn}_{(2/3-x/3)}]\text{O}_2$, $0 < x < 0.5$, LLNMO) first introduced by Lu *et al.*¹⁰ have promising electrochemical properties with exceptionally high capacities ($> 250 \text{ mAh g}^{-1}$).^{11,12} The unusually high capacity is available after the first charging process over 4.6 V that includes a voltage plateau near 4.5 V.¹² The long voltage plateau at charging, a unique feature of Li-excess oxide cathodes, corresponds to the delithiation process that accompanies oxidation of O^{2-} within the crystal structure and subsequent evolution of oxygen gas.^{13,14} Intensive investigations to interpret the abnormally high capacity have revealed that a structural rearrangement after oxygen extraction and corresponding activation of a manganese redox reaction contribute significantly to the high capacity.^{11,15-20} Surprisingly, there has been little interest in the role and effects of the evolved oxygen on the electrochemical system. Oxygen is known to participate in a critical safety reaction of the cell *via* thermal runaway at elevated temperatures.²¹⁻²³ Furthermore, recent studies on Li-air batteries revealed that oxygen can react with the conventional carbonate-based electrolyte during cycling.²⁴⁻²⁶ Thus, identifying the pathway of evolved oxygen in Li-excess materials is important and should not be overlooked.

In this chapter, I discuss the critical role of oxygen evolved from the

lattice of LLNMO in Li rechargeable batteries. Gaseous byproducts evolved during the electrochemical cycling and the deposits on the electrode surface were analyzed to track the reaction path of oxygen within the system. The extracted oxygen vigorously participated in a series of reversible/irreversible reactions inside the cell and eventually deteriorated the electrochemical performance of the cell, especially in terms of its cycle stability and rate capability.

2.1.2. Experimental details

Raw Materials

Li_2CO_3 (99%) and NaHCO_3 (99%) were purchased from Junsei (Japan) and $\text{MnSO}_4 \cdot \text{H}_2\text{O}$ (99%), $\text{NiSO}_4 \cdot 6\text{H}_2\text{O}$ (99%), LiCoO_2 (99.9%), and LiMn_2O_4 (99.9%) were purchased from Sigma–Aldrich (USA). They were used as precursors without additional treatment.

Preparation of the Materials

The LLNMO with a composition of $\text{Li}_{1.2}\text{Ni}_{0.2}\text{Mn}_{0.6}\text{O}_2$ ($\text{Li}[\text{Li}_{0.2}\text{Ni}_{0.2}\text{Mn}_{0.6}]\text{O}_2$, or $0.5\text{LiNi}_{0.5}\text{Mn}_{0.5}\text{O}_2 \cdot 0.5\text{Li}_2\text{MnO}_3$) was synthesized via a coprecipitation method. Mixed NiSO_4 and MnSO_4 aqueous solution (0.2 M, Mn/Ni = 3 and 1, respectively) was added dropwise to an equal volume of a 1 M NaHCO_3 aqueous solution under constant stirring at 50 °C. The pH was maintained at 9 by adding ammonium hydroxide. The mixed solution containing the green precipitate was aged for 24 h. The mixed nickel–manganese carbonate precursor ($\text{Ni}_{0.25}\text{Mn}_{0.75}\text{CO}_3$) precipitate was filtered,

washed with deionized water several times, and dried overnight at 120 °C. The dried powder was ball-milled with a 3% excess of the stoichiometric amount of Li₂CO₃ to compensate for possible lithium loss during the calcination. The mixture was finally heated at 900 °C for 6 h in air and then quenched with liquid N₂.

Electrochemical Analysis and DEMS Analysis

Electrodes were fabricated by the following sequences. A slurry of 80 wt % active materials, 10 wt % carbon black (Super-P, TIMCAL), and 10 wt % polyvinylidene fluoride (PVDF) binder dissolved in *N*-methyl-1,2-pyrrolidone (NMP, Sigma-Aldrich, 99.5%) was cast onto Al foil. The NMP was evaporated at 120 °C over 2 h. Coin cells (Hohsen, CR2016, Japan) were assembled with the electrodes, the Li counter electrode, a separator (Celgard 2400), and a 1 M solution of LiPF₆ in a mixture of ethyl carbonate/dimethyl carbonate (EC/DMC, 1:1 v/v) in an argon-filled glovebox. The galvanostatic charging/discharging process was performed for five cycles at 25 °C at 10 mA g⁻¹ at a voltage range of 2.0–4.8 V by a potentio-galvanostat (WonA Tech, WBCS 3000, Korea). Differential electrochemical mass spectroscopy (DEMS) analysis was performed via a small pinhole in each cap of the coin-type cell.

Ex Situ Analyses on the Electrode Surface

The electrodes fully discharged to 2.0 V after five electrochemical cycles were retrieved by disassembling the coin cells and rinsed with DMC. All the procedures were performed in the glovebox. Fourier transform infrared

(FTIR) spectroscopy analysis was performed on a pellet made of active materials from the electrodes and KBr powder by using an FTIR spectrometer (JASCO, 6200 series, Japan). For high-resolution transmission electron microscopy (HRTEM) analysis, the active material was retrieved from the electrode, dispersed in ethanol, and transferred onto carbon-coated Cu grids. High-resolution images of the samples were recorded using a field emission TEM (FETEM, JEOL, JEM-3000F, Japan). Cycled electrodes were used without pretreatment for X-ray photoelectron spectroscopy (XPS, Thermo VG Scientific, Sigma Probe, U.K.) and field emission scanning electron microscopy (FESEM, Carl Zeiss, AURIGA, Germany) analyses. Special care was taken to prevent contamination of the electrode by air during all experiments.

Confirmation of Metal Dissolution

Inductively coupled plasma–atomic emission spectrometer (ICP-AES, Thermo Jarrel Ash, Polyscan 60E, USA) analysis was conducted on the separator and Li metal anode dissembled from coin-cell after five cycles.

2.1.3. Results and discussion

Characterization of the as-prepared layered LLNMO

Figure 2.1 shows the X-ray diffraction (XRD) pattern of the as-prepared layered Li-excess transition metal oxide compound. All the peaks correspond to O₃-type structures that can be indexed by $R\bar{3}m$ symmetry; no impurities are evident. The peaks at 21–25° can be indexed to $C2/m$ symmetry and

indicate the existence of a Li_2MnO_3 -like superstructure in the transition metal layer. The composition of the pristine sample obtained from ICP-AES was $\text{Li}_{1.145}\text{Ni}_{0.212}\text{Mn}_{0.643}\text{O}_2$.

Partially Reversible Formation/Decomposition of Lithium Carbonate by Oxygen Evolved from the Li–Excess Materials.

To trace the gas evolution during the electrochemical reactions, real-time analysis by DEMS was performed for the first few cycles under a low current density of 10 mA g^{-1} . DEMS results in Figure 2.2 showed that most of the oxygen gas evolution occurred at the end of the first charging process near 4.6 V, in agreement with previous reports.¹³ However, unexpectedly, a considerable amount of other gases such as CO and CO_2 were simultaneously detected with oxygen.

The formation of these carbon-containing gases during the initial charging process implies that additional reactions occurred along with oxygen evolution. In the second cycle, only a trace amount of oxygen was detected. This indicated that subsequent cycles do not involve oxygen extraction, in agreement with previous reports.^{11, 13} In contrast, significant amounts of CO and CO_2 were detected in subsequent charging steps. Also, the evolution of these gases occurred starting at around 4.0 V, substantially lower than the 4.6 V for the first charging process, indicating the oxidization of different chemical species. CO and CO_2 evolution was also observed at the first discharging process.

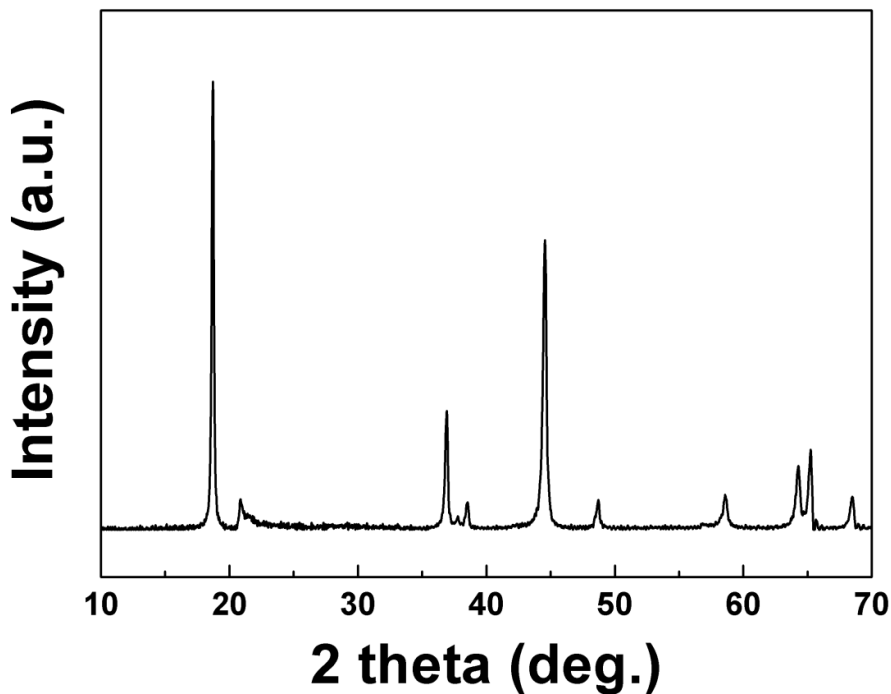


Figure 2.1. XRD pattern of the synthesized layered Li-excess nickel-manganese oxide $\text{Li}_{1.2}\text{Ni}_{0.2}\text{Mn}_{0.6}\text{O}_2$. All the peaks correspond to O3-type structures that can be indexed by $R\bar{3}m$ symmetry, and no impurities are evident.

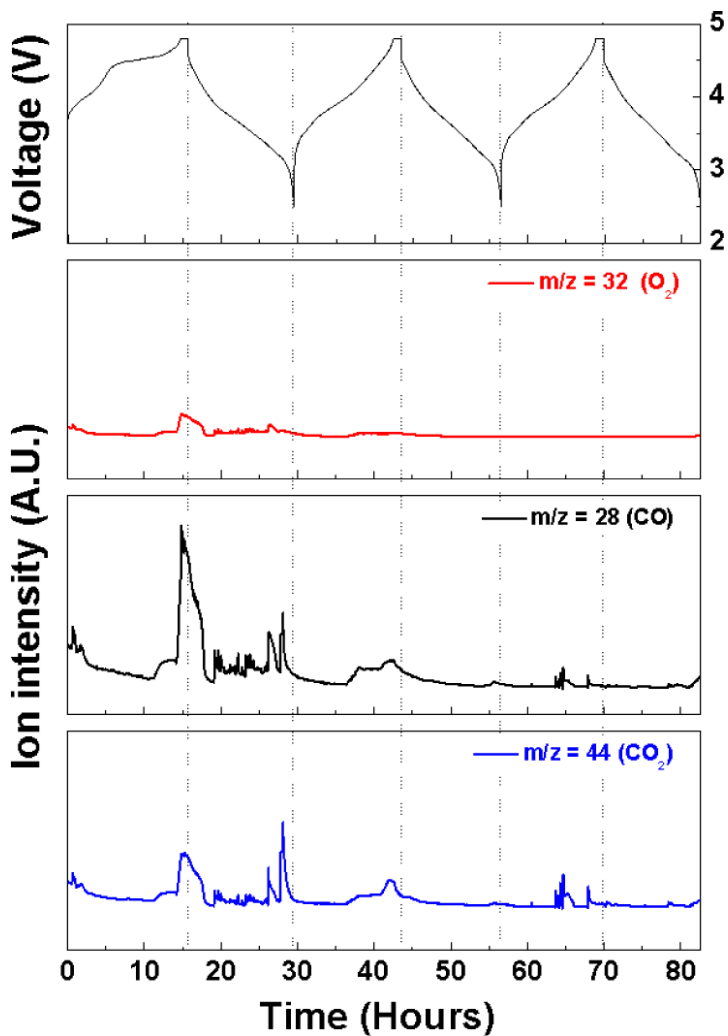
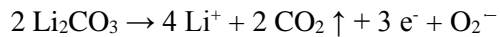


Figure 2.2. Charge/discharge profile (top) and the DEMS ion intensities for $m/z = 32$, 28 , and 44 of the layered Li-excess transition metal oxide cathode material upon electrochemical cycling. O_2 ($m/z = 32$), CO ($m/z = 28$), and CO_2 ($m/z = 44$) repeatedly evolve during the charging process.

To further clarify the reactions occurring in the cell, *ex situ* FTIR analysis was performed on the electrode at the end of charging and discharging events for the initial few cycles (Figure 2.3). The peaks at 1437 cm^{-1} , 1498 cm^{-1} , and 867 cm^{-1} exactly correspond to the IR-active modes of Li_2CO_3 .^{24, 27, 28} These peaks appeared and disappeared repeatedly with discharging and charging, respectively. This indicates that Li_2CO_3 formed during the discharging process and decomposed during the charging process, *i.e.*, reversibly. When Li_2CO_3 decomposes, CO and CO_2 can be formed following the path below and reactions (1) and (5).^{24, 25}



Detection of these gases by DEMS during subsequent charging steps (Figure 1) supports the decomposition of Li_2CO_3 as their source. In contrast, formation of Li_2CO_3 was not detected for conventional cathodes that did not evolve oxygen (LiCoO_2 and $\text{LiNi}_{0.5}\text{Mn}_{0.5}\text{O}_2$) under identical experimental conditions (Figure 2.4) and LLNMO cycled under non-oxygen releasing condition (Figure 2.5).

Figure 2.4 shows the FTIR spectra of two layered electrode materials after five charging/discharging cycles. These materials do not release oxygen gas during the electrochemical reactions.

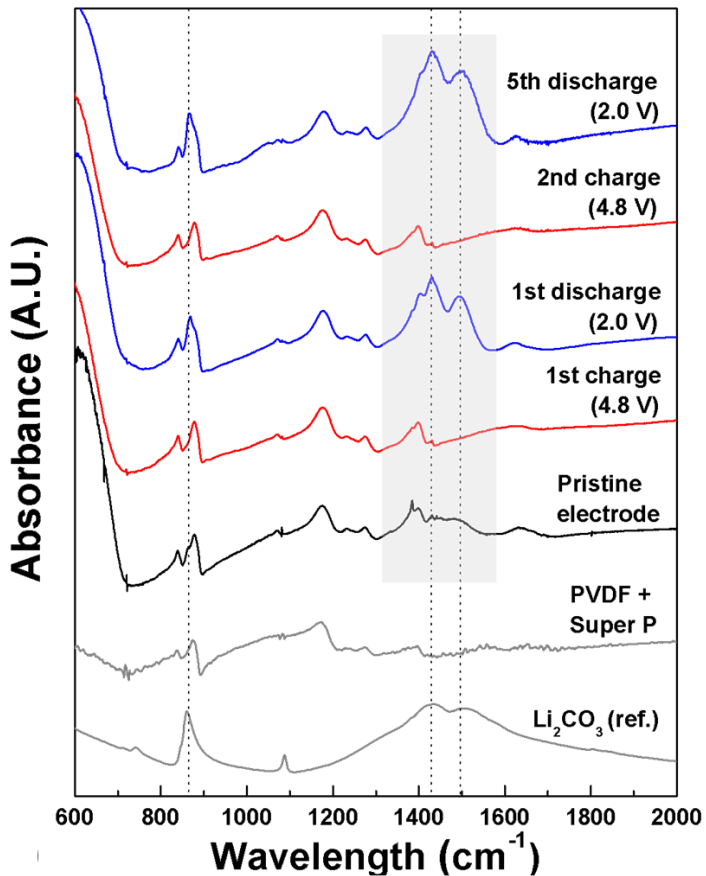


Figure 2.3. FTIR spectra of the layered Li-excess transition metal oxide electrode at the end of charging (red, 4.8 V) and discharging (blue, 2.0 V) for the first few electrochemical cycles. The spectrum for Li_2CO_3 powder is provided as a reference. Reversible formation and decomposition of Li_2CO_3 (peaks at 1437, 1498, and 867 cm^{-1} , dotted lines) were observed for the discharged and charged states, respectively, for coin-type cells.

Because Li_2CO_3 forms at a low voltage range (about 2.0–3.0 V in the case of Li-excess metal oxide), all the electrodes were fully discharged to 2.0 V vs. Li^+/Li . There was no evidence of Li_2CO_3 formation under the same cycling conditions as for LLNMO. Moreover, the FTIR spectrum of the $\text{Li}_{1.2}\text{Ni}_{0.2}\text{Mn}_{0.6}\text{O}_2$ electrode cycled under non-oxygen releasing condition showed only trace amount of Li_2CO_3 as shown in Figure 2.5. These results imply that the oxygen extracted from the crystalline material contributed to the formation of Li_2CO_3 .

This indicates that Li_2CO_3 formation is closely related to the oxygen extracted from the lattice of the LLNMO. A detailed mechanism for the formation of Li_2CO_3 is given in the later part in this paper. While the formation and decomposition of Li_2CO_3 seem to be partially reversible according to the FTIR analysis, the signal intensities for the evolved gas species decreased with the number of cycles (Figure 2.2). In the case of coin-type batteries or commercial Li rechargeable batteries, *i.e.*, closed systems, any evolved gas species are trapped within the cells. Consequently, additional reactions between CO, CO_2 , oxygen, and the electrolyte are expected and can be related to the reversible formation of Li_2CO_3 upon lithiation, as observed in FTIR. On the other hand, the reduction of the signal intensities may be due to escape of the gases from the open-cell system used for the DEMS analysis; this would reduce additional reactions between CO, CO_2 , oxygen, and the electrolyte.

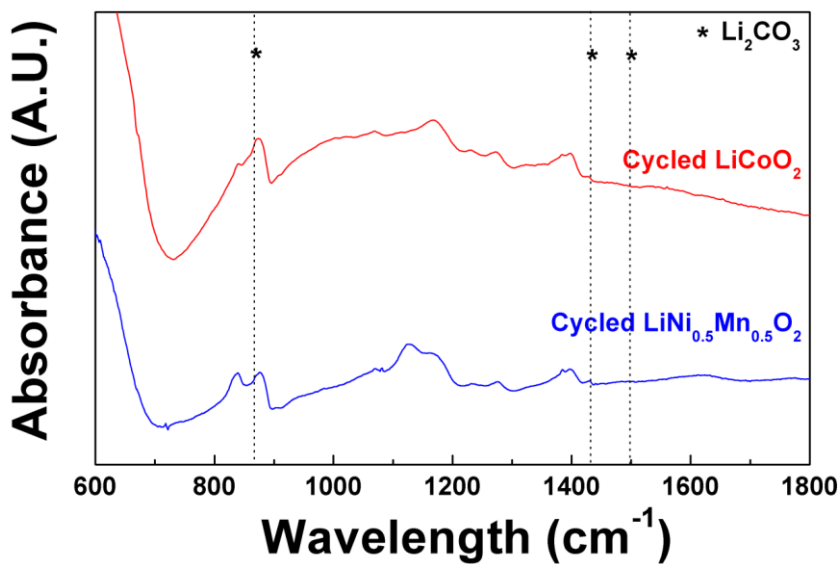


Figure 2.4. FTIR spectra of the cycled electrodes without oxygen evolution at the first charge, such as LiCoO_2 and $\text{LiNi}_{0.5}\text{Mn}_{0.5}\text{O}_2$. All electrodes are fully discharged to 2.0 V

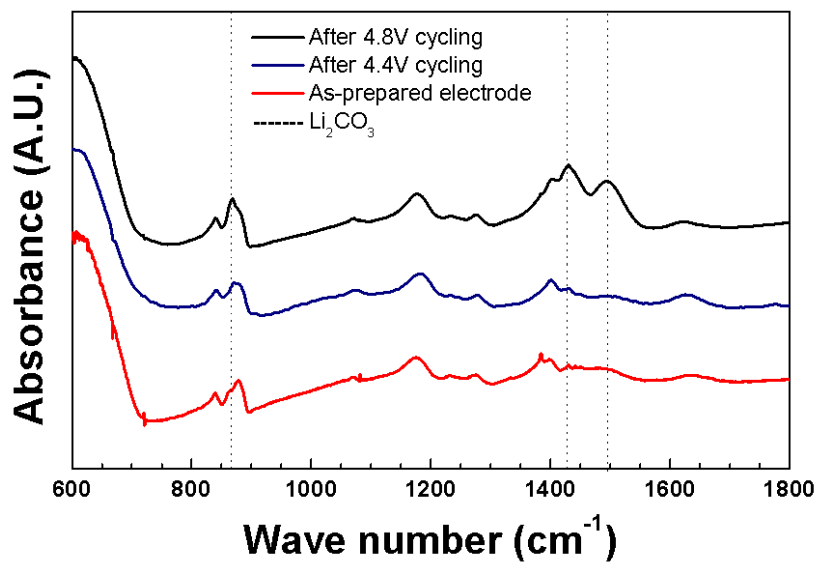


Figure 2.5. FTIR spectra of $\text{Li}_{1.2}\text{Ni}_{0.2}\text{Mn}_{0.6}\text{O}_2$ electrodes at as-prepared state (red), fully discharged state (2.0 V) after charged to 4.4 V (blue), and fully discharged state after charged to 4.8 V (black).

The compounds formed on the electrode surface were studied by XPS analysis before and after electrochemical cycling. Figure 2.6a-c show the XPS spectra obtained for the pristine electrode and the electrodes after the first cycle (fully discharged) and the second charge. From the C 1s and O 1s the electrode after 1st discharge, and surface (blue line) and core (green line) of the electrode after 2nd charge. Depth of etching: 30 nm. The signal for C-O bonding, CO_3^{2-} , and Li-F appeared at the electrode surface after discharge. spectra, the formation of compounds containing C-O (286.5 eV^{29,30}, Figure 2.6a) and CO_3^{2-} (531.8 eV³⁰, Figure 2.6b) was clearly observed at the surface of the discharged electrode after cycling. The Li 1s spectra also signify the formation of compounds such as Li_2CO_3 and LiF (55.5 eV and 56.3 eV³⁰, Figure 2.6c) during discharge. After an etching process, the signals from the products of the reaction between gases and electrolyte disappeared and the signals from the LLNMO (M-O bond, 530 eV¹⁶) arose. Accordingly, the thickness of formed compounds is less than 30 nm. At the charged state, the peaks from the bonds between carbon and oxygen significantly decreased in C 1s and O 1s spectra. Moreover, no peak was detected in Li 1s spectra. The disappearance of the peaks indicates that the decomposition of the products on the electrode surface occurred during charge. The observation of the repeated formation and decomposition of the compounds upon battery cycling is in accordance with the FTIR results. HRTEM revealed that a thin amorphous layer (5–10 nm) had formed on the surface of the electrode at discharged state (Figure 2.7) which is attributed to Li_2CO_3 and LiF.

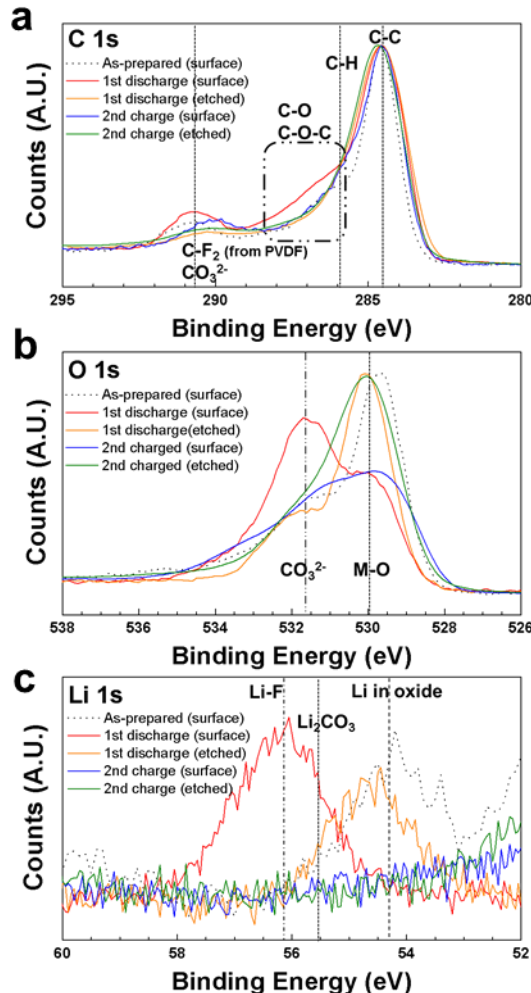


Figure 2.6. XPS (a) C 1s (b) O 1s and (c) Li 1s spectra of the surface of the pristine electrode (dotted line), surface (red line) and core (yellow line) of

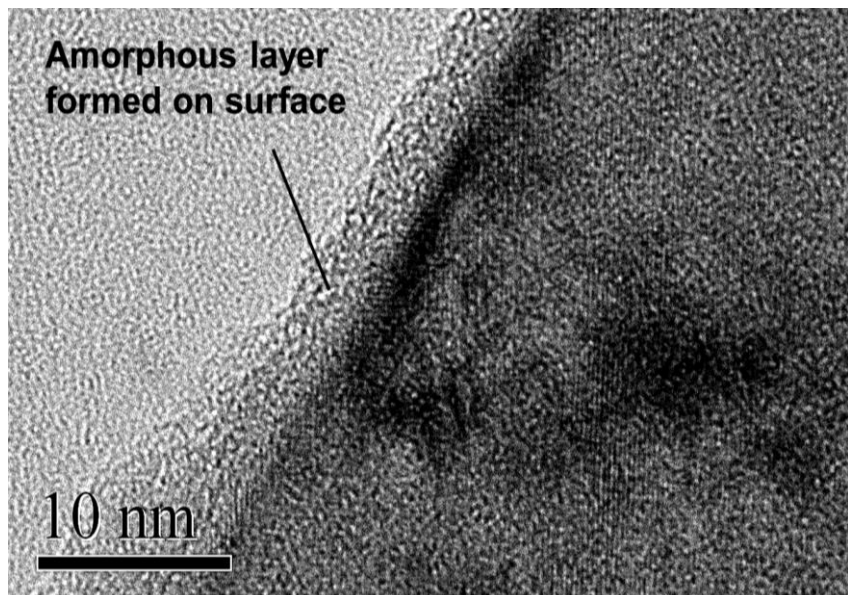
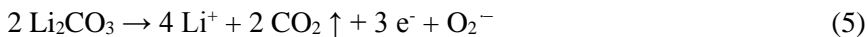
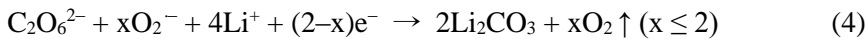


Figure 2.7. HRTEM image of fully discharged LLNMO after five repeated cycles (2.0 – 4.8 V). An amorphous layer 5-10 nm thick on the surface of the particle was observed.

Freunberger *et al.*²⁴ and Bruce *et al.*³¹ proposed that oxygen radicals are responsible for the decomposition of a carbonate-based electrolyte and lead to the formation of byproducts, including Li_2CO_3 and organic compounds. We suggest that when oxygen gas is present within the cell, oxygen radicals can be easily generated by receiving electrons from the conductive surface of the electrodes during the discharging process (reaction (1) below).^{24, 25, 27} Oxygen radicals in the cells would react rapidly with the electrolyte (*e.g.*, ethylene carbonate (EC)); the ring structure of the electrolyte solvent could be opened for a carbonate-based organic electrolyte (reaction (2)). As a result, CO_2 , water, and other carbon-containing byproducts would be formed during this reaction at the first discharging process. The oxygen radicals would also react with CO_2 to generate $\text{C}_2\text{O}_6^{2-}$ (peroxycarbonate) ions in the cell (reaction (3)) and finally form Li_2CO_3 (reaction (4)) on the surface of the electrodes. Moreover, the oxygen radicals could be extracted directly from the LLNMO framework during the first charging process. It seems to be easier for oxygen ions (O^{2-}) in oxide lattices to lose fewer electrons to become oxygen radicals (O_2^-) rather than lose more electrons to transform into the gas phase (O_2) during the charging process. This results in simultaneous CO and CO_2 generation during the first charging process, as observed in the DEMS experiment. At the next charging process, the formed Li_2CO_3 would decompose into CO and CO_2 (reactions (5), (2)). Interestingly, the observation of the partially-reversible formation of Li_2CO_3 in this system is in agreement with the results recently reported for Li-air batteries.^{24, 27}



Severe damage on the surface of the electrode including Mn dissolution after the electrochemical cycles

XPS O 1s depth profile (etch rate = 10 nm min⁻¹, Figure 2.8) pointed out that the intensity of the peak from the M-O bond (530 eV) on the electrode surface is abnormally low relative to that in the core of the electrode. This implies that the transition metal content noticeably decreases along the distance from the electrode core. Quantitative analysis of the XPS depth profiles manifested that the manganese concentration was significantly deficient near the surface, while the nickel concentration remained almost constant throughout the cycled electrode (Figure 2.9, Figure 2.10). Figure 2.10 shows the Mn 2p and Ni 2p XPS spectra obtained by depth profiling of the electrode after five electrochemical cycling. In contrast to the Ni 2p spectra, the area of Mn 2p spectra significantly increased when the core of the electrode was exposed. When we convert the raw data into the quantitative data as shown in Figure 2.11, we found that the manganese-to-nickel ratio suddenly changed at a few nanometers under the surface of the electrode after five repeated cycles in contrast to the pristine electrode.

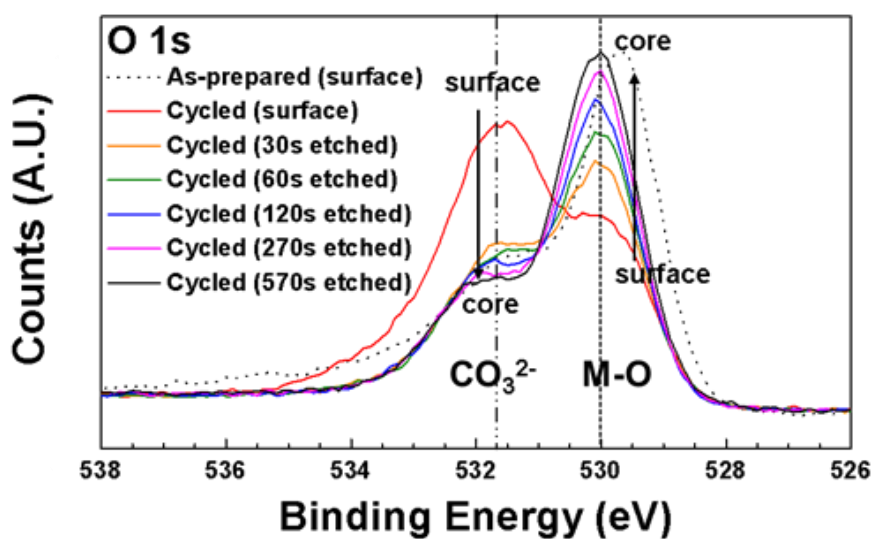


Figure 2.8. XPS O 1s depth profile of fully discharged LLNMO after five

The manganese concentration was significantly deficient near the surface, while the nickel concentration remained almost unchanged. The severe Mn deficiency for the cycled sample strongly implies the outbreak of manganese dissolution during cell operation at the interface between the electrode and the electrolyte, in consistent with the ICP-AES result. We further investigated the distribution of transition metal components in the cycled electrode by energy dispersive spectroscopy (EDS, Figure 2.12) analysis equipped in FESEM. The elemental analysis revealed that the manganese-to-nickel ratio prominently reduces at the surface. Comparison between the surface and the core exposed by using focused ion beam (FIB) indicated that a remarkable deficiency in the Mn amount was observed at the surface of the electrode. The dotted line in Figure 2.12 indicates the edge of the groove created by the FIB milling. A dramatic decrease was observed in the Mn amount at the edge between the surface and the bulk of the electrode. This finding is consistent with Mn dissolution during charging/discharging processes; it is in good agreement with XPS depth profiling (Figure 2.11).

The severe Mn deficiency for the cycled sample strongly implies the outbreak of manganese dissolution during cell operation at the interface between the electrode and the electrolyte. The result of ICP-AES analysis also confirmed the presence of Mn and Ni in separator and the counter electrode after battery operation. This is a clear evidence of the dissolution of metal ions from the Li-excess electrode materials.

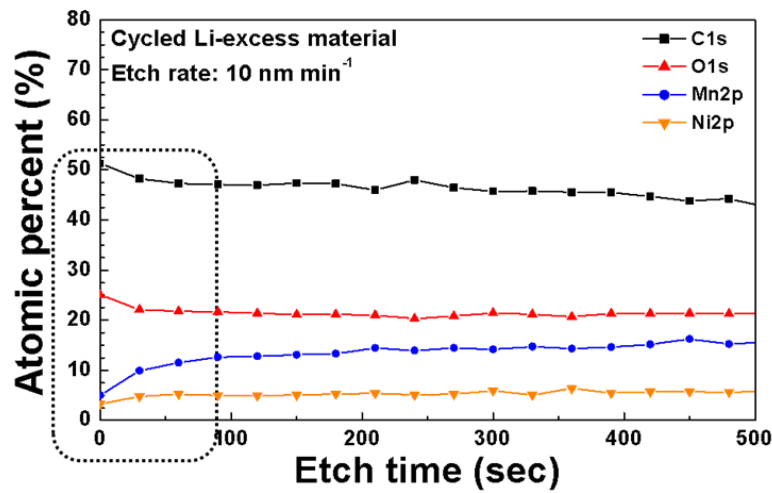


Figure 2.9. Atomic concentration obtained by quantitative analysis of XPS depth profiling of the electrode after cell operation (Etch rate: 10 nm s⁻¹). The Mn deficiency observed at the surface of the electrode implies that significant Mn²⁺ dissolution occurred during the cycling.

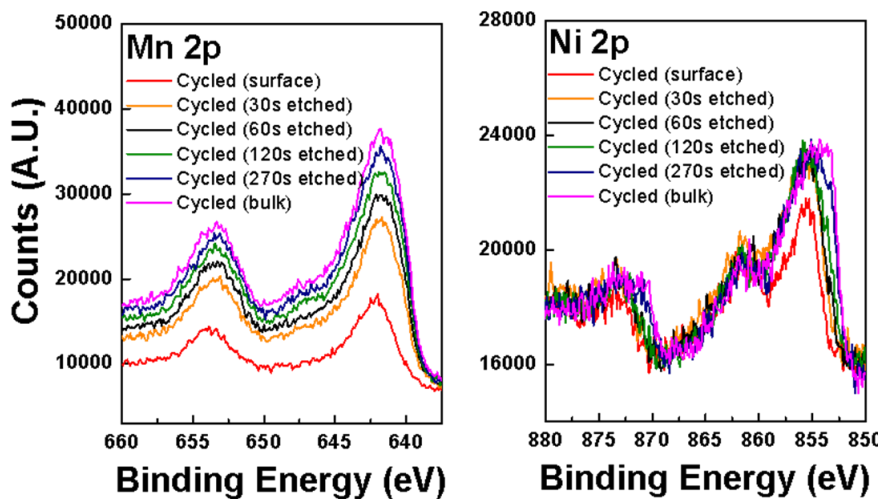


Figure 2.10. Raw data of Mn 2p and Ni 2p XPS depth profiling spectra of the electrode after 5 cycles. (Etch rate: 10 nm min^{-1}) Figure 2.9 was obtained by conversion of this data using a Thermo Avantage software.

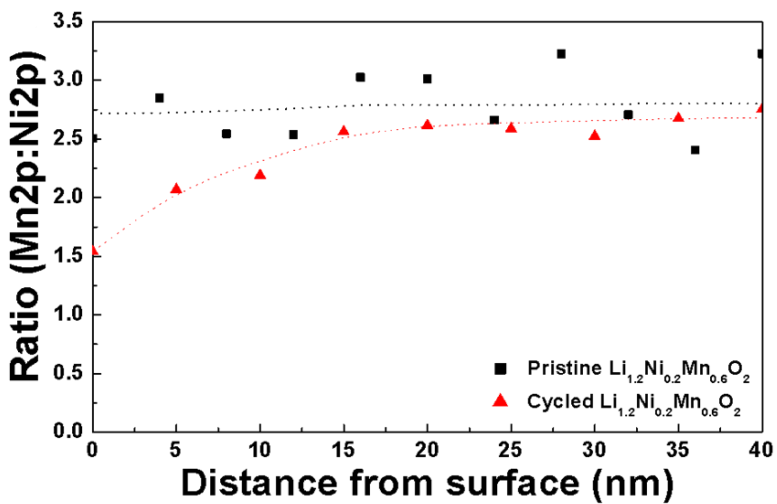


Figure 2.11. Mn-to-Ni ratio obtained by quantitative analysis of XPS depth profiling of the electrode after cell operation (Etch rate: 10 nm s^{-1}). The Mn deficiency observed at the surface of the electrode implies that significant Mn^{2+} dissolution occurred during the cycling.

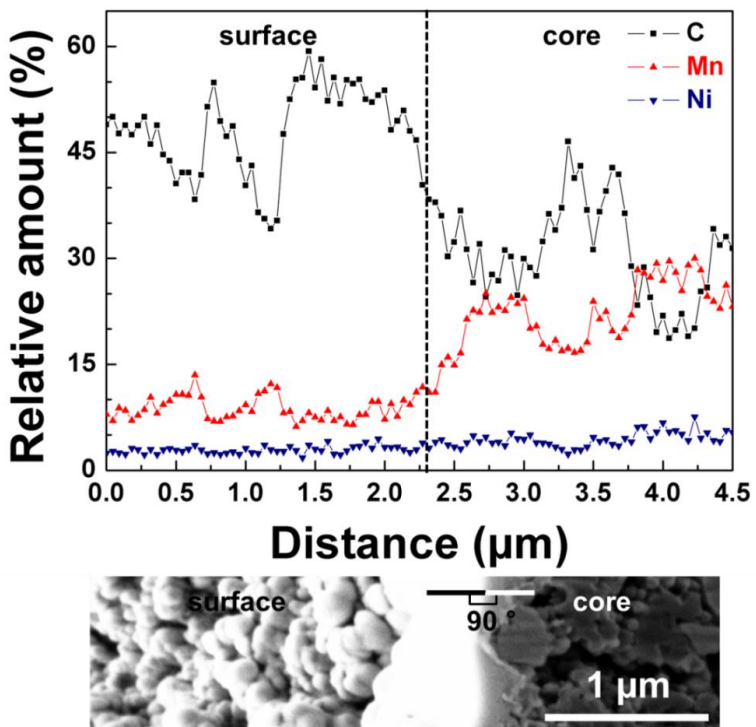


Figure 2.12. Line EDS analysis of the cycled electrode milled by FIB using a gallium ion beam. At the surface, the amount of Ni is greater than that of Mn. In contrast, for the core, the amount of Mn is greater than that of Ni by nearly three times.

The atomic ratio of Mn and Ni measured by ICP-AES analysis was 6.356: 1, which is much higher than that in as-prepared Li-excess material (3: 1).

Mn dissolution is known to be stimulated by the presence of HF, as frequently reported for Mn-based spinel electrode materials.^{32,36} As previously discussed, the decomposition of EC by oxygen radicals yields byproducts such as CO₂ and water.²⁴ In the presence of water, various products such as HF, LiF, POF₃, and PO₄³⁻ can be produced *via* reaction between H₂O and the electrolyte salt (LiPF₆).^{32,36} Schematic reactions are illustrated in Scheme 1 and detailed process can be found in Supporting Information. Among the byproducts, HF in particular is harmful to electrode electrochemical properties. For a manganese-containing electrode, the acidic environment accelerates Mn²⁺ dissolution by the disproportionation reaction of Mn³⁺ to Mn²⁺/Mn⁴⁺ in the electrolyte.^{33,34} Furthermore, HF extracts Li ions chemically from the electrode materials, resulting in the formation of LiF as an insulating layer on the electrode surface. This layer reduces the electrical conductivity and deteriorates the rate capability.³¹ The XPS Li 1s, F 1s, and P 2p spectra (Figure 2.13) confirmed the formation of LiF, POF₃, and PF₅³² resulting from the decomposition of the electrolyte salt. Figure 2.13 shows XPS spectra showing the appearance of various chemical species on the surface of the Li-excess metal oxide electrode after repeated electrochemical cycling. Formation of LiF was observed in both Li 1s and F 1s spectra (Figures 2.13a and 2.13b, respectively). Phosphorus-containing

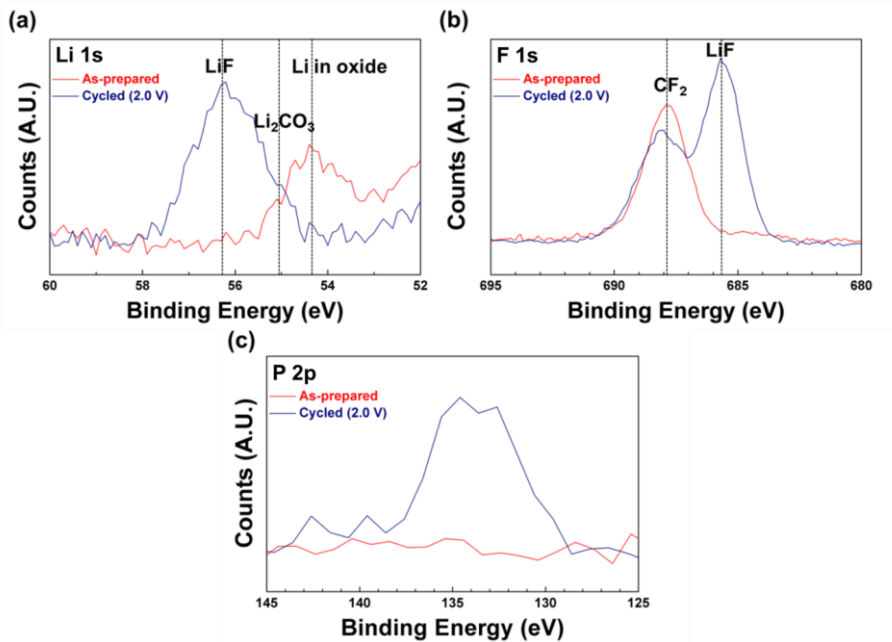
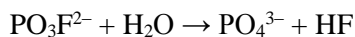
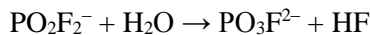
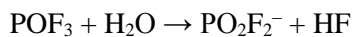
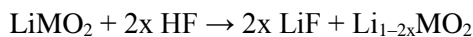


Figure 2.13. XPS (a) Li 1s, (b) F 1s, and (c) P 2p spectra of as-prepared Li-excess transition metal oxide electrode (red) and the fully-discharged electrode after five electrochemical cycles (blue). Various compounds, *e.g.*, LiF, Li₂CO₃, and P-containing species such as POF₃, appeared on the surface of the electrode during cell operation.

compounds were also detected on the surface of the cycled electrode. Both results signify that decomposition of the LiPF₆ salt took place during the electrochemical reaction. The decomposition probably originated from the presence of water molecules inside the cell. In the case of the Li-excess transition metal oxide, the presence of oxygen generates water molecules as a result of a series of reactions, in particular the reaction between ethylene carbonate (EC) and oxygen radicals. The detailed reactions involving water generation are discussed in Section S3. When the LiPF₆ salt and water react, an acidic species, HF, and an insulating compound, LiF, are formed *via* the following successive reactions:^{35,36}



The hydrofluoric acid attacks the active materials in the phases of the layered and spinel structures. The surface of the electrode materials can be damaged by HF through the following reactions:^{36, 37}



As a result of these reactions, the electrochemical performances of the

cells diminish. Because LiF is an insulating material, precipitation of LiF on the electrode surface significantly reduces the electrical conductivity of the electrode. This degrades the rate capability of the cell. The dissolution of Mn²⁺ ions into the electrolyte results in capacity reduction. The final structure of the Li-excess nickel-manganese oxide after the activation of the Mn^{3+/4+} redox couple has the characteristics of both the layered and the spinel compounds.^{15,16} Thus, we believe that the electrochemical properties of the Li-excess metal oxide materials are limited by the formation of these byproducts, which stem from reactions of water that originated from oxygen evolved during the first charging process.

This implies that the degradation of the electrochemical properties of the LLNMO occurs because of hydrolysis in which water molecules are derived from oxygen evolution within the cell. The byproducts formed in the succession of reactions are capable of damaging the surface of the electrode. The significant inhomogeneity of the transition metal components on the surface due to metal dissolution affects the cycle life and rate capability.

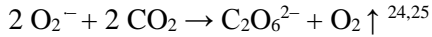
Based on the results above, I summarized the successive reactions inside the closed system originated from the oxygen evolution out of the layered Li-excess transition metal oxides in Figure 2.14. According to the proposed mechanisms, the several reports on the improvement of cyclability and rate capability by coating inorganic materials onto the surface of the layered Li-excess materials^{24,38} can be clearly understood. We believe that a coated layer protects the surface of the electrodes from the harsh acidic environment

developed from oxygen evolution over a longer operating time. Additionally, the crystalline structure near the surface through which the Li^+ ions pass can also be protected against Mn dissolution by this type of surface treatment.

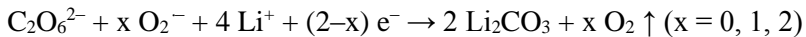
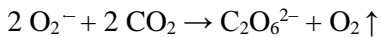
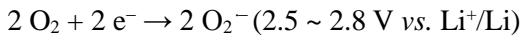
2.1.4. Conclusion

In conclusion, we identified the critical role of the oxygen evolved from the lattice of layered Li-excess metal oxides in Li rechargeable batteries. In coin-type electrochemical cells made with Li-excess materials, partially-reversible formation and decomposition of Li_2CO_3 occurred, similar to the mechanism known for Li-air batteries having a carbonate-based electrolyte (Figure 2.14). It is believed that oxygen radicals are responsible for the formation of Li_2CO_3 during the discharging process of Li-air batteries.^{24,25} In contrast to Li-air batteries, there is no external source of oxygen in the case of coin-type Li-ion cells. However, oxygen extracted from the lattice can play a similar role to oxygen gas. The following is a proposed reaction mechanism for each step of the electrochemical cycling based on FTIR and DEMS analyses.

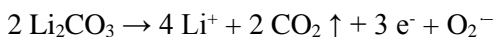
Oxygen evolution from the lattice of the Li-excess metal oxide occurs at the end of the first charging process (from 4.5 V). Some oxygen is assumed to be evolved as free radicals. In the presence of a carbonate-based electrolyte such as EC, the oxygen radicals can carry out the ring-opening reaction of EC and form various byproducts as follows:



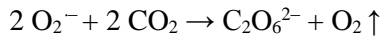
During discharge, dissolved oxygen gas molecules in the electrolyte can become radicals, analogous to the discharging process in Li-air batteries. The oxygen radicals further react with electrolyte and CO₂. Lithium ions not only intercalate into the LLNMO but also react with byproducts forming Li₂CO₃.



According to the mechanism proposed by Freunberger *et al.*,²⁴ the decomposition of Li₂CO₃ in Li-air batteries follows the path below. We believe that the same reaction occurs in our system.



The reaction occurs at a voltage above 4.0 V. This path is consistent with the DEMS results indicating that CO₂ and CO generation starts above 4.0 V. Furthermore, in case of a coin-type cell or commercial Li-ion batteries, *i.e.*, in a “closed” system, CO₂ gas trapped in the cell and O₂⁻ radicals can further react inside the cell:



Also, oxygen radicals react with a carbonate-based electrolyte in the presence of oxygen gas:



While the reversible Li_2CO_3 formation can contribute to the high capacity of this class of materials, the H_2O byproduct resulting from the decomposition of carbonate-based electrolytes can easily hydrolyze the electrolyte salt (LiPF_6) to generate HF , LiF , and POF_3 . The acidic species attacks metal oxide electrodes and lead to surface damage that deteriorates the electrochemical performance of the electrode in terms of cyclability and rate capability. Trapping the oxygen radicals using a scavenger, or protecting the surface of the electrodes, could reduce the performance degradation. We expect that improved control of oxygen evolution in Li-air batteries will impact development in the area of layered Li-excess metal oxide Li rechargeable batteries and *vice versa*.

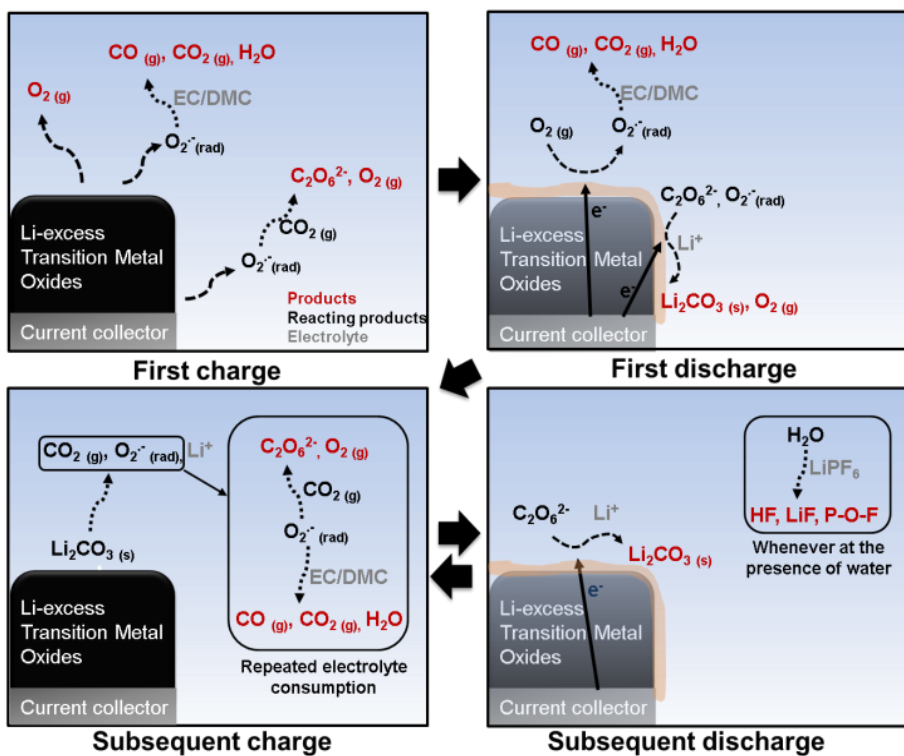


Figure 2.14. Scheme of the proposed mechanism of the successive reactions inside the closed system originated from the oxygen evolution out of the layered Li-excess metal oxides.

2.1.5. References

- 1 Tarascon, J. M. & Armand, M. Issues and challenges facing rechargeable lithium batteries. *Nature* **414**, 359-367 (2001).
- 2 Armand, M. & Tarascon, J. M. Building better batteries. *Nature* **451**, 652-657, doi:10.1038/451652a (2008).
- 3 Kang, K., Meng, Y. S., Breger, J., Grey, C. P. & Ceder, G. Electrodes with high power and high capacity for rechargeable lithium batteries. *Science* **311**, 977-980, doi:10.1126/science.1122152 (2006).
- 4 Tarascon, J. M., Wang, E., Shokoohi, F. K., Mckinnon, W. R. & Colson, S. The Spinel Phase of Limn₂O₄ as a Cathode in Secondary Lithium Cells. *Journal of The Electrochemical Society* **138**, 2859-2864, doi:10.1149/1.2085330 (1991).
- 5 Ohzuku, T., Ueda, A., Nagayama, M., Iwakoshi, Y. & Komori, H. Comparative-Study of LiCoO₂, LiNi_{1/2}Co_{1/2}O₂ and LiNiO₂ for 4-Volt Secondary Lithium Cells. *Electrochimica Acta* **38**, 1159-1167, doi:10.1016/0013-4686(93)80046-3 (1993).
- 6 Kang, B. & Ceder, G. Battery materials for ultrafast charging and discharging. *Nature* **458**, 190-193, doi:10.1038/nature07853 (2009).
- 7 Park, Y.-U. *et al.* Synthesis of Multicomponent Olivine by a Novel Mixed Transition Metal Oxalate Coprecipitation Method and Electrochemical Characterization. *Chemistry of Materials* **22**, 2573 (2010).
- 8 Seo, D. H., Gwon, H., Kim, S. W., Kim, J. & Kang, K. Multicomponent Olivine Cathode for Lithium Rechargeable Batteries: A First-Principles Study. *Chemistry of Materials* **22**, 518-523, doi:10.1021/cm903138s (2010).
- 9 Padhi, A. K., Nanjundaswamy, K. S. & Goodenough, J. B. Phospho-olivines as positive-electrode materials for rechargeable lithium

- batteries. *Journal of the Electrochemical Society* **144**, 1188-1194 (1997).
- 10 Zhonghua, L., MacNeil, D. D. & Dahn, J. R. Layered Cathode Materials $\text{Li}[\text{Ni}_x\text{Li}_{(1/3 - 2x/3)}\text{Mn}_{(2/3 - x/3)}]\text{O}_2$ for Lithium-Ion Batteries. *Electrochemical and Solid-State Letters* **4**, A191-A194 (2001).
- 11 Kim, J.-S. et al. Electrochemical and Structural Properties of $x\text{Li}_2\text{M}'\text{O}_3(1-x)\text{LiMn}_{0.5}\text{Ni}_{0.5}\text{O}_2$ Electrodes for Lithium Batteries ($\text{M}' = \text{Ti}, \text{Mn}, \text{Zr}; 0 < x < 0.3$). *Chemistry of Materials* **16**, 1996-2006 (2004).
- 12 Zhonghua, L. & Dahn, J. R. Understanding the Anomalous Capacity of $\text{Li}/\text{Li}[\text{Ni}_x\text{Li}_{(1/3 - 2x/3)}\text{Mn}_{(2/3 - x/3)}]\text{O}_2$ Cells Using In Situ X-Ray Diffraction and Electrochemical Studies. *Journal of The Electrochemical Society* **149**, A815-A822 (2002).
- 13 Armstrong, A. R. et al. Demonstrating Oxygen Loss and Associated Structural Reorganization in the Lithium Battery Cathode $\text{Li}[\text{Ni}_{0.2}\text{Li}_{0.2}\text{Mn}_{0.6}]\text{O}_2$. *Journal of the American Chemical Society* **128**, 8694-8698, doi:10.1021/ja062027+ (2006).
- 14 Robertson, A. D. and Bruce, P. G. Mechanism of Electrochemical Activity in Li_2MnO_3 . *Chemistry of Materials* **15**, 1984-1992, doi:10.1021/cm030047u (2003).
- 15 Hong, J. et al. Structural evolution of layered $\text{Li}_{1.2}\text{Ni}_{0.2}\text{Mn}_{0.6}\text{O}_2$ upon electrochemical cycling in a Li rechargeable battery. *Journal of Materials Chemistry* **20**, 10179-10186 (2010).
- 16 Yabuuchi, N., Yoshii, K., Myung, S.-T., Nakai, I. & Komaba, S. Detailed Studies of a High-Capacity Electrode Material for Rechargeable Batteries, $\text{Li}_2\text{MnO-LiCo}_{1/3}\text{Ni}_{1/3}\text{Mn}_{1/3}\text{O}_2$. *Journal of the American Chemical Society* **133**, 4404-4419 (2011).
- 17 Xu, B., Fell, C. R., Chi, M. & Meng, Y. S. Identifying surface structural changes in layered Li-excess nickel manganese oxides in high voltage lithium ion batteries: A joint experimental and

- theoretical study. *Energy & Environmental Science* **4**, 2223-2233 (2011).
- 18 Tran, N. *et al.* Mechanisms Associated with the Plateau Observed at High Voltage for the Overlithiated $\text{Li}_{1.12}(\text{Ni}_{0.425}\text{Mn}_{0.425}\text{Co}_{0.15})_{0.88}\text{O}_2$ System. *Chemistry of Materials* **20**, 4815-4825 (2008).
- 19 Jiang, M., Key, B., Meng, Y. S. & Grey, C. P. Electrochemical and Structural Study of the Layered, "Li-Excess" Lithium-Ion Battery Electrode Material $\text{Li}[\text{Li}_{1/9}\text{Ni}_{1/3}\text{Mn}_{5/9}]\text{O}_2$. *Chemistry of Materials* **21**, 2733-2745, doi:10.1021/cm900279u (2009).
- 20 Lei, C. H. *et al.* Local structure and composition studies of $\text{Li}_{1.2}\text{Ni}_{0.2}\text{Mn}_{0.6}\text{O}_2$ by analytical electron microscopy. *Journal of Power Sources* **178**, 422-433 (2008).
- 21 Hui, Y., Hyunjoo, B., Khalil, A. & Jai, P. Investigations of the Exothermic Reactions of Natural Graphite Anode for Li-Ion Batteries during Thermal Runaway. *Journal of The Electrochemical Society* **152**, A73-A79 (2005).
- 22 MacNeil, D. D., Lu, Z., Chen, Z. & Dahn, J. R. A comparison of the electrode/electrolyte reaction at elevated temperatures for various Li-ion battery cathodes. *Journal of Power Sources* **108**, 8-14 (2002).
- 23 Baba, Y., Okada, S. & Yamaki, J.-i. Thermal stability of Li_xCoO_2 cathode for lithium ion battery. *Solid State Ionics* **148**, 311-316 (2002).
- 24 Freunberger, S. A. *et al.* Reactions in the Rechargeable Lithium-O₂ Battery with Alkyl Carbonate Electrolytes. *Journal of the American Chemical Society* **133**, 8040-8047, doi:10.1021/Ja2021747 (2011).
- 25 Takechi, K., Shiga, T. & Asaoka, T. A Li-O₂/CO₂ battery. *Chemical Communications* **47**, 3463-3465 (2011).
- 26 McCloskey, B. D., Bethune, D. S., Shelby, R. M., Girishkumar, G. & Luntz, A. C. Solvents' Critical Role in Nonaqueous Lithium-Oxygen Battery Electrochemistry. *The Journal of Physical Chemistry Letters*

- 2**, 1161-1166 (2011).
- 27 Aurbach, D. *et al.* The Correlation between the Surface-Chemistry and the Performance of Li-Carbon Intercalation Anodes for Rechargeable Rocking-Chair Type Batteries. *Journal of The Electrochemical Society* **141**, 603-611, doi:10.1149/1.2054777 (1994).
- 28 Gibian, M. J., Sawyer, D. T., UngermaNN, T., Tangpoonpholvivat, R. & Morrison, M. M. Reactivity of Superoxide Ion with Carbonyl-Compounds in Aprotic-Solvents. *Journal of the American Chemical Society* **101**, 640-644, doi:10.1021/JA00497a026 (1979).
- 29 Lu, Y., Goodenough, J. B. & Kim, Y. Aqueous Cathode for Next-Generation Alkali-Ion Batteries. *Journal of the American Chemical Society* **133**, 5756-5759, doi:10.1021/ja201118f (2011).
- 30 Wu, Z. S. *et al.* A LiF Nanoparticle-Modified Graphene Electrode for High-Power and High-Energy Lithium Ion Batteries. *Adv Funct Mater* **22**, 3290-3297, doi:10.1002/adfm.201200534 (2012).
- 31 Bruce, P. G., Freunberger, S. A., Hardwick, L. J. & Tarascon, J. M. Li-O₂ and Li-S batteries with high energy storage. *Nat Mater* **11**, 19-29, doi:10.1038/Nmat3191 (2012).
- 32 Oh, S. M. *et al.* High-Performance Carbon-LiMnPO₄ Nanocomposite Cathode for Lithium Batteries. *Adv Funct Mater* **20**, 3260-3265, doi:10.1002/adfm.201000469 (2010).
- 33 Plakhotnyk, A. V., Ernst, L. & Schmutzler, R. Hydrolysis in the system LiPF₆-propylene carbonate-dimethyl carbonate-H₂O. *J Fluorine Chem* **126**, 27-31, doi:10.1016/j.jfluchem.2004.09.027 (2005).
- 34 Wieghardt, K. The Active-Sites in Manganese-Containing Metalloproteins and Inorganic Model Complexes. *Angewandte Chemie-International Edition in English* **28**, 1153-1172, doi:10.1002/anie.198911531 (1989).

- 35 Ken, T., Katsuya, K., Shinichiro, N. & Makoto, U. Decomposition of LiPF₆ and Stability of PF₅ in Li-Ion Battery Electrolytes. *Journal of The Electrochemical Society* **150**, A1628-A1636 (2003).
- 36 Nakajima, T. & Groult, H. *Fluorinated materials for energy conversion*. (Elsevier, 2005).
- 37 Wieghardt, K. The Active Sites in Manganese-Containing Metalloproteins and Inorganic Model Complexes. *Angewandte Chemie International Edition in English* **28**, 1153-1172 (1989).
- 38 Kang, S. H. & Thackeray, M. M. Enhancing the rate capability of high capacity xLi₂MnO₃-(1-x)LiMO₂ (M = Mn, Ni, Co) electrodes by Li-Ni-PO₄ treatment. *Electrochemistry communications* **11**, 748-751, doi:10.1016/j.elecom.2009.01.025 (2009).

2.2 High energy layered Li-excess nickel-manganese oxide electrodes without voltage decay

2.2.1. Research background

Breakthrough enhancement of the energy density of current lithium-ion batteries is one of the grand challenges in green energy technologies such as electric automobiles and large-scale power backups.¹ As a key step toward it, great efforts are being made to develop new electrode materials with higher reversible energy densities. Among the various cathode materials that have been studied to date, the layered Li-excess transition metal oxides ($\text{Li}[\text{Li}_x\text{Ni}_y\text{Mn}_{(1-x-y)}]\text{O}_2$, $0 < x < 0.33$, $0 < y < 0.5$ hereafter called LLNMO), are of particular interest due to their extraordinarily high reversible capacities ($> 230 \text{ mAh g}^{-1}$) and relatively high operating voltage ($\sim 3.6 \text{ V vs. Li/Li}^+$ on average).²

In typical Ni–Mn-based layered materials, the $\text{Ni}^{n+}/\text{Ni}^{4+}$ ($2 \leq n \leq 3$) redox reaction is electrochemically active, *i.e.*, it contributes to the reversible capacity, while electrochemically inactive Mn^{4+} ions stabilize the lattice framework.^{2–4} Therefore, several research groups have described LLNMO as structurally integrated composites of inactive Li_2MnO_3 and active LiMO_2 , *i.e.*, $z\text{Li}_2\text{MnO}_3-(1-z)\text{LiMO}_2$ ($\text{M} = \text{Ni, Mn}$, $0 < z < 1$).^{5,6} However, the observed capacity from LLNMO far exceeds the theoretical values based on the redox couples of LiMO_2 components in the materials.^{2,5,6} Also, the high capacity of LLNMO is only available after an initial charging process beyond a voltage plateau of 4.5–4.6 V. Furthermore, recent studies have

shown that the cathode potential of LLNMO continuously decreases as electrochemical cycle proceeds. While the precise mechanism for these unusual behaviors is yet to be unveiled; thus intense research is still actively progressing, earlier works by Lu *et al.*⁷ suggested that the initial extra charging capacity beyond nickel redox reaction occurs by the simultaneous Li⁺ and O²⁻ extraction instead of the transition metal oxidation at the voltage plateau of 4.5–4.6 V. Later, Armstrong *et al.*⁸ confirmed the evolution of oxygen gas by *in situ* differential electrochemical mass spectroscopy (DEMS). Some researchers observed that a structural transformation occurs after the release of oxygen gas, and it is necessary to achieve the high discharge capacity from these materials.^{5,8-10} We previously reported that this structural transformation is related to the local layered-to-spinel-like phase transition *via* cation migration during cycling and activates Mn⁴⁺/Mn³⁺ redox reaction at lower potential region, thus lowering the overall voltage.¹¹ It was later confirmed by Bo *et al.*¹², who identified tetrahedral lithium ions and the migration of transition metal ions. Yabuuchi *et al.*⁶ also observed a bulk structural rearrangement that included a cation migration from a transition metal layer to a lithium layer in the cobalt-doped layered Li-excess material.

The issue of voltage suppression of this class of materials was firstly tackled by Sathiya *et al.*¹³, who recently suggested a new Li-excess model material, Li₂Ru_{1-x}Sn_xO₃. This series of materials exhibited both reversible anionic ($2\text{O}^{2-} \leftrightarrow \text{O}_2^{2-}$) and cationic redox reaction (Ru⁴⁺/Ru⁵⁺). During the initial charge, the irreversible oxygen gas evolution could be minimized due

to the ready anionic redox reaction in this material. As a result, it could reduce the irreversible cation rearrangement and remarkably suppress the corresponding voltage depression. While this new Li-excess material group suggested a new way to overcome the voltage suppression, it was necessary to use heavy $4d$ transition metals such as Ru and Sn to utilize the oxygen redox reaction, thus is different from nickel or manganese chemistry in LLNMOs. The use of heavy $4d$ transition metals is believed to be required to promote the hybridization with oxygen orbitals and the utilization of its redox reaction. However, it substantially lowers the specific capacity of Li-excess materials and significantly dilutes the advantage of this class of materials.

Here, we demonstrate that the voltage depression in the layered Li-excess nickel manganese oxides can be suppressed without the use of heavy $4d$ transition metals (or occurrence of anionic redox reaction) or doping of third elements, but can be done by a simple substitution of manganese to nickel in $\text{Li}_2\text{MnO}_3\text{-LiMO}_2$ ($\text{M}=\text{Ni, Mn}$). In the present study, we discovered that the configuration of transition metal ions composing LiMO_2 is closely related to the structural evolution and the corresponding redox reaction of LLNMO. The ratio between nickel and manganese ions in LiMO_2 is critical to determine the final structure of LLNMO after cycling-induced transformation, where the layered and spinel-like phases coexist. As the contents of nickel increased in LLNMO, the layered phase dominated the final structure, resulting in the suppressed voltage depression during battery

cycling. The additional activation of nickel redox reaction, regardless of the initial oxidation states of nickel ions in the pristine materials, fully compensates for the capacity loss from the subdued manganese redox reaction.

2.2.2. Experimental details

Sample Preparation

$0.5\text{Li}_2\text{MnO}_3-0.5\text{LiNi}_x\text{Mn}_{1-x}\text{O}_2$ ($x = 0.5, 0.75, 1$), i.e., $\text{Li}_{1.2}\text{Ni}_y\text{Mn}_{0.8-y}\text{O}_2$ ($y = 0.2, 0.3, 0.4$) were prepared by a solid-state reaction from lithium carbonate and nickel-manganese carbonate ($\text{Ni}_y\text{Mn}_{1-y}\text{CO}_3$, $y = 0.25, 0.375, 0.5$). The mixed nickel-manganese carbonate was prepared *via* a co-precipitation method. A 0.2 M mixed nickel sulfate and manganese sulfate aqueous solution ($\text{Ni}:\text{Mn} = 2:6, 3:5, 4:4$) was added drop-wise to an equal volume of a 1 M NaHCO_3 aqueous solution under constant stirring of 250 rpm at 50 °C. The pH was maintained at 9 by adding the desired amount of NH_4OH . The $(\text{NiMn})\text{CO}_3$ precipitate was filtered, rinsed with deionized water several times, and dried overnight at 120 °C. Thus, the obtained powder was mixed with lithium carbonate which is added 3 wt% excess of stoichiometric amount to compensate for the possible lithium evaporation at high temperature. The mixture was heated at 900 °C for 6 hours in air then quenched by soaking the powder in liquid nitrogen.

Compounds Characterization

The chemical formula of the synthesized compounds was determined by

inductively coupled plasma atomic emission spectroscopy (ICP-AES, Thermo Jarrel Ash, Polyscan 60E, USA). The crystal structures of the layered Li-excess nickel-manganese oxides with various compositions were characterized using a D/MAX-2500 X-ray diffractometer (Rigaku, Japan) equipped with Cu-K α radiation ($\lambda = 1.54178 \text{ \AA}$) in the 2θ range of $10 - 75^\circ$. Neutron Diffraction data were collected over a 2θ range of $15 - 155^\circ$ with a step size of 0.05° , and $\lambda = 1.8348 \text{ \AA}$ was supplied by a Ge (331) single-crystal monochromator on a high-resolution powder diffractometer (HRPD) at the HANARO facility at the Korea Atomic Energy Research Institute. Further XRD and ND Rietveld refinement analyses were carried out using FulProf program.¹⁴

Electrochemical Measurement

The electrodes were fabricated by casting the slurry paste consisted of 80 wt% active materials, 10 wt% carbon black (Super-P), and 10 wt % polyvinylidene fluoride (PVdF) onto aluminum foils, the current collector. Coin-type cells (CR2016, Hohsen, Japan) were assembled with the electrodes, the Li metal counter electrode, a separating membrane (Celgard 2400), and a 1 M solution of LiPF₆ in a mixture of ethyl carbonate and dimethyl carbonate (EC/DMC, 1:1 v/v) in an argon-filled glove box. The galvanostatic charging/discharging process was performed for five cycles at 25 °C at 15 mA g⁻¹ at a voltage range of 2.0–4.8 V by a potentio-galvanostat (WonA Tech, WBCS 3000, Korea)

Ex situ Characterization

The electrodes fully discharged to 2.0 V after five electrochemical cycles were retrieved by disassembling the tested cells and rinsed with DMC. The procedures were performed in Ar-filled glove box. X-ray Photoelectron Spectroscopy (XPS) spectra were obtained using an X-ray photoelectron spectrometer (Sigma Probe, Thermo VG Scientific, England) with Al-K α (1487 eV) X-ray source. Ni and Mn K-edge X-ray absorption spectra (XAS) were collected at the beamline BL10C, Pohang Light Source (PLS) in Pohang Accelerator Laboratory, Korea. The Si(1 1 1) double crystal was employed to monochromatize the X-ray photon energy. The monochromator was detuned to 35-45 % of its original intensity to eliminate the high-order harmonics. Mn and Ni K-edge spectra were collected in transmission mode. Energy calibration was carried out using the first inflection point of the spectrum of Mn and Ni metal foil as a reference (i.e., Mn K-edge = 6539 eV and Ni K-edge = 8333 eV). Reference spectra were simultaneously collected for each *in situ* spectrum using Mn or Ni metal foils. The electrode samples were prepared by disassembling the coin cells after the proper electrochemical cycling and sealed in a water-resistant polymer film in the Ar-filled glove box. Analysis of the XAS spectra was conducted by using program code of IFEFFIT.¹⁵

Computational Details

First principles calculations were performed based on density functional theory (DFT) using Perdew-Burke-Ernzerhof (PBE) exchange-correlation parameterization with generalized gradient approximation (GGA).¹⁶ A plane-

wave basis set and the projector-augmented wave (PAW) pseudopotentials¹⁷ were used as implemented in Vienna *ab initio* simulation package (VASP).¹⁸ In order to correct the well-known incomplete description of self-interaction in transition metal oxides, we adopted the Hubbard U parameters (GGA+U).¹⁹ U value of 6.0 eV and 6.96 eV were used for manganese ions and nickel ions, respectively, and J value of 1.0 eV was used for both ions.¹² For the calculation of electronic properties, we modeled repeating unit cell composed of layered $\text{Li}_{32}(\text{Mn}_{16}\text{Ni}_{16})\text{O}_{64}$ and spinel $\text{Li}_{32}\text{Mn}_{32}\text{O}_{64}$ with identical oxygen framework. The geometric optimization was performed with kinetic energy cutoff of 500 eV, and repeated until the remaining force of the system converges within 0.05 eV/Å.

2.2.3. Results and discussion

We prepared a series of LLNMO ($z\text{Li}_2\text{MnO}_3-(1-z)\text{LiMO}_2$) with varying transition metal composition in LiMO_2 components (Figure 2.15a). The amount of Li_2MnO_3 (Figure 2.15b) in LLNMO was fixed at $z = 0.5$, while the ratio of nickel to manganese in LiMO_2 was systematically altered ($M = \text{Ni}_{0.5}\text{Mn}_{0.5}$, $\text{Ni}_{0.75}\text{Mn}_{0.25}$, Ni). Thus, the chemical compositions of the target compounds were $\text{Li}_{1.2}\text{Ni}_y\text{Mn}_{0.8-y}\text{O}_2$ ($y = 0.2, 0.3, 0.4$ hereafter called LL226, LL235, LL244, respectively). The compositions of $\text{Li}_{1.2}\text{Ni}_y\text{Mn}_{0.8-y}\text{O}_2$ measured by inductively coupled plasma-atomic emission spectroscopy (ICP-AES) were $\text{Li}_{1.145}\text{Ni}_{0.212}\text{Mn}_{0.643}\text{O}_2$, $\text{Li}_{1.155}\text{Ni}_{0.311}\text{Mn}_{0.535}\text{O}_2$, and $\text{Li}_{1.161}\text{Ni}_{0.417}\text{Mn}_{0.423}\text{O}_2$, which are close to the target compositions.

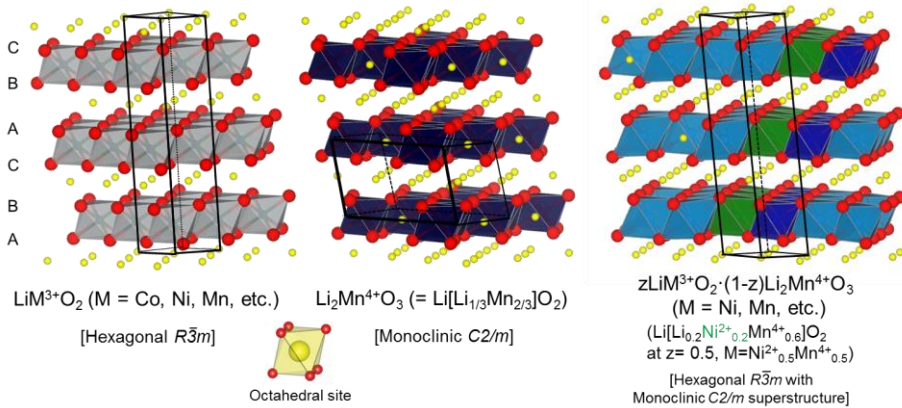


Figure 2.15. Crystal structure of LiMO_2 ($\text{M}=\text{Ni, Mn}$) with $R\bar{3}m$ symmetry, Li_2MnO_3 with $C2/m$ symmetry and $z\text{LiMO}_2 \cdot (1-z)\text{Li}_2\text{MnO}_3$.

The crystal structures of as-prepared LLNMOs were carefully investigated by the diffraction study using both X-ray (XRD) and neutron (ND) radiation. The XRD patterns of the materials correspond to O3-type structures that can be indexed by $R\bar{3}m$ symmetry with superstructure patterns of $C2/m$ symmetry without impurities (Figure 2.16).² The superstructure patterns in the 2θ range of 20–25° originate from the presence of honeycomb-like transition metal-lithium ordering in the transition metal layers.^{20,21} The weaker superstructure patterns in LL244 is attributable to more disordered atomic configurations in transition metal layers^{22,23} compared to LL226. The ND patterns of the LLNMO compounds varied more appreciably than XRD patterns along the compositional change due to the difference in neutron scattering lengths of nickel (10.3 fm) and manganese (-3.73 fm)²⁴ as shown in Figure 2.17. The intensity of the (003) peak at 22.4° gradually increased with the nickel content, while that of the (012) peak at 46.2° significantly decreased compared to the (104) peak at 53.6°. This observation is consistent with the results of ND pattern simulation in Figure 2.18, and is attributed to stronger scattering of neutron by nickel compared to manganese.

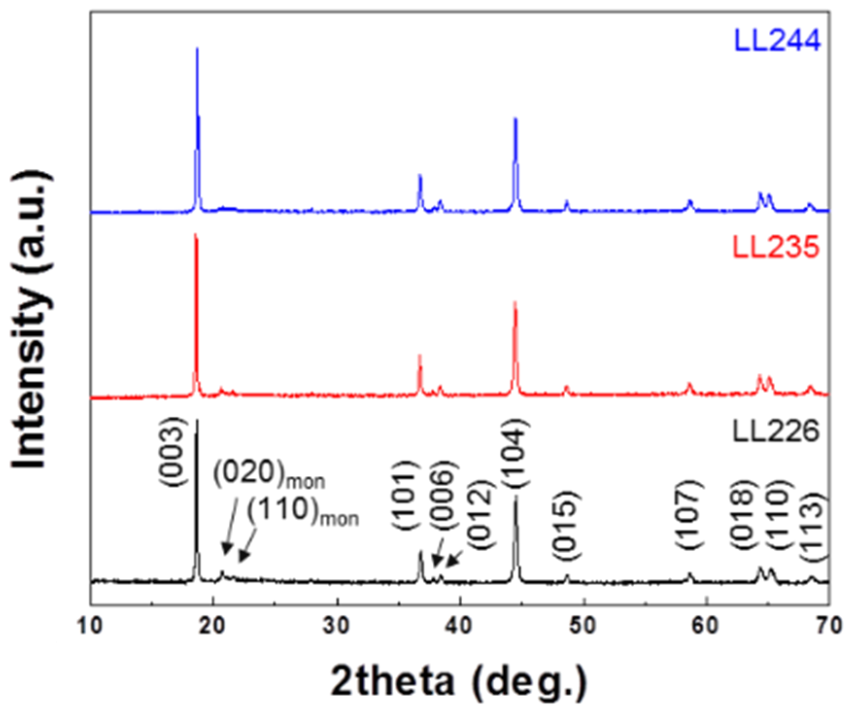


Figure 2.16. XRD patterns of pristine LL226 (black), LL235 (red), and LL244 (blue).

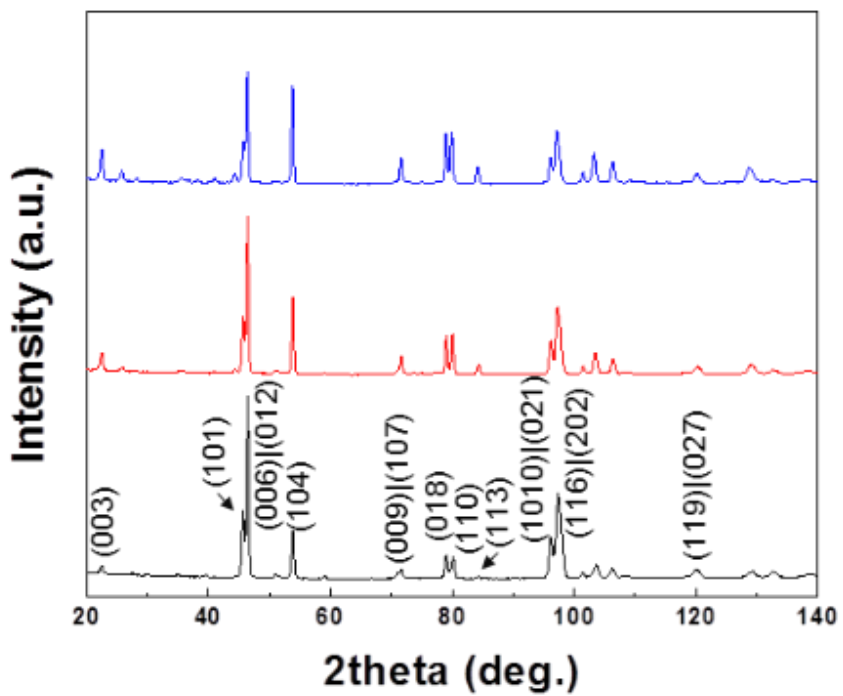


Figure 2.17. ND patterns of pristine LL226 (black), LL235 (red), and LL244 (blue).

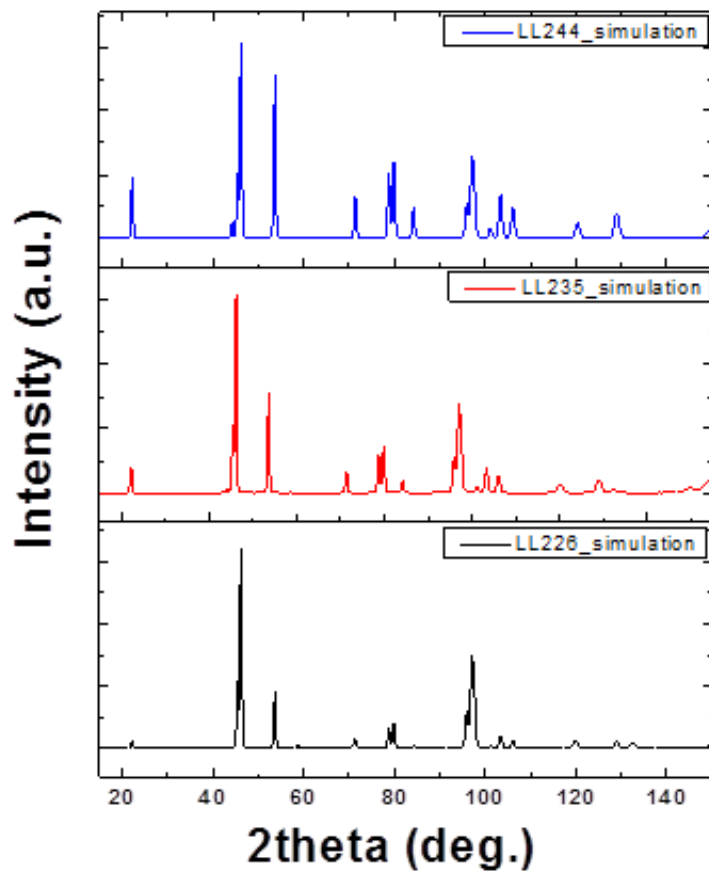


Figure 2.18. Simulated neutron diffraction patterns of LL226 (black), LL235 (red), and LL244 (blue).

However, we could not locate any superstructure pattern from Ni-Mn ordering in the ND, which implies the absence of long-range orderings between nickel and manganese in the transition metal layers of LLNMO. The lattice parameters and atomic occupancies of the series of LLNMO compounds were obtained by Rietveld refinements of the XRD and ND patterns, which are summarized in Tables 2.1-2.5 and Figures 2.19 and 2.20. The changes in lattice parameters that follow Vegard's law were observed, indicative of the gradual changes in the compositions of Ni/Mn within the layered framework. We found that the oxidation states of each transition metal ions varied as a result of the changes in Ni/Mn ratios. The X-ray absorption near-edge structure (XANES) of Ni K-edge show that the pristine materials contain more oxidized nickel ions in the structure as the nickel contents increase (Figure 2.21a), which agrees with the targeted oxidation states of +2, +2.67 and +3 for LL226, LL235, and LL244, respectively. In contrast, Mn K-edge spectra indicate that the oxidation states of manganese remain unchanged as +4 regardless of the Ni/Mn ratio in all the compounds (Figure 2.21b).

Table 2.1. The detailed data for the structural refinement of LLNMO using XRD patterns

Source	X-ray		
Formula	Li _{1.2} Ni _{0.2} Mn _{0.6} O ₂	Li _{1.2} Ni _{0.3} Mn _{0.5} O ₂	Li _{1.2} Ni _{0.4} Mn _{0.4} O ₂
Crystal system	Rhombohedral	Rhombohedral	Rhombohedral
Space group	$R\bar{3}m$	$R\bar{3}m$	$R\bar{3}m$
Lattice parameters			
a (Å)	2.858586 (4)	2.861556 (4)	2.866193 (3)
c (Å)	14.26113319 (19)	14.25193310 (15)	14.24773979 (13)
Unitcell volume (Å³)	100.922 (0.022)	101.0667 (0.018)	101.365 (0.016)
Formula weight	85.03	85.41	85.78
Temperature (K)	300	300	300
Wave length (Å)	1.54059	1.54059	1.54059
2θ range	10 - 80°	10 - 80°	10 - 80°
Number of data points	7000	7000	7000
Step size	0.01°	0.01°	0.01°
R_p (%)	2.55	2.38	2.60
R_I (%)	8.65	6.50	4.90
R_F (%)	7.61	6.55	4.35
χ²	1.77	1.36	1.93

Table 2.2. The detailed data for the structural refinement of LLNMO using ND patterns

Source	Neutron		
Formula	Li _{1.2} Ni _{0.2} Mn _{0.6} O ₂	Li _{1.2} Ni _{0.3} Mn _{0.5} O ₂	Li _{1.2} Ni _{0.4} Mn _{0.4} O ₂
Crystal system	Rhombohedral	Rhombohedral	Rhombohedral
Space group	$R\bar{3}m$	$R\bar{3}m$	$R\bar{3}m$
Lattice parameters			
a (Å)	2.857693 (3)	2.8605032 (3)	2.8654940 (2)
c (Å)	14.25090 (1)	14.24536 (1)	14.24227 (1)
Unitcell volume (Å³)	100.787 (0.000)	100.946 (0.000)	101.277 (0.000)
Formula weight	85.03	85.41	85.78
Temperature (K)	300	300	300
Wave length (Å)	1.834333	1.834333	1.834333
2θ range	0 - 160°	0 - 160°	0 - 160°
Number of data points	3200	3200	3200
Step size	0.05	0.05	0.05
R_p (%)	4.53	3.59	3.22
R_I (%)	6.73	3.44	3.04
R_F (%)	7.13	2.67	2.25
χ²	8.79	6.81	5.14

Table 2.3. The atomic positions and occupancies in LL226 using ND patterns

Atom	x	y	z	B_{iso}	Occupancy
Li1	0	0	0.5	0.99 (9)	0.971 (1)
Ni1	0	0	0.5	0.99 (9)	0.030 (1)
Li2	0	0	0	0.04 (13)	0.229 (1)
Ni2	0	0	0	0.04 (13)	0.171 (1)
Mn2	0	0	0	0.04 (13)	0.6
O1	0	0	0.25852 (6)	1.48 (3)	1.0

Table 2.4. The atomic positions and occupancies in LL235 using ND patterns

Atom	x	y	z	B_{iso}	Occupancy
Li1	0	0	0.5	0.31(9)	0.969 (8)
Ni1	0	0	0.5	0.31(9)	0.030 (8)
Li2	0	0	0	0.8 (3)	0.217 (8)
Ni2	0	0	0	0.8 (3)	0.271 (8)
Mn2	0	0	0	0.8 (3)	0.5
O1	0	0	0.25855 (5)	0.33 (2)	1.0

Table 2.5. The atomic positions and occupancies in LL244 using ND patterns

Atom	x	y	Z	B_{iso}	Occupancy
Li1	0	0	0.5	1.21 (11)	0.962 (8)
Ni1	0	0	0.5	1.21 (11)	0.026 (8)
Li2	0	0	0	0.08 (7)	0.208 (8)
Ni2	0	0	0	0.08 (7)	0.383 (8)
Mn2	0	0	0	0.08 (7)	0.4
O1	0	0	0.25830 (7)	0.51 (2)	1.0

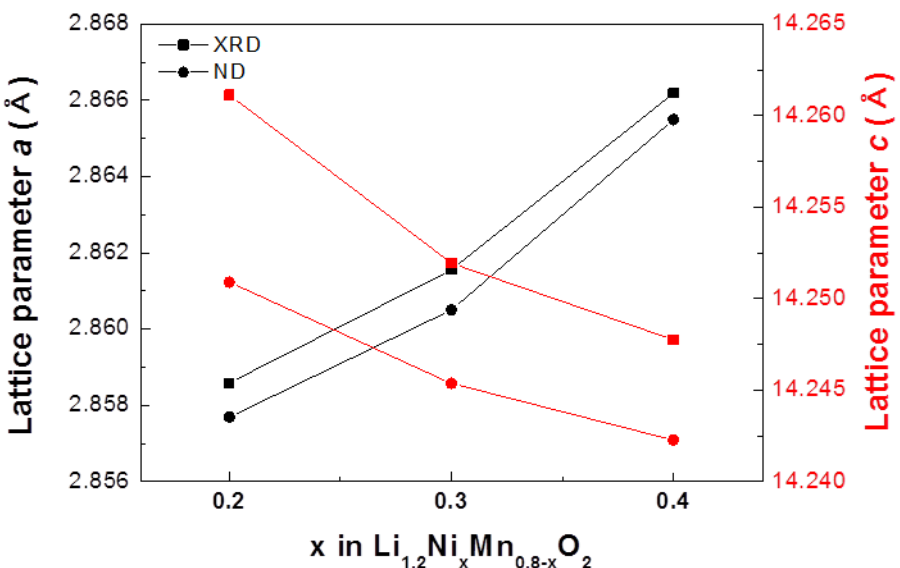


Figure. 2.19. Lattice parameters of LL226, LL235, and LL244 observed by XRD and ND analyses.

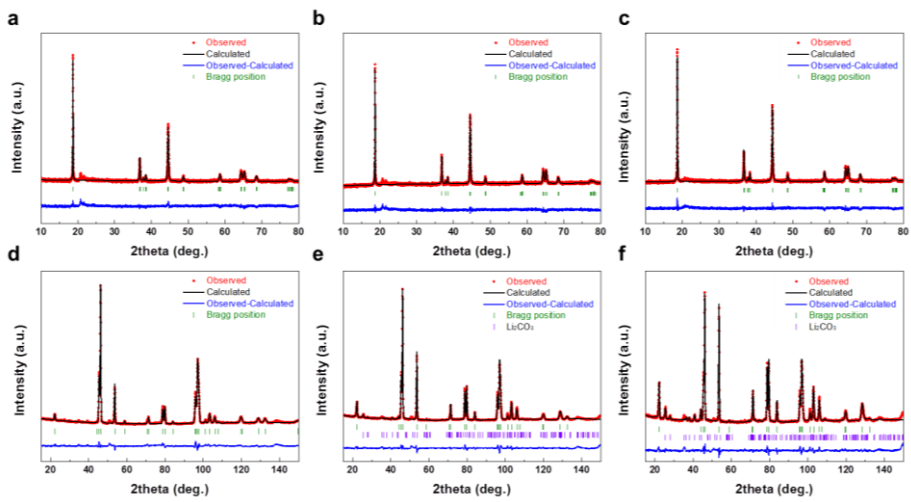


Figure 2.20. Rietveld refinements of the a, b, c) XRD patterns and d, e, f) ND patterns of LL226, LL235, and LL244 (left to right). R-factors for XRD and ND patterns are represented in Table 2.1 and 2.2.

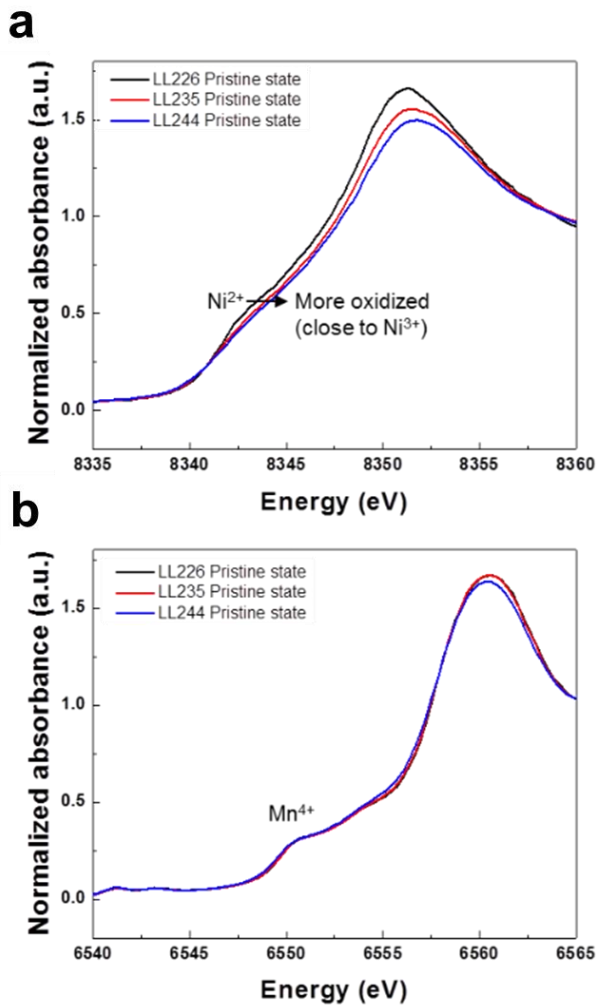


Figure 2.21. XANES a) Ni K-edge spectra, and b) XANES Mn K-edge spectra of pristine LL226 (black), LL235 (red), and LL244 (blue).

The electrochemical activity of each LLNMO was galvanostatically measured versus lithium metal at a current density of 15 mA g⁻¹ in the voltage range of 2.0–4.8 V (Figure 2.22a). During the initial charging process, a plateau at 4.4–4.5 V was observed in all cases implying that the oxygen evolution commonly occurs in 0.5Li₂MnO₃–0.5LiMO₂ compounds.^{8,25} The initial charging capacities of LL226, LL235 and LL244 were 357, 352 and 343 mAh g⁻¹ corresponding to almost all Li extraction from the materials (~1.20 Li⁺ per formula unit), respectively. The initial charge process is comprised of two reactions of (i) the anionic oxidation of oxygen ions (> 4.5 V)^{8,25} and (ii) the oxidation of nickel ions to tetravalent states (< 4.5 V). The differential capacity plots (dq/dV) show that the anodic reaction potentials in the first cycle were almost identical for all compounds regardless of the compositions comprising of two peaks; one at around 3.8V corresponding to Ni²⁺/Ni⁴⁺ (LL226), Ni^{2.67+}/Ni⁴⁺ (LL235) or Ni³⁺/Ni⁴⁺(LL244) and the other at around 4.5V corresponding to oxygen oxidation (Figure 2.22b) However, upon discharge, three different cathodic reactions were observed at 3.25 V, 3.7 V, and 4.25 V. It is noteworthy that the intensity ratio for the peaks at 3.25 and 3.7 V varied significantly with the composition. The difference in electrochemical reactions of LLNMOs is more clearly observed in the charge/discharge profiles of the fifth cycle as shown in Figure 2.23a and 2.23b. The discharge capacity at 3.25 V dominates the total area of the discharge reactions for LL226, while the initial charge voltage of LL226 was much higher.

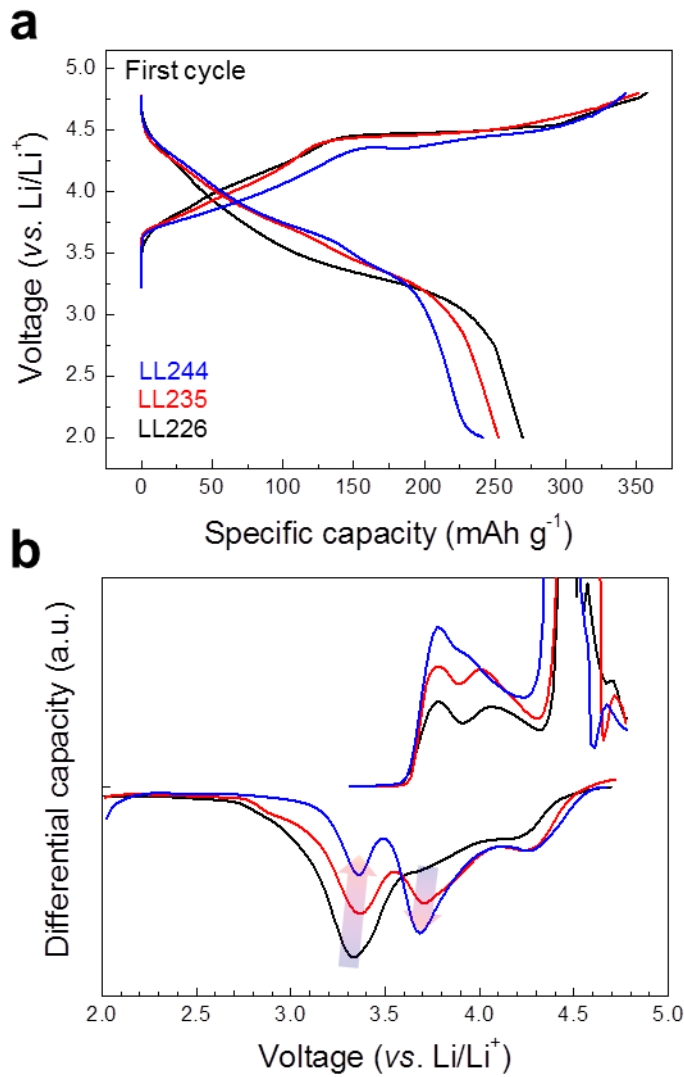


Figure 2.22. a) Charge/discharge profiles and b) differential capacity curves of LL226 (black), LL235 (red), and LL244 (blue) of the first cycle.

It clearly demonstrates the voltage suppression that Li-excess materials typically suffer from. On the other hand, we found that the voltage decay is significantly subdued as the nickel contents increases to LL244. The discharge capacity at 3.25 V accounts for the only small fraction for LL244. For a more clear comparison, we calculated the capacity contribution from different potential regions for each sample in Figure 2.24a. The discharge capacity from 3.4 V and above accounted for 48%, 60%, and 68% of the total discharge capacity of LL226, LL235, and LL244, respectively. As results, the average cathodic (discharge) potential of the LLNMO increased along the nickel content, from 3.49 V for LL226 to 3.66 V for LL244. Nevertheless, the average anionic potential values were similar to each other as comparatively shown in Figure 2.24b. It indicates that the energy efficiency of the electrode also has been enhanced with higher nickel contents. The relatively large polarization of LL226 is attributed to the sluggish redox reaction at 3.25 V, which was previously reported to be related to the cationic disorder and cubic-like phase formation on the surface of the layered framework.

Variation in the redox potentials after the initial charge strongly suggests that the evolution of lithium environments follows distinct ways for each Li-excess material with different ratios of nickel and manganese. Accordingly, we analyzed the structures of LLNMOs after the voltage decay using various tools including XRD, Raman spectroscopy, and high-resolution transmission electron microscopy (HR-TEM).

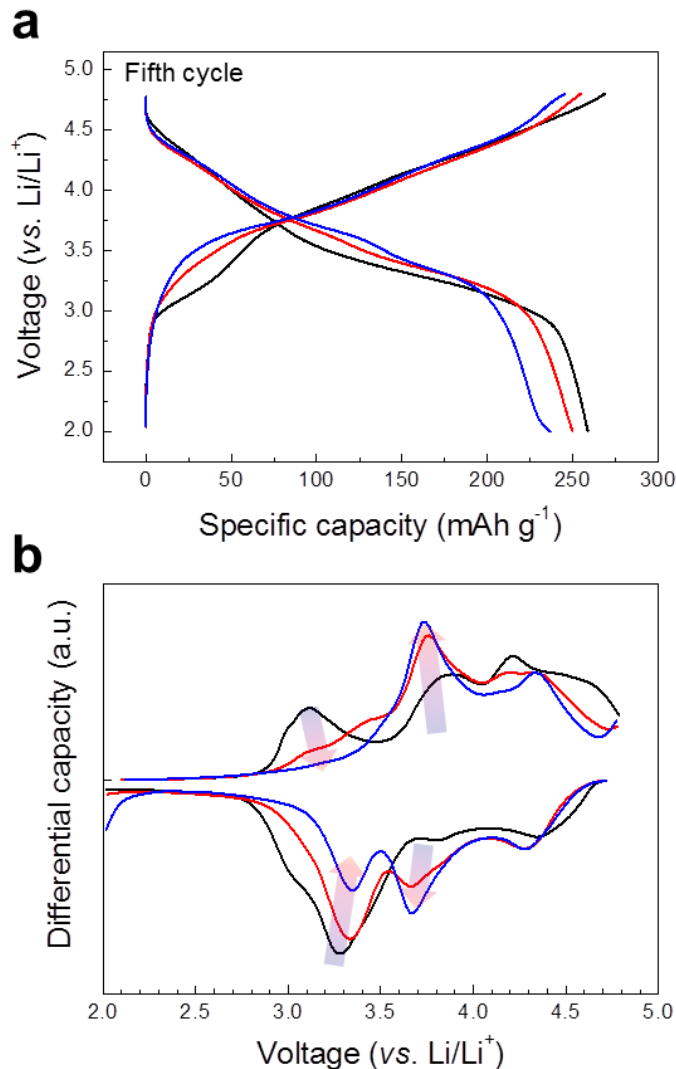


Figure 2.23. a) Charge/discharge profiles and b) differential capacity curves of LL226 (black), LL235 (red), and LL244 (blue) of the fifth cycle.

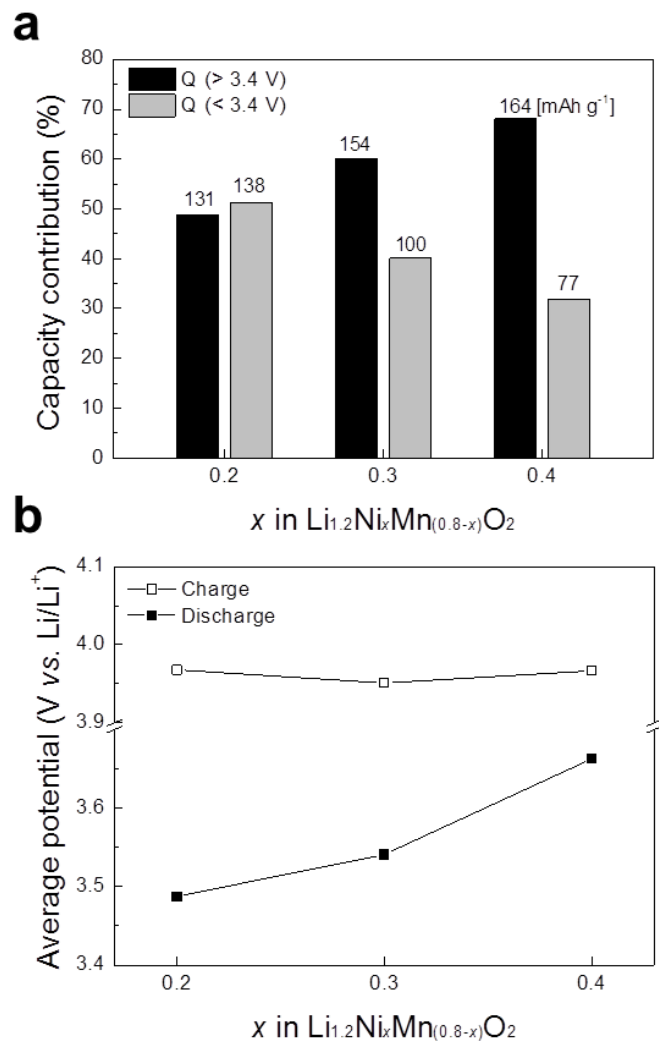


Figure 2.24. a) Capacity contributions on discharge above 3.4 V (black) and below 3.4 V (grey), and b) average potential (energy/capacity) of charge and discharge processes of the LLNMOs.

The overall structural evolution is first examined by XRD as shown in Figure 2.25 and 2.26a. The most obvious difference observed in XRD patterns of LLNMOs after cycling was the ratio among several important Bragg peaks that indicate the degree of transition metal ordering. In XRD patterns of LL226 after cycling, the intensity ratio of (104)/(003) peak becomes notably larger compared to that of LL235 and LL244 in Figure 2.25. For clear comparison, we plotted the ratio of the (104) peaks at 44.1° to the (101) peaks at 36.5° and the (003) peaks at 18.5° for LLNMOs at pristine states and after electrochemical cycling (Figure 2.26a). At pristine states, the ratios of the (104) peak to the (101) peak and the (104) peaks to the (003) peaks are almost identical for the three compounds in the range of 2.455 – 2.480 and 0.545 – 0.565, respectively. However, after five cycles, the peak intensities dramatically changed which results in the differences between the ratios for LLNMOs along compositions. For LL226 with the low-nickel contents, both ratios of the (104) peak to the (101) peaks and the (003) peaks increased to 2.63 and 0.71, respectively, while the values significantly decreased to 2.08 and 0.27 for LL244 with the high-nickel contents. The increase of the ratio values of LL226 is attributable to our simulations on XRD patterns (Figure 2.26b) which qualitatively analyze that the (104) peak grows while the (003) peak and the (101) peak diminish as some portions (~6%) of the transition metal ions migrate into the lithium layer, reducing the contrast between transition metal layers and lithium layers.

In contrast, the decrease of the ratio values of LL244 indicates the

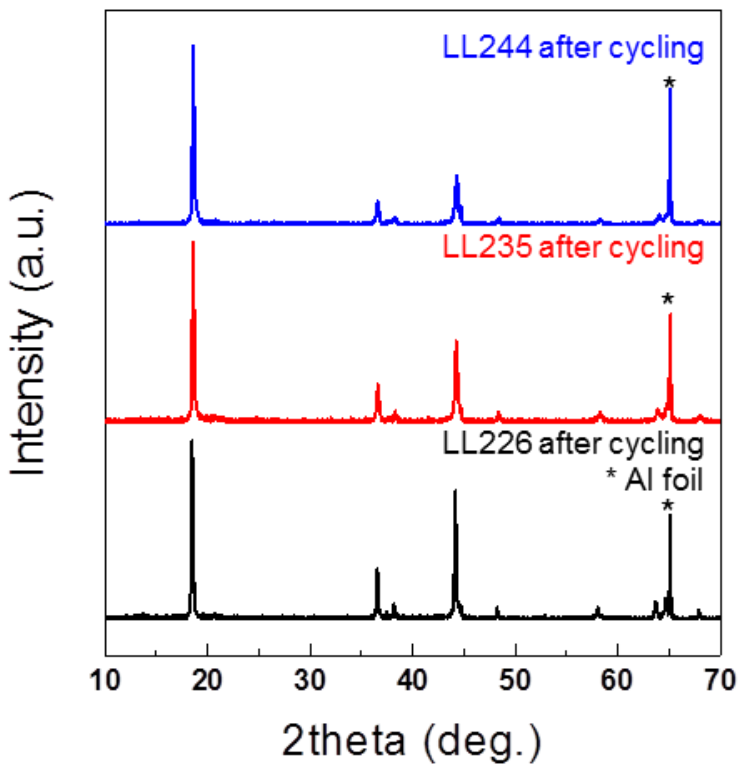


Figure 2.25. XRD patterns of LL226 (black), LL235 (red), and LL244 (blue) after five electrochemical cycles

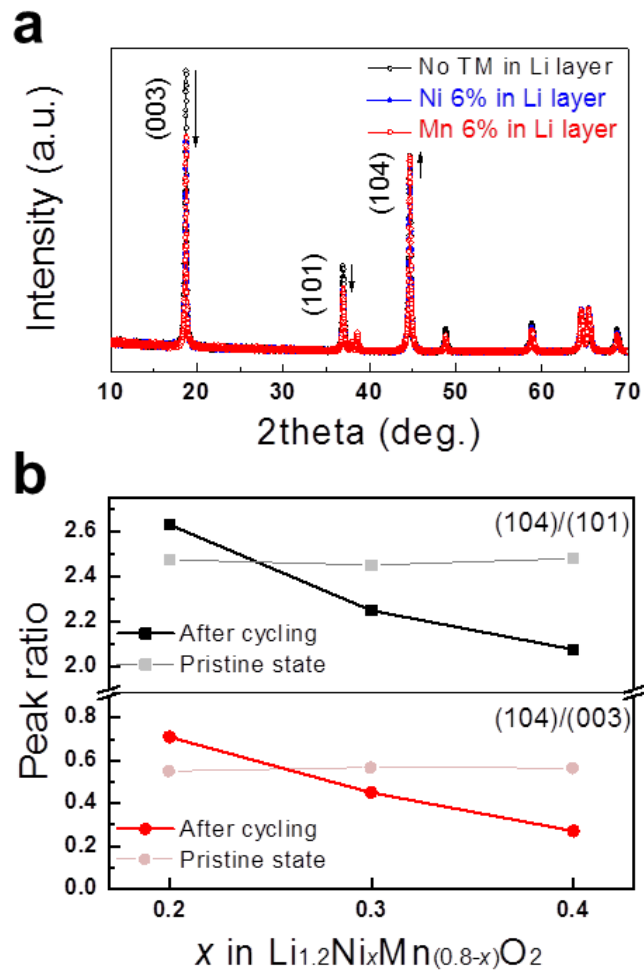


Figure 2.26. a) Peak ratio of (104)/(101) (black) and (104)/(003) (red) of LLNMOs before and after cycling, b) simulated XRD patterns of LLNMO with no transition metal ions in lithium layers (black), with 6 % nickel (blue) migration or manganese migration (red) into Li layers

increased contrast between transition metal layers and lithium layers which might originates from the lattice densification of transition metal layers. The previous NMR, XRD studies revealed the substitution of vacancies (original lithium site in transition metal layers) with migrated transition metal species.^{10,26} These results also well agree with the changes in lattice parameters measured by full pattern matching refinement as shown in Figure 2.27. Both lattice parameters a and c (based on $R\bar{3}m$ symmetry) increased after cycling for all compounds. The lattice expansion along both a and c axes is rather abnormal phenomena in the layered compounds. In a presence of vacancies in lithium layers which can be resulted from the incomplete re-intercalation during cycling, lattice parameter a typically decreases due to the reduced size of the oxidized transition metal ions, while lattice parameter c increases due to the electrostatic repulsion across the Van der Waals gap between the transition metal layers. Instead, the results demonstrate the transition metal migration into lithium layers.^{6,11} It is notable that the lattice expansion along a and c axes was most significant in LL226 (a : 0.94%, c : 1.12%) which is 70% larger expansion than that in LL244.

We further probed the changes in atomic arrangements by Raman spectroscopy, which has been demonstrated to be particularly sensitive to changes in metal-oxygen bonds in layered and spinel structures.^{11,27-29} Figure 2.28 compares the Raman spectra of LL226, LL235, and LL244 before and after electrochemical cycles. Initially, three samples exhibit generally similar patterns characteristic of layered materials. Two peaks near 595 and 474 cm⁻¹

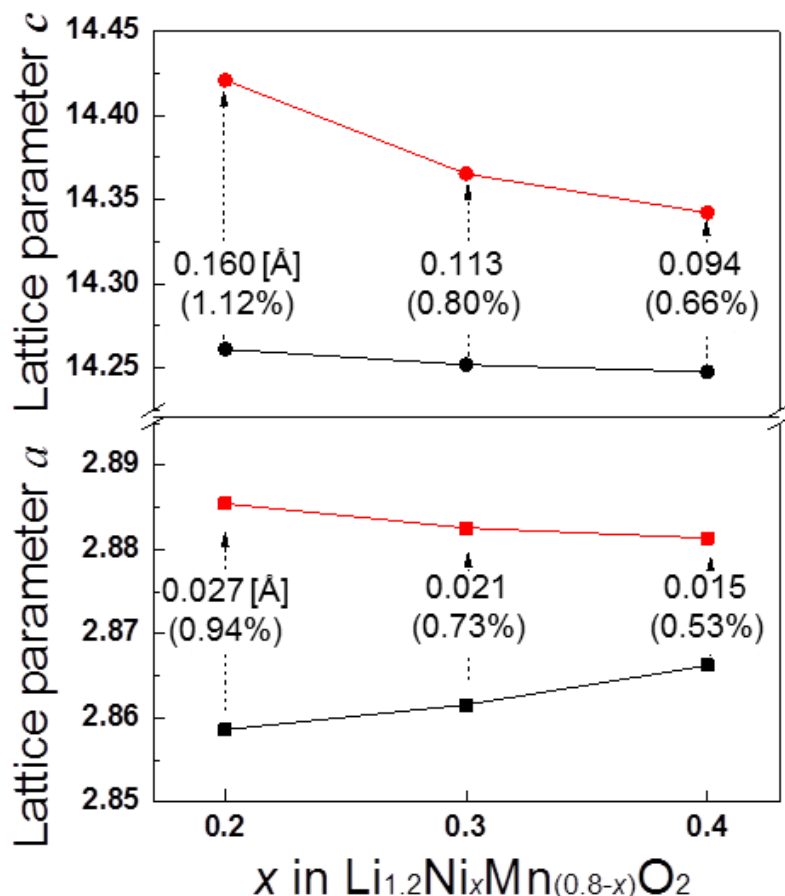


Figure 2.27. Lattice parameters of LLNMOs before (black) and after (red) cycling obtained by Rietveld refinements.

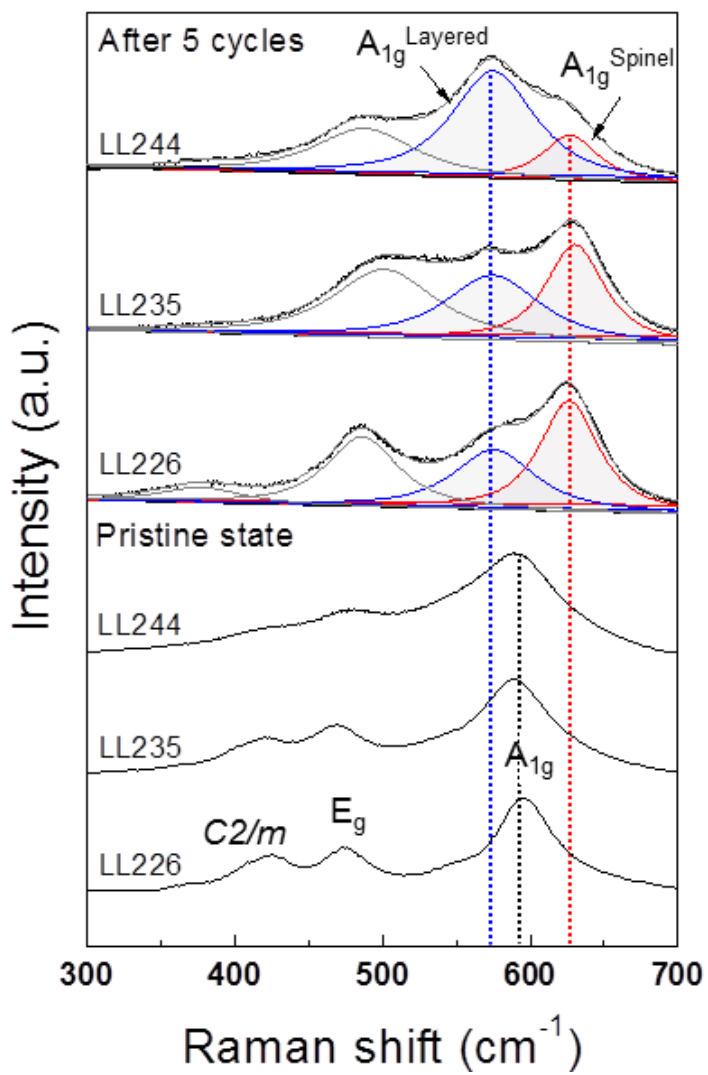


Figure 2.28. Raman spectra of LLNMOs before (bottom) and after five cycles (top). Red peak and blue peak indicate A_{1g} mode of spinel and layered phases, respectively.

corresponds to the A_{1g} (symmetrical stretching of M–O) and E_g (symmetrical deformation) vibrational modes in layered lithium transition metal oxides with $R\bar{3}m$ symmetry. An additional small peak at 425 cm^{-1} originates from the Li_2MnO_3 -like structure with the lower $C2/m$ symmetry. The intensity of the peak at 425 cm^{-1} increases with the Mn content in the samples implying the higher degree of ordering which is consistent with the observation on the superstructure patterns in the XRD (Figure 2.18). The single A_{1g} mode for the pristine compounds indicates that the layered LiMO_2 and Li_2MnO_3 phases share a common layered lattice framework. However, after electrochemical cycles, it was noted that the initial spectra are significantly altered. For all samples, the symmetrical M–O stretching peak split into two peaks near 627 and 572 cm^{-1} indicating the evolution of two different bonding environments. The peak near 627 cm^{-1} is commonly attributed to the M–O symmetrical stretching in spinel $\text{Li}_{1+x}\text{M}_2\text{O}_4$, which was also confirmed from the spectra of $\text{Li}_{1+x}\text{Mn}_2\text{O}_4$ (Figure 2.29).³⁰ The peak at 572 cm^{-1} can be assigned as the layered A_{1g} peak which is lower frequency compared to the pristine compounds (595 cm^{-1}). The shift to lower frequency of the layered A_{1g} peak after cycling is attributable to the increase in the average mass of the atoms in the transition metal layers which might be induced from the lattice densification. The densification is also consistent with the disappearance of the peak at 425 cm^{-1} corresponding to the honeycomb-like ordering in the transition metal layers in our Raman study as well as the XRD results (Figure 2.25).

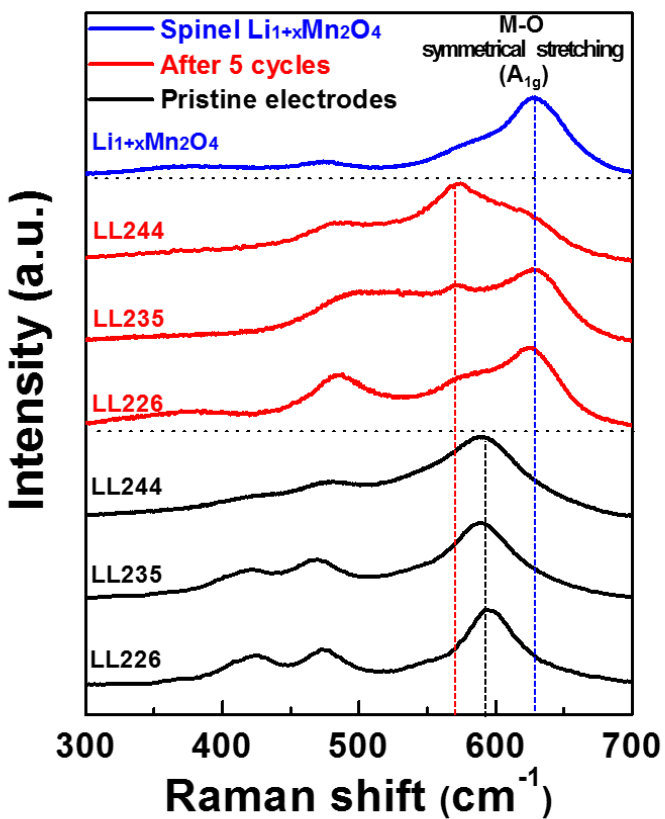


Figure 2.29. Raman spectra of LLNMOs before (black) and after five cycles (red) compared with spinel $\text{Li}_{1+x}\text{Mn}_2\text{O}_4$ (blue). Red dotted line and blue dotted line indicate A_{1g} mode of layered and spinel phases, respectively.

The peak separation indicates the division of the original layered structure into two different phases with spinel and layered structures in agreement with previous studies on LL226.^{11,12} Notable is that the ratio between the A_{1g} peaks of the spinel and layered phases depended on the composition of the LLNMO compounds. As shown in Figure 2.28, the majority of the structure remains as a layered structure in LL244, contrast to the high-manganese-content LL226 where significantly more spinel phase was detected after cycles. The calculated portions of the spinel A_{1g} peak area to the total area of the peak were 22%, 48% and 57% for LL244, LL235 and LL226, respectively. It follows similar trends for the fraction of discharge capacities accounted for the region below 3.4 V (32%, 40%, and 52%). It strongly suggests the correlation between the redox reactions activated below 3.4 V and the formation of the spinel phase (Li₂M₂O₄) in the framework.

To investigate the local structural change of the samples, transmission electron microscopy (TEM) analyses were performed. The alternative stacking of transition metal layers (aligned bright spots) and lithium layers (dark space) was observed in the high-resolution (HR) images of LL226 at pristine state along [100] crystallographic direction of rhombohedral $R\bar{3}m$ structure ([100]_R) which is parallel to [0-10] of monoclinic $C2/m$ ([0-10]_M) (Figure 2.30a). The transition metal layers are stacked in a sequence of A-C-B-A-C-B (inset, top) indicative of O₃-structure. The arrows in the figure correspond to the *c* axis of $R\bar{3}m$ and $C2/m$ structures (inset, bottom). The selected area electron diffraction (SAED) pattern obtained from the particle

in Figure 2.30a is shown in Figure 2.30b which corresponds to a typical SAED pattern of the layered compounds, *i.e.*, LiMO₂ and Li₂MO₃ along the [100]_R and the [0-10]_M direction, respectively.³¹

Along the [-441]_R direction which is parallel to the [10-1]_M direction, the atoms (bright spots) are aligned in square patterns in the HR-TEM images of as-prepared LL226 (Figure 2.31a) and LL244 (Figure 2.31c) obtained. In the SAED patterns of the as-prepared compounds, the diffraction spots from both $R\bar{3}m$ and $C2/m$ structures were observed (Figure 2.31b and 2.31d). The bright spots composing pink-colored squares correspond to the {110}_R planes and the {104}_R planes of $R\bar{3}m$ structure which can also be indexed as the {060}_M planes and the {131}_M planes of $C2/m$ structure. Two darker spots linearly located on the diagonals of the squares correspond to the {020}_M and {040}_M planes or the {111}_M planes of the monoclinic Li₂MO₃ phase with lower symmetry which agrees with the superstructure peaks in the XRD results.

To trace the structural evolution, we compared the HR-TEM images and SAED patterns of the compounds along the [-441]_R//[10-1]_M direction, which allows us to distinguish the spinel phase formed during electrochemical cycling from the original layered phases.

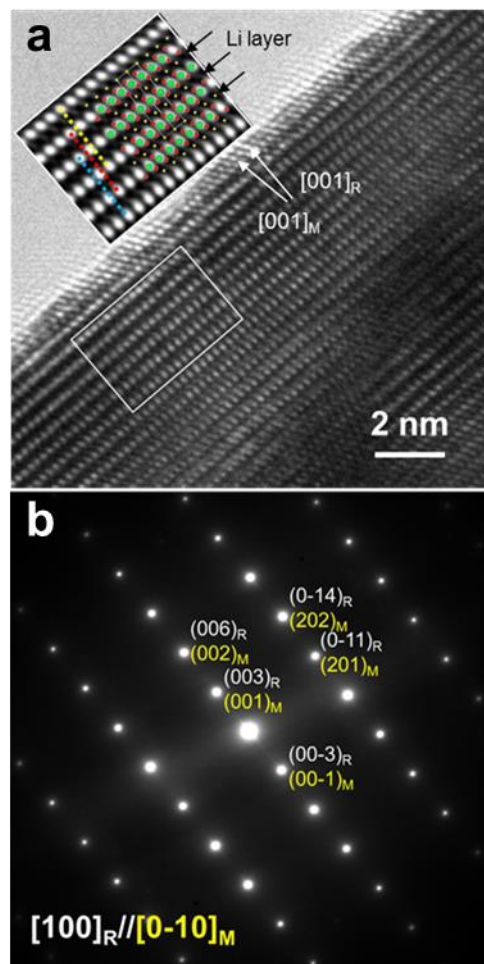


Figure 2.30. a) HR-TEM images and b) corresponding SAED patterns (bottom) of as-prepared LL226 along $[100]_R$ direction which is parallel to $[0-10]_M$ direction of monoclinic $C2/m$.

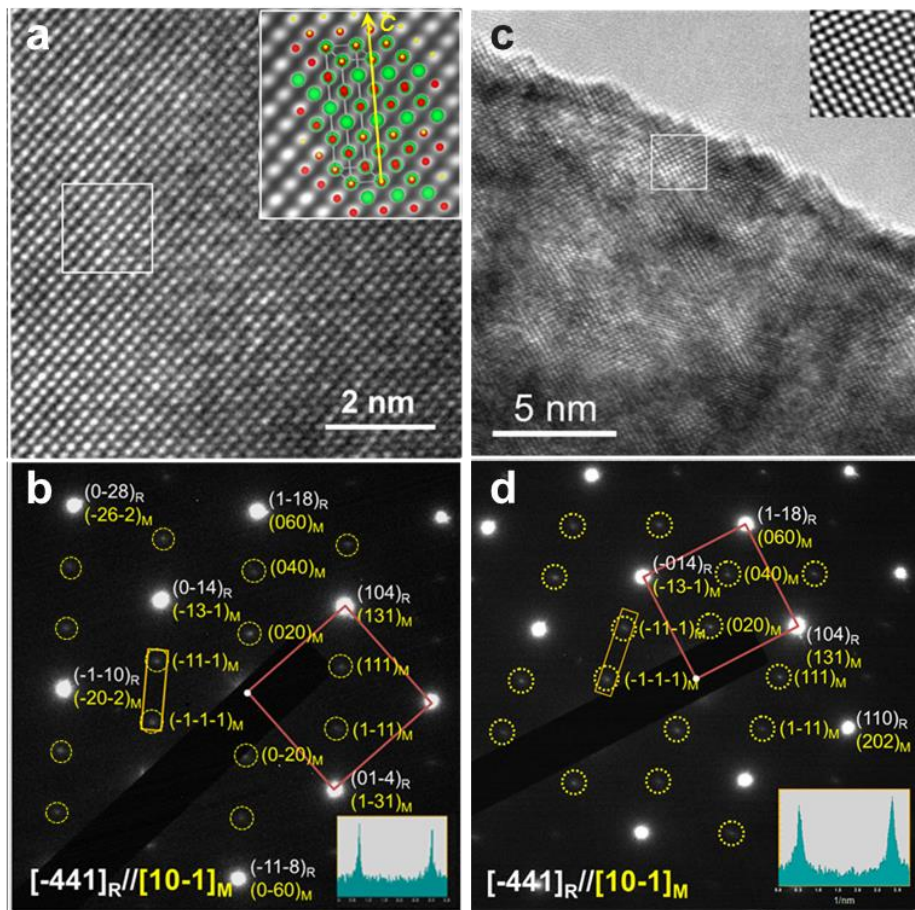


Figure 2.31. HR-TEM images and corresponding SAED patterns of a, b) LL226 along $[-441]_R$ direction which is parallel to $[10-1]_M$ direction of $C2/m$, and c, d) as-prepared LL244 along $[-441]_R$ direction. Insets in HR-TEM images show the inverse FFT images of white boxed region and corresponding atomic structure of the materials. Insets in SAED patterns show the intensity histogram of the yellow-boxed region.

As the result, we could find an alteration in the SAED patterns of LL226 after electrochemical cycling shown in Figure 2.32a. In the SAED pattern of LL226, additional diffraction spots appeared in the center of the $\{020\}_M$ and $\{040\}_M$ spots, or in between the origin and $\{110\}_R$ spots. The additional spots can be indexed as $\{220\}$ planes of the cubic spinel phase ($\{220\}_C$) which is parallel to the $\{110\}_R$ and the $\{060\}_M$ planes. As shown in the Figure 2.33, the difference between the $\{220\}_C$ plane and the parallel planes of layered phase is the presence of the transition metals in the lithium layers, indicative of the formation of spinel-like phases in LL226 after cycling *via* the interlayer migration of the transition metal ions. Note that the $\{220\}_C$ spots were observed in all the regions of the sample (Figure 2.32b-d), which implies that the layered-to-spinel structural evolution occurred throughout the particles but not limited to the near-surface region. In contrast, we could find negligible signatures from the $\{220\}_C$ planes in the SAED patterns of LL244 after the cycling (Figure 2.34a, b) which suggests that majority of the LL244 is remained as layered structure in agreement with the Raman results.

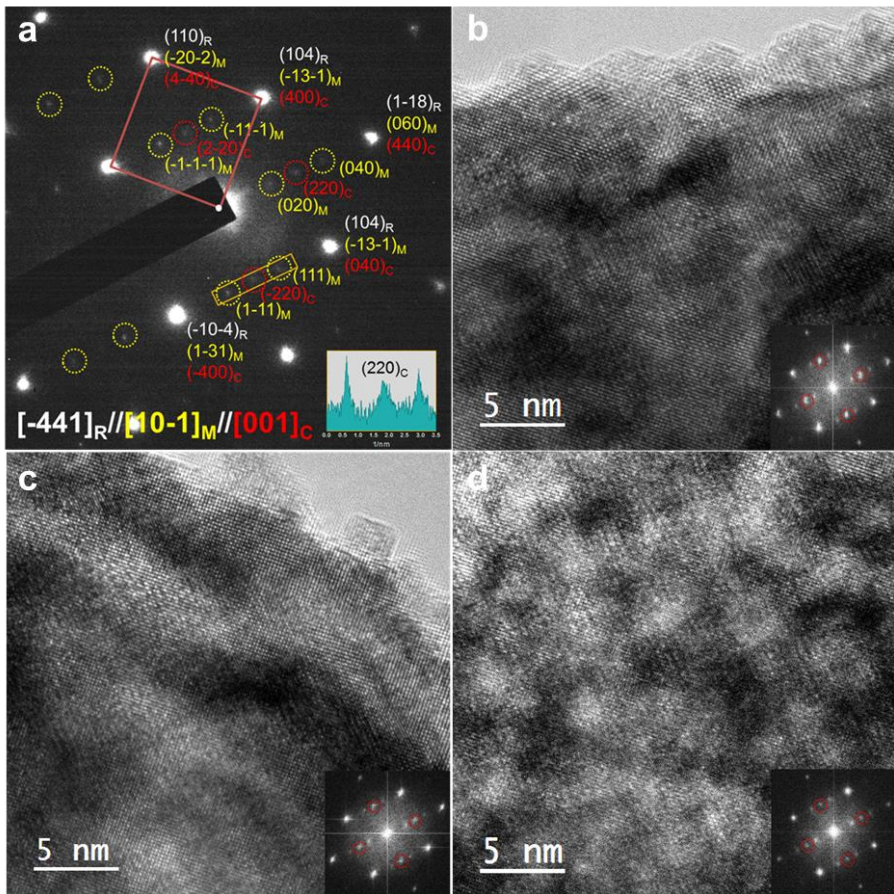


Figure 2.32. a) SAED pattern of LL226 after five cycles along $[-441]_R$ direction which is parallel to $[10-1]_M$ of monoclinic $C2/m$ and $[001]_C$ of cubic $Fd\text{-}3m$ (spinel phase). b-d) HR-TEM images and corresponding FFT patterns (inset) of local regions of the particle. Insets in SAED patterns show the intensity histogram of the yellow-boxed region.

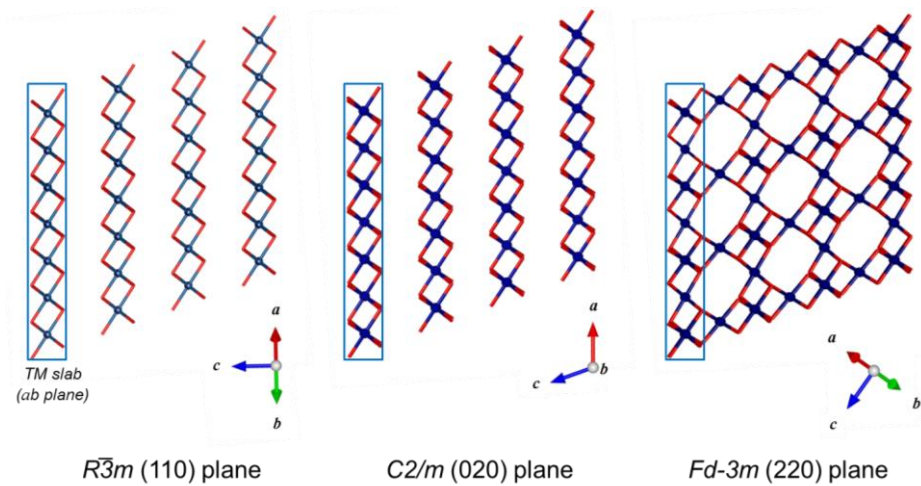


Figure 2.33. Structural differences between the layered $(110)_R//(020)_M$ planes and spinel $(220)_c$ plane. The formation of spinel-like phases in LLNMO after cycling takes place by the interlayer migration of the transition metal ions between the transition metal slabs.

To improve our understanding on the redox mechanism during the cycling, *ex situ* X-ray absorption spectroscopy (XAS) study was performed. Figure 2.35 and 2.36 show XANES of the Mn K-edge and Ni K-edge for the samples at various states of charge. Mn K-edge spectra in Figure 2.35a indicate that the oxidation states of manganese remains almost identical for all the compounds at the charged states as +4, like the pristine states (Figure 2.21). However, changes in the shape of the spectra were observed for each compound with charging compared to the pristine compounds, which is from delithiation.⁶ After discharge of the samples, Mn⁴⁺ ions are reduced to a lower oxidation state (Mn³⁺) as shown in Figure 2.35b. Interestingly, it was noted that the degree of manganese reduction varies among samples. More manganese reduction were found for Mn-rich compounds such as LL226 than LL244 or LL235 (Figure 2.36). This result is consistent with the additional experiments of XPS, which revealed that the manganese reduction occurred more extensively in LL226 than in LL244 after electrochemical cycling (Figure 2.37a and b). Moreover, it coincides with the increasing electrochemical activities below 3.4 V, which is more dominant in Mn-rich samples. On the other hand, the opposite trend was found for XANES spectra of the Ni K-edge during cycling. The pristine materials contain different initial nickel oxidation states of +2, +2.67 and +3 for LL226, LL235, and LL244, respectively (Figure 2.21). Upon charging to 4.8 V, all the Ni K-edge converge into the same energy region of Ni⁴⁺ (Figure 2.38a).

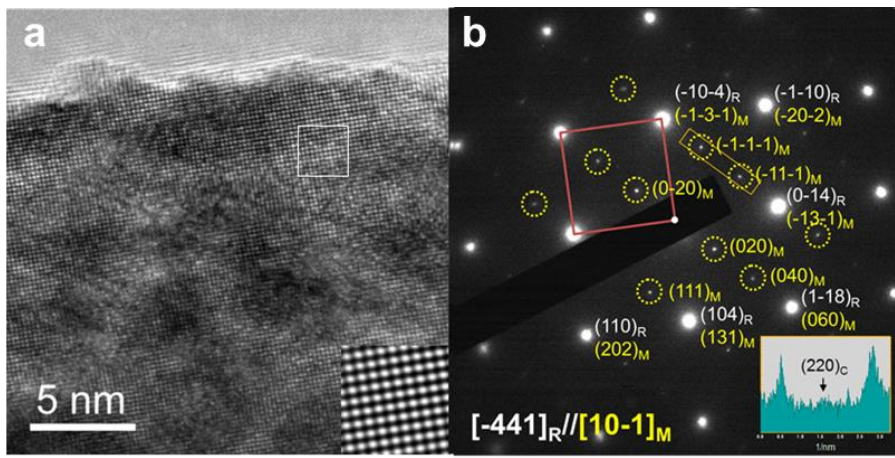


Figure 2.34. a) SAED pattern and b) HR-TEM image and corresponding FFT patterns (inset) of LL244 after five cycles along $[-441]_R$ direction. Insets in SAED patterns show the intensity histogram of the yellow-boxed region.

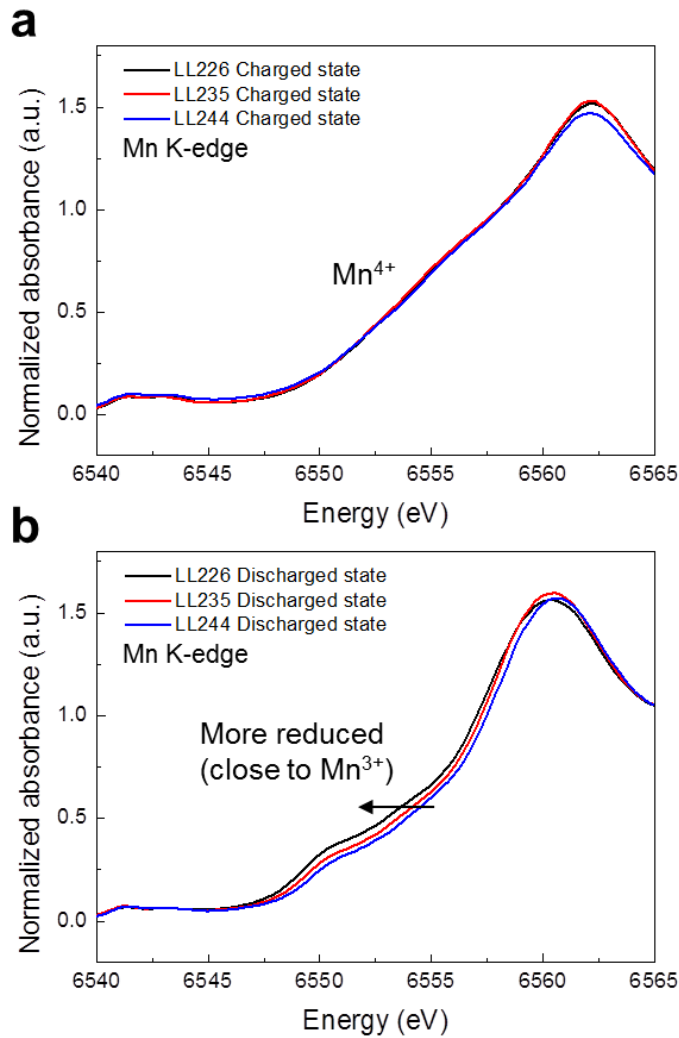


Figure 2.35. Mn K-edge XANES spectra of LL226 (black), LL235 (red), and LL244 (blue) at a) charged state (4.8 V) and b) discharged state (2.0 V).

However, unlike the manganese redox reaction, all the samples identically reduce to Ni^{2+} with following discharge (Figure 2.38b) which implies that attributed to slight changes in the electronic structure near manganese ions the redox reaction of nickel ions in both LL235 and LL244 has extended from $\text{Ni}^{2.67+}/\text{Ni}^{4+}$ or $\text{Ni}^{3+}/\text{Ni}^{4+}$ to $\text{Ni}^{2+}/\text{Ni}^{4+}$ after the first cycle (Figure 2.39). The XPS results also confirmed the lowered oxidation states (Ni^{2+}) of LL244 after cycling (Figure 2.40). The activation of the nickel divalent/tetravalent redox reaction in high-nickel-contents LL235 and LL244 after the first cycle accounts for the high electrochemical activities at 3.7 V of the samples. We believe that the extended nickel redox reaction is activated due to the higher redox potential of $\text{Ni}^{2+}/\text{Ni}^{3+}$ compared to that of $\text{Mn}^{3+}/\text{Mn}^{4+}$, which makes the lithiation process to reduce Ni^{3+} to Ni^{2+} before reducing Mn^{4+} to Mn^{3+} . The enhanced electrochemical activity at 3.7 V due to Ni redox reaction also implies that the local environment of Ni is likely to be in the layered-framework rather than spinel since the $\text{Ni}^{2+}/\text{Ni}^{4+}$ redox reaction in spinel framework takes place at much higher potential of 4.6–4.7 V in $\text{LiNi}_x\text{Mn}_{2-x}\text{O}_4$ ($0 < x < 0.5$).²⁸

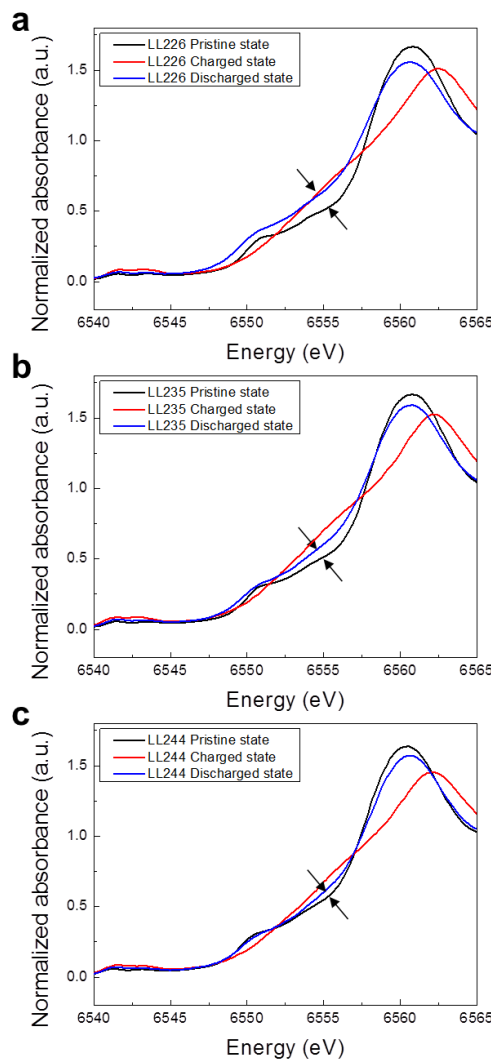


Figure 2.36. Mn K-edge XANES spectra of a) LL226, b) LL235, and c) LL244 electrodes at pristine (black), charged to 4.8 V (red), and discharged to 2.0 V (blue). Manganese trivalent/tetravalent redox reaction in LL226 is electrochemically more active compared to LL244.

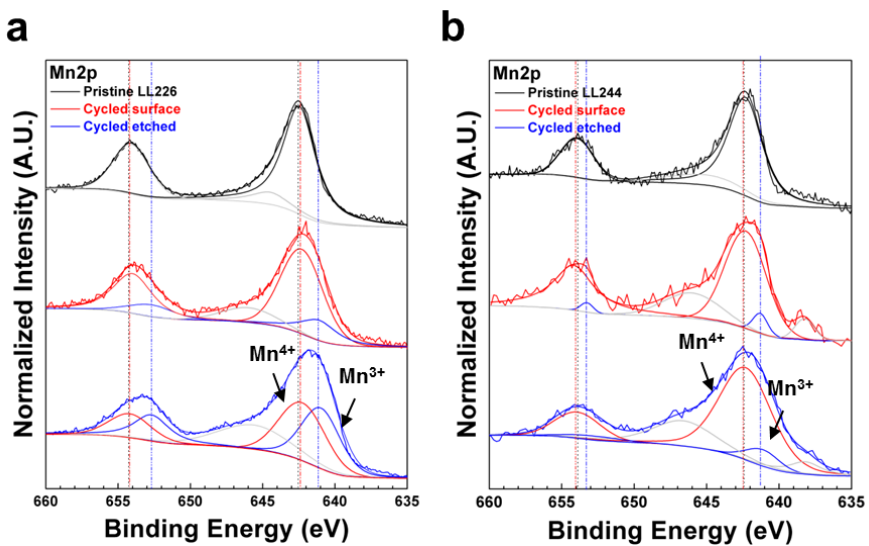


Figure 2.37. XPS Mn 2p spectra of a) LL226, b) LL244. Black, red, blue spectra (from top to bottom) represent the observed spectra of pristine LLNMO, surface of cycled LLNMO, and etched plane (surface + bulk properties) of LLNMO electrodes, respectively. Mn 2p spectra of etched planes show the presence of manganese ions reduced to trivalent state after cycling. The activation of manganese dominantly occurred in LL226 rather than LL244.

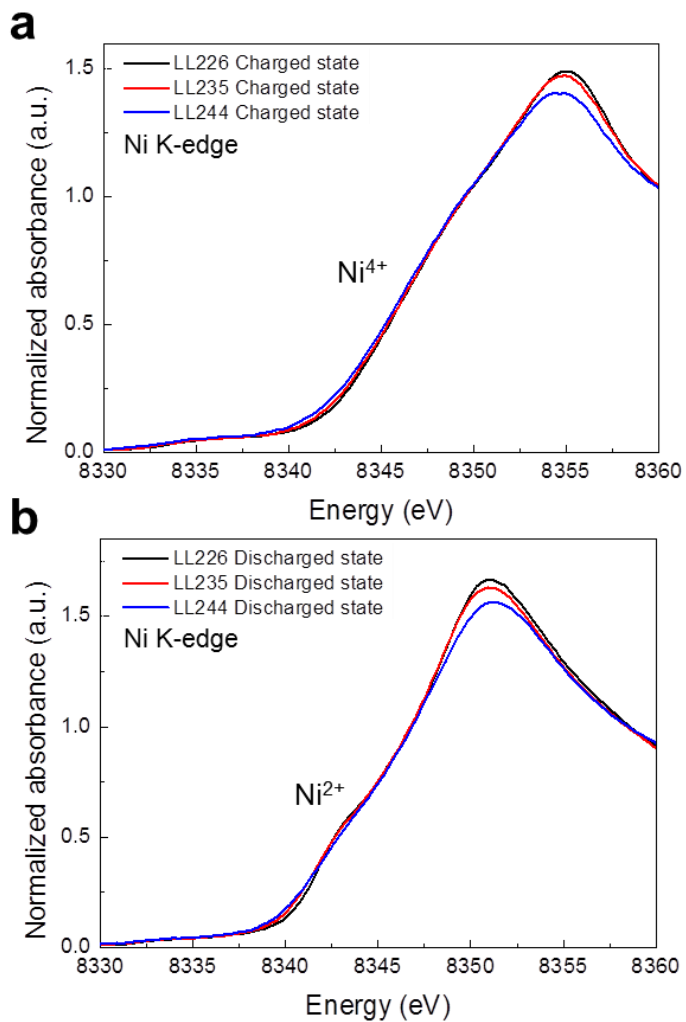


Figure 2.38. Ni K-edge XANES spectra of LL226, LL235, LL244 at a) charged state and b) discharged state.

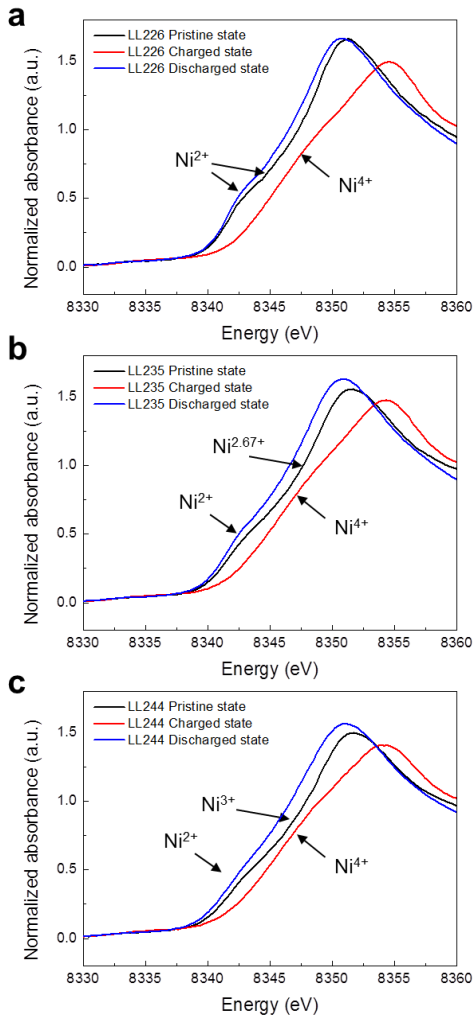


Figure 2.39. Ni K-edge XANES spectra of a) LL226, b) LL235, and c) LL244 electrodes at pristine (black), charged to 4.8 V (red), and discharged to 2.0 V (blue). Nickel divalent/tetravalent redox reactions occur in all compounds regardless of initial oxidation states of nickel ions.

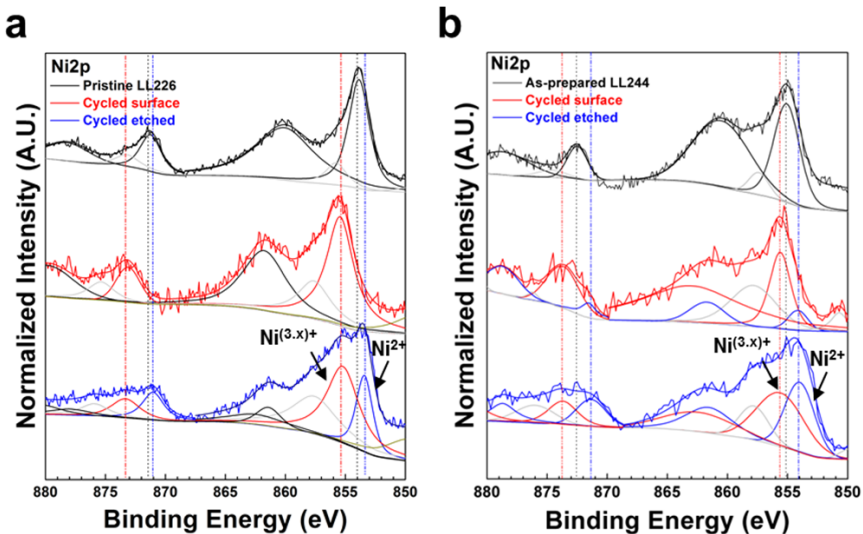


Figure 2.40. XPS Ni 2p spectra of a) LL226, b) LL244. Black, red, blue spectra represent the observed spectra of pristine LLNMO, surface of cycled LLNMO, and etched plane (surface + bulk properties) of LLNMO electrodes, respectively. Ni 2p spectra of etched planes confirm the activation of nickel redox reaction between divalent and tetravalent states after cycling in both LL226 and LL244. Spectra of the surface of cycled LLNMO and the etched plane of cycled LLNMO exhibit different characteristics due to the dissolution of trivalent manganese ions (See Figure 2.41). Nickel-rich regions at the surface of LLNMO contain large amount of nickel ions oxidized to $\text{Ni}^{3.x+}$, which is believed to be originated from the formation of LiNiO_2 or NiO_2 -like environments due to the manganese dissolution.

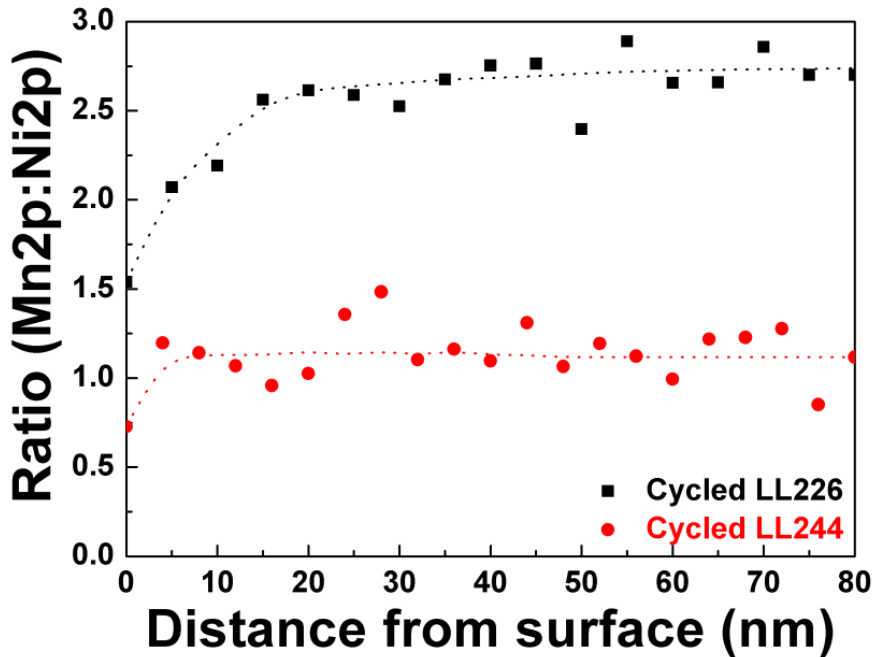


Figure 2.41. The ratio of manganese to nickel quantified with XPS spectra.

Severe manganese dissolution was observed at the surface of cycled electrodes. The detailed explanation of surface damage and manganese dissolution are well described in chapter 2.1.

We further examined the discharge reactions of the LLNMOs by using density-functional-theory (DFT)-based calculations. We designed a model system where some manganese ions have migrated into the lithium layers which results in a composite-like structure with a composition of $\text{LiNi}_{0.25}\text{Mn}_{0.75}\text{O}_2$ where the layered $\text{LiNi}_{0.5}\text{Mn}_{0.5}\text{O}_2$ and the spinel $\text{Li}_2\text{Mn}_2\text{O}_4$ are co-present with nanometer-sized domains (~ 0.8 nm) in a common oxygen framework (Figure 2.42). As the results of spin integration, we found that the manganese ions within spinel domains are trivalent while the manganese ions composing layered domains are tetravalent. The nickel ions are divalent. This result implies that the formation of spinel phase in LLNMOs induces the reduction of manganese ions into trivalent which results in the lower average oxidation states of manganese in LL226 compared to that in LL244.

According to our experimental and computational results, the key findings are (i) the final LLNMO structures contain two phases of layered and spinel structure, (ii) the electrochemical activities at 3.25 and 3.7 V were proportional to the amount of the spinel and layered phases, respectively, (iii) manganese trivalent/tetravalent redox reaction becomes activated especially for high Mn-contents LLNMO and (iv) the full nickel divalent/tetravalent redox reaction takes place regardless of initial nickel oxidation states. Based on the findings, we propose the structural evolution mechanism of LLNMOs as schematically illustrated in Figure 2.43 and

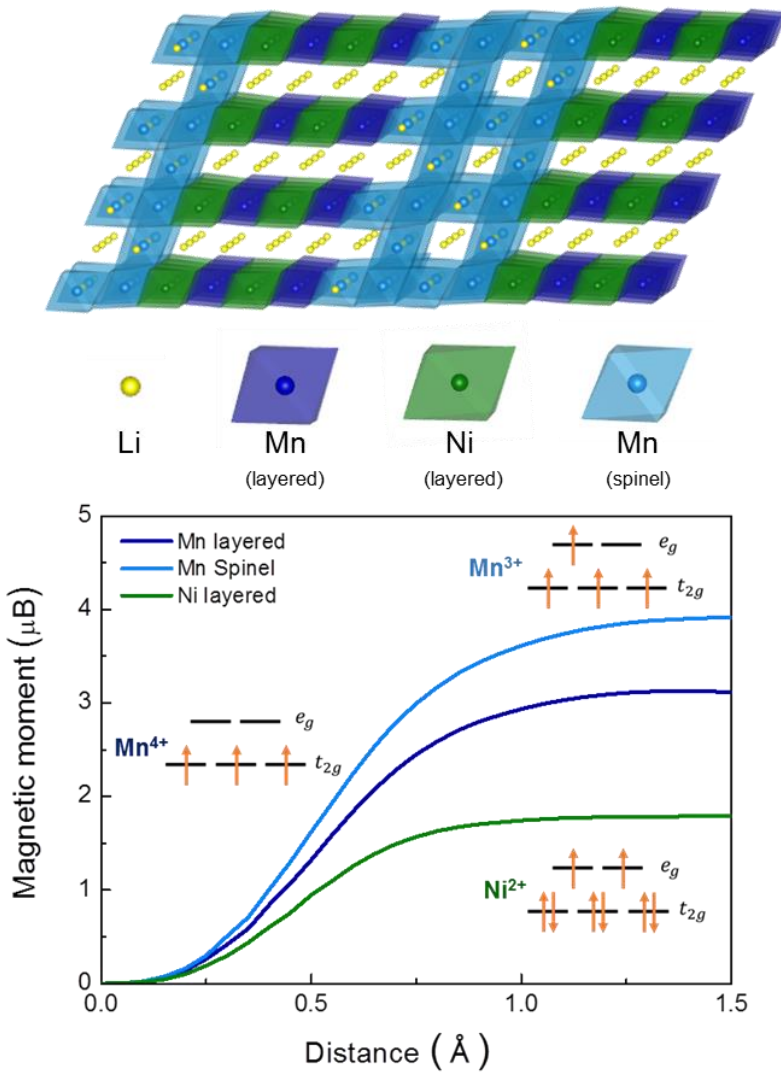


Figure 2.42. A model composite structure with nanometer-sized layered and spinel phases (top) and the oxidation states of the nickel and manganese composing the structure (bottom).

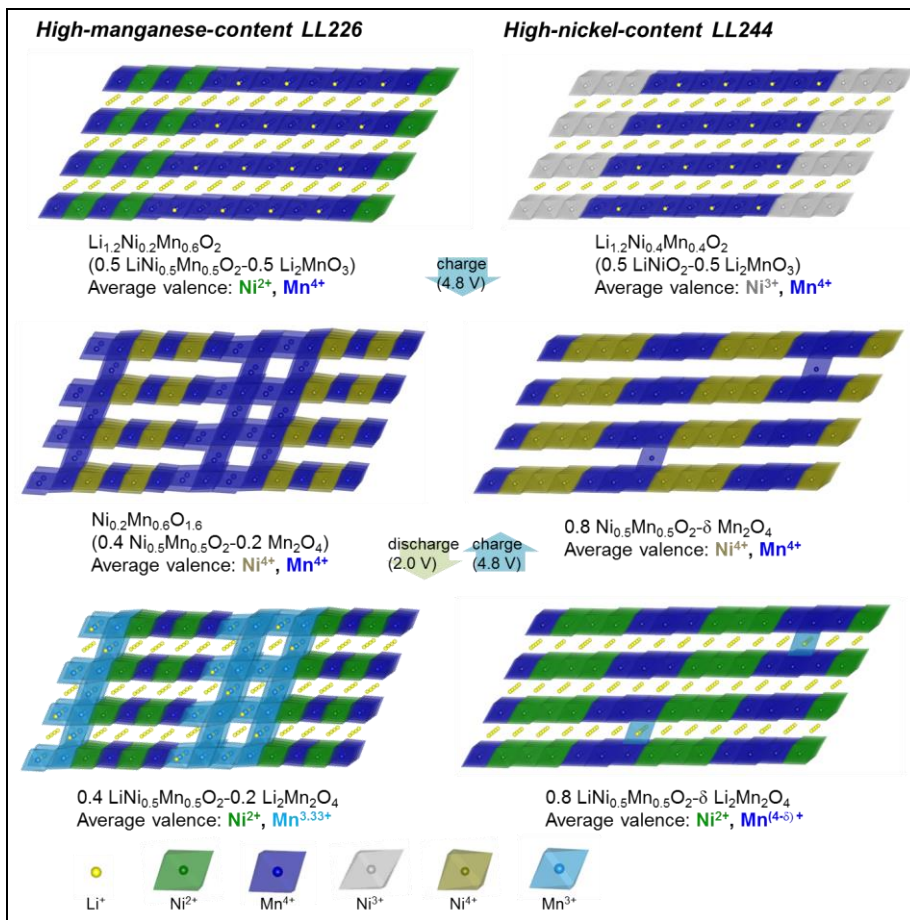
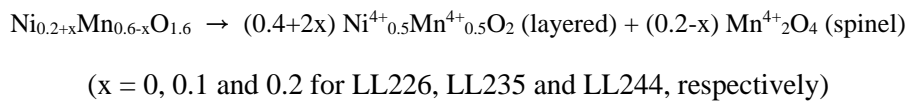


Figure 2.43. Proposed capacity activation and structural evolution mechanism of LLNMOs with high-manganese-content (left) and high-nickel-content (right).

summarized in Table 2.6. During the first charge, the initial delithiation (~4.4 V) occurs *via* the oxidation of Ni^{2+} (LL226), $\text{Ni}^{2.67+}$ (LL235) and Ni^{3+} (LL244) to Ni^{4+} accounting for 0.4 Li ion extraction from each phase. Remaining 0.8 Li ions are further extracted with a concurrent oxygen evolution, which results in $\text{Ni}_{0.2}\text{Mn}_{0.6}\text{O}_{1.6}$, $\text{Ni}_{0.3}\text{Mn}_{0.5}\text{O}_{1.6}$ and $\text{Ni}_{0.4}\text{Mn}_{0.4}\text{O}_{1.6}$. It should be noted that the valence states of both Ni and Mn in this state are +4. After the process above, the original phase converts into two domains of layered $\square\text{Ni}_{0.5}\text{Mn}_{0.5}\text{O}_2$ and spinel $\square\text{Mn}_2\text{O}_4$ as following.



Upon discharge, the re-lithiation into the layered phase of (0.4+2x) $\text{Ni}_{0.5}\text{Mn}_{0.5}\text{O}_2$ reduces Ni^{4+} to Ni^{2+} , while Mn^{4+} remains intact. On the other hand, Mn^{4+} reduces to Mn^{3+} in the spinel phase of (0.2-x) Mn_2O_4 when lithium is reinserted. Since each sample of LLNMO contains different ratio of Ni and Mn, therefore, different amounts of two phases in the transformed structure, the final valence states of Mn and Ni vary among samples. For example, when x = 0.1 (*i.e.* LL235), there are 0.3 Ni^{4+} and 0.5 Mn^{4+} in the charged state. The insertion of first 0.6 Li into this sample will reduce Ni^{4+} to Ni^{2+} before reducing Mn^{4+} to Mn^{3+} due to higher redox potential of $\text{Ni}^{2+}/\text{Ni}^{4+}$,²⁹ resulting in 0.5 $\text{LiNi}^{2+}_{0.5}\text{Mn}^{4+}_{0.5}\text{O}_2$ (layered) + 0.1 $\text{Mn}^{4+}_{2}\text{O}_4$ (spinel). Further lithiation of 0.2 Li occurs in the spinel phase by reducing

Mn^{4+} to Mn^{3+} , which completes the discharge process with 0.5 $LiNi^{2+}_{0.5}Mn^{4+}_{0.5}O_2$ (layered) + 0.1 $Li_2Mn^{3+}_2O_4$ (spinel). The final valence state of Mn, therefore, becomes +3.6 after the discharge. Likewise the Mn oxidation states become +3.33, +3.6 and +4 for LL226, LL235 and LL244 after discharge, respectively, while those of Ni are +2 for all samples. It corresponds to the XANES and XPS observation that the Ni oxidation states converge to the same value for all samples and the Mn oxidation states differ for samples. Our mechanism predicts the similar reversible capacities of LL226, LL235, and LL244. The theoretical capacities of LL226, LL235, and LL244 are almost the same about 251 mAh g⁻¹ corresponding to 0.8 Li⁺, which agrees well with the experimental results on LL226 (0.84 Li⁺), LL235 (0.81 Li⁺), and LL244 (0.77 Li⁺). The slightly lower capacity of LL244 compared to LL226 is believed to originate from the less mixed configuration of transition metal ions of $LiNi_{0.5}Mn_{0.5}O_2$ formed in LL244 during cycling because the $LiNi_{0.5}Mn_{0.5}O_2$ phase was built with the nickel ions and the manganese ions from $LiNiO_2$ phase and the Li_2MnO_3 phase, separately.

Table 2.6. Proposed mechanism of structural evolution and capacity activation in LL226, LL235, and LL244

	Pristine	Oxidized (4.4 V)	Fully charged	Cycled (2.0 V)** (4.8 V)*
Phase	$\text{Li}_{1.2}\text{Ni}_{0.2}\text{Mn}_{0.6}\text{O}$ 2 (LL226)	$\text{Li}_{0.8}\text{Ni}_{0.2}\text{Mn}_{0.6}\text{O}$ 2	$\text{Ni}_{0.2}\text{Mn}_{0.6}\text{O}_{1.6}$ 6	$\text{Li}_{0.8}\text{Ni}_{0.2}\text{Mn}_{0.6}\text{O}_{1.6}$ \rightarrow $0.4\text{LiNi}_{0.5}\text{Mn}_{0.5}\text{O}_2$ / $0.2\text{Li}_2\text{Mn}_2\text{O}_4$
Oxidation state	$\text{Ni}^{2+}, \text{Mn}^{4+}$	$\text{Ni}^{4+}, \text{Mn}^{4+}$	$\text{Ni}^{4+}, \text{Mn}^{4+}$	$\text{Ni}^{2+}, \text{Mn}^{4+}/ \text{Mn}^{3+}$ (average: $\text{Ni}^{2+}, \text{Mn}^{3.33+}$)
Phase	$\text{Li}_{1.2}\text{Ni}_{0.3}\text{Mn}_{0.5}\text{O}$ 2 (LL235)	$\text{Li}_{0.8}\text{Ni}_{0.3}\text{Mn}_{0.5}\text{O}$ 2	$\text{Ni}_{0.3}\text{Mn}_{0.5}\text{O}_{1.6}$ 6	$\text{Li}_{0.8}\text{Ni}_{0.3}\text{Mn}_{0.5}\text{O}_{1.6}$ \rightarrow $0.6\text{LiNi}_{0.5}\text{Mn}_{0.5}\text{O}_2$ / $0.1\text{Li}_2\text{Mn}_2\text{O}_4$
Oxidation state	$\text{Ni}^{2.67+}, \text{Mn}^{4+}$	$\text{Ni}^{4+}, \text{Mn}^{4+}$	$\text{Ni}^{4+}, \text{Mn}^{4+}$	$\text{Ni}^{2+}, \text{Mn}^{4+}/ \text{Mn}^{3+}$ (average: $\text{Ni}^{2+}, \text{Mn}^{3.6+}$)
Phase	$\text{Li}_{1.2}\text{Ni}_{0.4}\text{Mn}_{0.4}\text{O}$ 2 (LL244)	$\text{Li}_{0.8}\text{Ni}_{0.4}\text{Mn}_{0.4}\text{O}$ 2	$\text{Ni}_{0.4}\text{Mn}_{0.4}\text{O}_{1.6}$ 6	$\text{Li}_{0.8}\text{Ni}_{0.4}\text{Mn}_{0.4}\text{O}_{1.6}$ \rightarrow $0.8\text{LiNi}_{0.5}\text{Mn}_{0.5}\text{O}_2$ / $\delta\text{Li}_2\text{Mn}_2\text{O}_4$
Oxidation state	$\text{Ni}^{3+}, \text{Mn}^{4+}$	$\text{Ni}^{4+}, \text{Mn}^{4+}$	$\text{Ni}^{4+}, \text{Mn}^{4+}$	$\text{Ni}^{2+}, \text{Mn}^{4+}/ \text{Mn}^{3+}$ (average: $\text{Ni}^{2+}, \text{Mn}^{(4-\delta)+}$)

*Full delithiation was hypothesized for the initial charge ($0.8\text{Li}^+ + 0.4\text{O}^{2-}$ extraction)

**Theoretically available reversible capacity is same for LL226, LL235, and LL244

2.2.4. Conclusion

The origin and mechanism of capacity activation and voltage decay in layered Li-excess nickel manganese oxides were examined by systematic study on $0.5\text{Li}_2\text{MnO}_3\text{-}0.5\text{LiMO}_2$ ($\text{M} = \text{Ni}_{0.5}\text{Mn}_{0.5}$, $\text{Ni}_{0.75}\text{Mn}_{0.25}$, Ni) compounds with different Ni/Mn ratios. On the basis of our results, it is proposed that high capacity after the first cycle is derived from two distinct activation mechanisms of manganese redox reaction ($\text{Mn}^{3+}/\text{Mn}^{4+}$) and nickel redox reaction between divalent and tetravalent states ($\text{Ni}^{2+}/\text{Ni}^{4+}$) irrespective of the initial valence states. The activation of transition metal ions accompanies the structural evolution of LLNMO into layered $\text{LiNi}_{0.5}\text{Mn}_{0.5}\text{O}_2$ and spinel $\text{Li}_2\text{Mn}_2\text{O}_4$ phases where $\text{Ni}^{2+}/\text{Ni}^{4+}$ and $\text{Mn}^{3+}/\text{Mn}^{4+}$ redox reactions are active, respectively. The relative amounts of layered and spinel phases in the final structure of LLNMOs after the cycling were significantly varied with the relative amounts of nickel and manganese ions of LiMO_2 components in $0.5\text{Li}_2\text{MnO}_3\text{-}0.5\text{LiMO}_2$ compounds. As the Ni/Mn ratio in LLNMO increased from 0.33 (LL226) to 1 (LL244), the formation of spinel phase were significantly inhibited resulting in a dramatic increase in the average redox potential of LLNMOs. In conclusion, to suppress the voltage decay of the layered Li-excess transition metal oxides, it is important to inhibit the formation of spinel phase during cycling by optimizing the composition of transition metal ions in LLNMOs, or exploiting new-type transition metal ions which prefer layered structure rather than spinel structure.

2.2.5. References

- 1 Kang, K., Meng, Y. S., Bréger, J., Grey, C. P. & Ceder, G. Electrodes with high power and high capacity for rechargeable lithium batteries. *Science* **311**, 977-980 (2006).
- 2 Lu, Z., MacNeil, D. D. & Dahn, J. R. Layered Cathode Materials $\text{Li}[\text{Ni}_x\text{Li}_{(1/3-2x/3)}\text{Mn}_{(2/3-x/3)}]\text{O}_2$ for Lithium-Ion Batteries. *Electrochemical and Solid-State Letters* **4**, A191-A194, doi:10.1149/1.1407994 (2001).
- 3 Yoon, W.-S., Grey, C. P., Balasubramanian, M., Yang, X.-Q. & McBreen, J. In Situ X-ray Absorption Spectroscopic Study on $\text{LiNi}_{0.5}\text{Mn}_{0.5}\text{O}_2$ Cathode Material during Electrochemical Cycling. *Chemistry of Materials* **15**, 3161-3169, doi:10.1021/cm030220m (2003).
- 4 Bréger, J. et al. Effect of High Voltage on the Structure and Electrochemistry of $\text{LiNi}_{0.5}\text{Mn}_{0.5}\text{O}_2$: A Joint Experimental and Theoretical Study. *Chemistry of Materials* **18**, 4768-4781, doi:10.1021/cm060886r (2006).
- 5 Thackeray, M. M. et al. Li_2MnO_3 -stabilized LiMO_2 ($\text{M} = \text{Mn, Ni, Co}$) electrodes for lithium-ion batteries. *Journal of Materials Chemistry* **17**, 3112-3125 (2007).
- 6 Yabuuchi, N., Yoshii, K., Myung, S.-T., Nakai, I. & Komaba, S. Detailed Studies of a High-Capacity Electrode Material for Rechargeable Batteries, $\text{Li}_2\text{MnO}_3-\text{LiCo}_{1/3}\text{Ni}_{1/3}\text{Mn}_{1/3}\text{O}_2$. *Journal of the American Chemical Society* **133**, 4404-4419, doi:10.1021/ja108588y (2011).
- 7 Lu, Z. & Dahn, J. R. Understanding the Anomalous Capacity of $\text{Li}/\text{Li}[\text{Ni}_x\text{Li}_{(1/3-2x/3)}\text{Mn}_{(2/3-x/3)}]\text{O}_2$ Cells Using In Situ X-Ray Diffraction and Electrochemical Studies. *Journal of The*

Electrochemical Society **149**, A815-A822, doi:10.1149/1.1480014 (2002).

- 8 Armstrong, A. R. *et al.* Demonstrating Oxygen Loss and Associated Structural Reorganization in the Lithium Battery Cathode $\text{Li}[\text{Ni}_{0.2}\text{Li}_{0.2}\text{Mn}_{0.6}] \text{O}_2$. *Journal of the American Chemical Society* **128**, 8694-8698, doi:10.1021/ja062027+ (2006).
- 9 Kim, J.-S. *et al.* Electrochemical and Structural Properties of $x\text{Li}_2\text{M}^{\text{c}}\text{O}_3 \cdot (1-x)\text{LiMn}_{0.5}\text{Ni}_{0.5}\text{O}_2$ Electrodes for Lithium Batteries ($\text{M}^{\text{c}} = \text{Ti, Mn, Zr}; 0 \leq x \leq 0.3$). *Chemistry of Materials* **16**, 1996-2006, doi:10.1021/cm0306461 (2004).
- 10 Tran, N. *et al.* Mechanisms Associated with the “Plateau” Observed at High Voltage for the Overlithiated $\text{Li}_{1.12}(\text{Ni}_{0.425}\text{Mn}_{0.425}\text{Co}_{0.15})_{0.88}\text{O}_2$ System. *Chemistry of Materials* **20**, 4815-4825, doi:10.1021/cm070435m (2008).
- 11 Hong, J. *et al.* Structural evolution of layered $\text{Li}_{1.2}\text{Ni}_{0.2}\text{Mn}_{0.6}\text{O}_2$ upon electrochemical cycling in a Li rechargeable battery. *Journal of Materials Chemistry* **20**, 10179-10186 (2010).
- 12 Xu, B., Fell, C. R., Chi, M. & Meng, Y. S. Identifying surface structural changes in layered Li-excess nickel manganese oxides in high voltage lithium ion batteries: A joint experimental and theoretical study. *Energy & Environmental Science* **4**, 2223-2233 (2011).
- 13 Sathiya, M. *et al.* Reversible anionic redox chemistry in high-capacity layered-oxide electrodes. *Nat Mater* **12**, 827-835, doi:10.1038/Nmat3699 (2013).
- 14 Rodriguez-Carvajal, J. in *Satellite Meeting on Powder diffraction of the XV Congress of the IUCr*. (Toulouse, France).
- 15 Ravel, B. & Newville, M. ATHENA, ARTEMIS, HEPHAESTUS: data analysis for X-ray absorption spectroscopy using IFEFFIT. *Journal of synchrotron radiation* **12**, 537-541 (2005).

- 16 Perdew, J. P., Burke, K. & Ernzerhof, M. Generalized Gradient Approximation Made Simple. *Physical Review Letters* **77**, 3865-3868 (1996).
- 17 Kresse, G. & Joubert, D. From ultrasoft pseudopotentials to the projector augmented-wave method. *Physical Review B* **59**, 1758-1775 (1999).
- 18 Kresse, G. & Furthmüller, J. Efficiency of ab-initio total energy calculations for metals and semiconductors using a plane-wave basis set. *Computational Materials Science* **6**, 15-50, doi:10.1016/0927-0256(96)00008-0 (1996).
- 19 Anisimov, V. I., Zaanen, J. & Andersen, O. K. Band theory and Mott insulators: Hubbard U instead of Stoner I. *Physical Review B* **44**, 943-954 (1991).
- 20 Van der Ven, A. & Ceder, G. Ordering in $\text{Li}_x(\text{Ni}_{0.5}\text{Mn}_{0.5})\text{O}_2$ and its relation to charge capacity and electrochemical behavior in rechargeable lithium batteries. *Electrochemistry communications* **6**, 1045-1050 (2004).
- 21 Meng, Y. S. *et al.* Cation Ordering in Layered $\text{O}_3 \text{Li}[\text{Ni}_x\text{Li}_{1/3-2x/3}\text{Mn}_{2/3-x/3}]\text{O}_2$ ($0 \leq x \leq 1/2$) Compounds. *Chemistry of Materials* **17**, 2386-2394, doi:10.1021/cm047779m (2005).
- 22 Kobayashi, H., Tabuchi, M., Shikano, M., Kageyama, H. & Kanno, R. Structure, and magnetic and electrochemical properties of layered oxides, Li_2IrO_3 . *Journal of Materials Chemistry* **13**, 957-962, doi:10.1039/B207282c (2003).
- 23 Bréger, J. *et al.* High-resolution X-ray diffraction, DIFFaX, NMR and first principles study of disorder in the $\text{Li}_2\text{MnO}_3-\text{Li}[\text{Ni}_{1/2}\text{Mn}_{1/2}]\text{O}_2$ solid solution. *Journal of Solid State Chemistry* **178**, 2575-2585, doi:10.1016/j.jssc.2005.05.027 (2005).
- 24 Sears, V. F. Neutron scattering lengths and cross sections. *Neutron News* **3**, 26-37, doi:10.1080/10448639208218770 (1992).

- 25 Hong, J. *et al.* Critical Role of Oxygen Evolved from Layered Li-Excess Metal Oxides in Lithium Rechargeable Batteries. *Chemistry of Materials* **24**, 2692-2697, doi:10.1021/cm3005634 (2012).
- 26 Jiang, M., Key, B., Meng, Y. S. & Grey, C. P. Electrochemical and Structural Study of the Layered, “Li-Excess” Lithium-Ion Battery Electrode Material $\text{Li}[\text{Li}_{1/9}\text{Ni}_{1/3}\text{Mn}_{5/9}]\text{O}_2$. *Chemistry of Materials* **21**, 2733-2745, doi:10.1021/cm900279u (2009).
- 27 Hwang, S.-J. *et al.* Micro-Raman Spectroscopic Study on Layered Lithium Manganese Oxide and Its Delithiated/Relithiated Derivatives. *Electrochemical and Solid-State Letters* **4**, A213-A216, doi:10.1149/1.1413704 (2001).
- 28 Loridant, S., Abello, L., Siebert, E. & Lucaleau, G. Correlations between structural and electrical properties of BaCeO_3 studied by coupled in-situ Raman scattering and impedance spectroscopy. *Solid State Ionics* **78**, 249-258, doi:10.1016/0167-2738(95)00112-J (1995).
- 29 Hy, S., Felix, F., Rick, J., Su, W. N. & Hwang, B. J. Direct In situ Observation of Li_2O Evolution on Li-Rich High-Capacity Cathode Material, $\text{Li}[\text{Ni}_x\text{Li}_{(1-2x)/3}\text{Mn}_{(2-x)/3}]\text{O}_2$ ($0 \leq x \leq 0.5$). *Journal of the American Chemical Society* **136**, 999-1007, doi:10.1021/Ja410137s (2014).
- 30 Hwang, S.-J., Park, H.-S., Choy, J.-H. & Campet, G. Evolution of Local Structure around Manganese in Layered LiMnO_2 upon Chemical and Electrochemical Delithiation/Relithiation. *Chemistry of Materials* **12**, 1818-1826, doi:10.1021/cm9905491 (2000).
- 31 Yu, H. J. *et al.* Direct Atomic-Resolution Observation of Two Phases in the $\text{Li}_{1.2}\text{Mn}_{0.567}\text{Ni}_{0.166}\text{Co}_{0.067}\text{O}_2$ Cathode Material for Lithium-Ion Batteries. *Angew Chem Int Edit* **52**, 5969-5973, doi:10.1002/anie.201301236 (2013).

Chapter 3. Biologically inspired organic compounds

(The essence of this chapter has been published in Angewandte Chemie International Edition, and Nature Communications. Reprinted from [M. Lee et al. *Angew. Chem. Int. Ed.*, (2013) DOI: 10.1002/anie.201301850] and [J. Hong *et al. Nat. Commun.*, 5, 5335 (2014) DOI:10.1038/ncomms6335]. Because this paper has been distributed under a Creative Commons license (Attribution-Noncommercial 2.5), one may reuse the contents for the paper for non-commercial/educational purposes without obtaining additional permission from Wiley-VCH Verlag GmbH & Co. KGaA and Macmillan Publishers Ltd., providing that the author and the original source of publication are fully acknowledged.)

3.1 Energy storage in biologically inspired organic electrode materials, flavin

3.1.1. Research background

Organic materials represent an attractive alternative to transition metal oxide cathodes in conventional rechargeable batteries because of their light weight, structural flexibility, and chemical diversity.¹ In particular, organic molecules that mimic redox centers in biological energy transduction have gained a great deal of attention for their sustainability and universal availability in natural systems.^{2,3} For instance, carbonyl-based compounds are the most

well-known examples of bio-inspired redox centers, imitating quinone cofactors in nature such as plastoquinone and ubiquinone, which are involved in the electron transport chain of chloroplasts and mitochondria.^{4,5} Previous studies on these compounds have shown promising electrochemical properties with high energy densities.⁶⁻⁹ Recent efforts have enabled the carbonyl-based organic electrodes to have high power as well as stable cycling performance, hinting at a practical feasibility for a bio-inspired design of energy storage materials.¹⁰⁻¹³

As a wide range of ion-coupled electron transfer reactions exists in biological energy conversion, the characterization of these redox systems may provide novel methods of electrochemical energy storage with versatile functionalities. In living organisms, heterocyclic molecules containing a pteridine (1,3,5,8-tetraazanaphthalene) nucleus composed of fused pyrimidine and pyrazine rings are widely occurring redox centers.^{14,15} Among such molecules, flavin cofactors including flavin adenine dinucleotide (FAD) and flavin mononucleotide (FMN) are one of the most vital compounds that catalyze biotransformation and energy transfer reactions.¹⁶ During photosynthesis and cellular respiration, for example, flavin cofactors serve as a key redox center facilitating proton-coupled electron transfer reactions for energy transduction. During the reaction, redox cycling occurs at the diazabutadiene of the isoalloxazine moiety.^{17,18} Based on this electrochemical cellular metabolism, I have proposed that natural flavin cofactors can be applied to lithium-storing electrodes in

rechargeable batteries as shown in Figure 3.1.¹⁹ I have demonstrated that the biochemical proton-coupled electron transfer reactions could be replaced by the lithium-coupled electron transfer reactions in man-made electrochemical devices (Figure 3.2). Although flavin-based electrodes can reversibly facilitate lithium-coupled electron transfer in batteries, their inadequate performance in terms of energy density and cycle stability requires further optimization along with in-depth studies regarding the underlying energy storage mechanism in the battery systems.

In chapter 3, I present a molecular design strategy to obtain an optimal redox-active cofactor of the diazabutadiene redox cycle on the basis of the in-depth study of organic electrode materials using combined DFT (density-functional-theory) calculations with experiments. While the DFT calculations have been widely utilized in the in-depth study on the energy storage mechanisms of various inorganic electrode materials,^{20,21} we used the computational method to understand the redox activity of organic active materials. First, in this chapter (3.1), the energy storage mechanisms of flavin redox cofactors *i.e.*, riboflavin and lumiflavine molecules which were demonstrated as active materials in lithium rechargeable batteries by experiments^{19,22} are studied. According to the DFT calculations results, the flavin molecules reversible store and release two electrons and energy in their diazabutadiene redox motif successively.

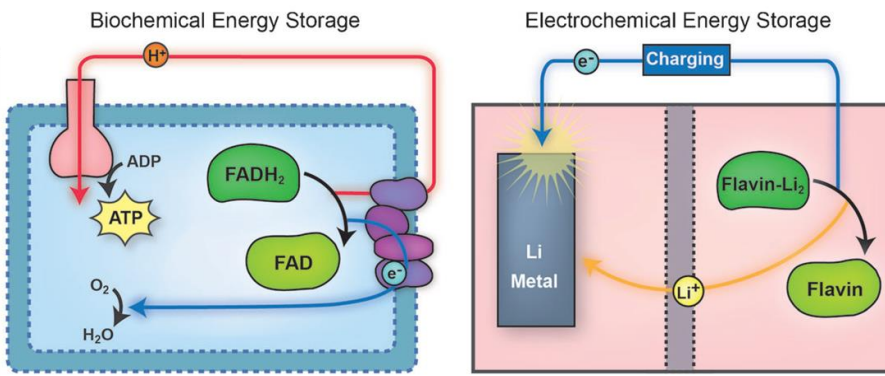


Figure 3.1. Biochemical energy transduction in mitochondria (left panel) where flavins work as a redox center to store energy from nutrients into high-energy ATP. For synthetic energy device applications (right panel), flavins serve as an active material that reversibly takes up and releases electrons and lithium ions during electrochemical energy storage.

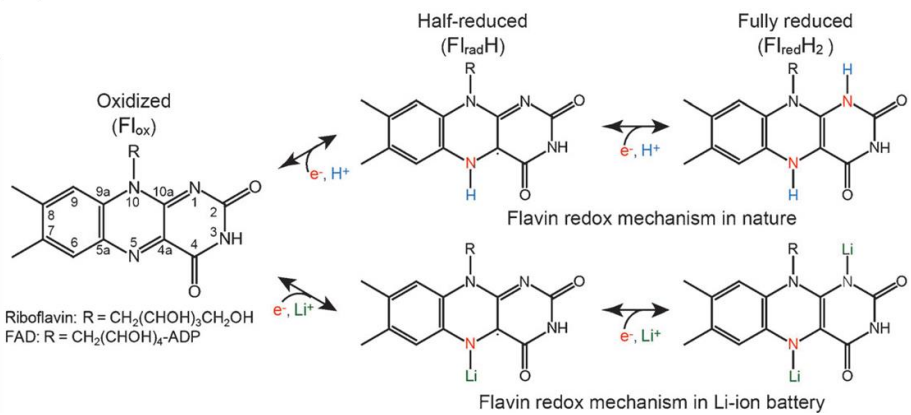


Figure 3.2. Different redox states of flavin-derivative molecules with indications of redox-active moieties upon electron uptake. Flavin molecules conduct a proton-coupled electron transfer reaction at N5 and N1 in nature (top). I suggest the flavin redox cycle can be applied to lithium rechargeable batteries using the reaction scheme proposed (bottom).

3.1.2. Computational details

Geometry optimization and energy calculations on the all molecules were conducted with spin-unrestricted density functional theory (DFT) using the Gaussian 09 quantum chemistry package²³ based on Becke-Lee-Yang-Parr (B3LYP) hybrid exchange-correlation functional^{24,25} and the standard TZVP basis set.²⁶⁻²⁸ The site and sequence of lithium occupation during redox reaction were determined by comparing DFT energies of possible reduced forms of molecules bonded to one or two lithium ions. Atomic charge was calculated with Mulliken population analysis.²⁹ Detailed procedure and the results of DFT calculations are discussed in the Supplementary Information. The HOMO plots were generated with cubegen utility which is embedded in Gaussian 09²³ and visualized with the Materials Studio program.

The sites and sequences of lithium occupation during electrochemical reactions in riboflavin were determined by comparing DFT energies obtained for the possible forms of Fl_{rad}Li (Flavin in radical form with one lithium ion insertion) and Fl_{red}Li₂ (Flavin in reduced form with two lithium ions insertion). First, a lithium atom was put on several binding sites of riboflavin; then the structure of lithiated riboflavin (Fl_{rad}Li) was fully optimized. Mulliken population analysis was used to investigate the redox reaction of riboflavin with lithiation. Mulliken charges of atoms in Fl_{ox}, Fl_{rad}Li, and Fl_{red}Li₂ of riboflavin were calculated. The similar calculations were conducted to understand the redox mechanism of lumiflavine which is the lighter form of molecule where the ribityl side group of riboflavin is

substituted by the methyl group.

3.1.3. Results and discussion

Figure 3.3 shows the DFT energies of the lithiated riboflavin radical ($\text{Fl}_{\text{rad}}\text{Li}$) with various configurations. We put lithium ions in various local environments forming N5-Li bond, N1-Li bond, pyrimidine (ring III)-Li bond and benzene (ring I)-Li bond. Among the various configurations, $\text{Fl}_{\text{rad}}\text{Li}$ with N5-Li1 bond was energetically the most stable at least by 576 meV. This value is significantly large considering the thermal energy at room temperature (about 25 meV) which implies that the results of DFT calculations are reasonable to accept. This result is consistent with the proton-coupled redox reaction of riboflavin in nature, where the first proton binds to N5.

I further investigated the site of the second lithium insertion by comparing various forms of the lithiated reduced flavins ($\text{Fl}_{\text{red}}\text{Li}_2$) with various lithium configurations as shown in Figure 3.4. After the first lithium insertion in N5, the second lithium was inserted into $\text{Fl}_{\text{rad}}\text{Li}$ to form additional N1-Li bond, benzene-Li bond, and pyrimidine-Li bond. Among various configurations of $\text{Fl}_{\text{red}}\text{Li}_2$, the $\text{Fl}_{\text{red}}\text{Li}_2$ with N5-Li1/N1-Li2 bond was energetically most stable compared to other $\text{Fl}_{\text{red}}\text{Li}_2$ with different lithium configurations by at least 1043 meV. Similar to the first lithium insertion, the second lithium insertion result is consistent with the proton-coupled redox reaction of riboflavin in nature, where the second proton binds to N1.

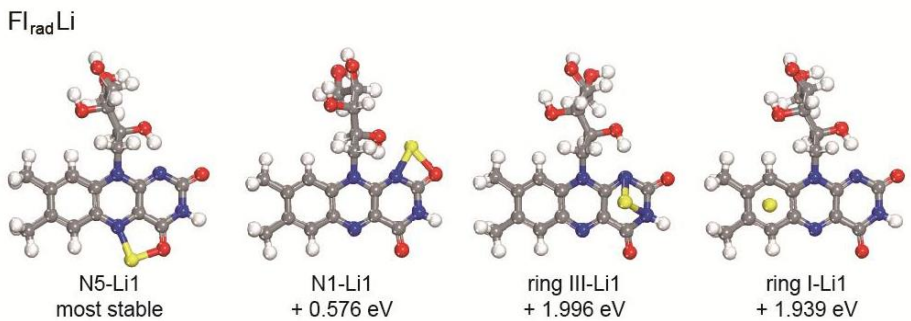


Figure 3.3. DFT energies calculated for various Fl_{rad}Li forms of riboflavin.

Fl_{rad}Li with N5-Li1 bond was energetically most stable compared to other Fl_{rad}Li with different lithium configurations.

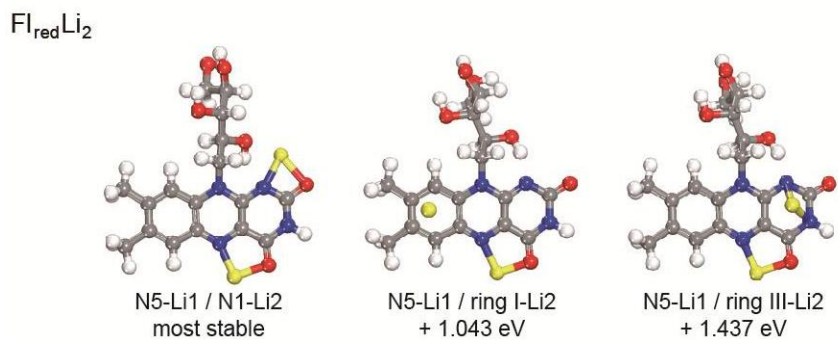


Figure 3.4. DFT energies calculated for various $\text{Fl}_{\text{red}}\text{Li}_2$ forms of riboflavin.

$\text{Fl}_{\text{red}}\text{Li}_2$ with N5-Li1/N1-Li2 bond was energetically most stable compared to other $\text{Fl}_{\text{red}}\text{Li}_2$ with different lithium configurations.

An interesting point is that while the formation of the new bonding occurs between lithium and nitrogen ions, the inserted lithium ions also interact with the neighboring oxygen atoms, which is totally different from the proton-coupled electron transfer reactions in nature. This phenomena is attributable to the relatively much large size of the lithium ion (59 pm) compared to the size of proton. As results, the insertion of lithium ions in riboflavin induces the formation of heterocyclic rings; during the first lithium insertion, the heterocyclic five-membered –C4a-C4-O4-Li1-N5-C4a- ring is formed and during the second lithium insertion, and the heterocyclic four-membered –C2-N1-Li2-O2-C2- ring is formed. As the geometric strain from four-membered heterocyclic ring is much large than that from five-membered heterocyclic ring, the intermediate phase $\text{Fl}_{\text{rad}}\text{Li}$ is comparatively stable during the electrochemical cycling, which results in two consecutive electron transfer reactions.

I further investigate the Mulliken population of atoms in riboflavin during the electrochemical cycling to understand the redox reaction. Mulliken charges of atoms in Fl_{ox} , $\text{Fl}_{\text{rad}}\text{Li}$, and $\text{Fl}_{\text{red}}\text{Li}_2$ of riboflavin were calculated as shown in Figure 3.5. As a result of lithium-coupled electron insertions, the electron densities of nitrogen atoms drastically increased, indicating the formation of Li-N bonds. At the same time, lithium interacts with the nearest oxygen atom, causing significant increases in electron populations of oxygen atoms. Therefore, the reduction of riboflavin molecules was dominantly localized on N5 and N1 atoms and partially on O4 and O2 atoms, indicating

that nitrogen atoms play a major role of redox centers in the molecule.

The bond lengths of the riboflavin molecules during the electron transfer were also observed by DFT calculations (Table 3.1). As expected, the sequential change in bond lengths of C4a=N5-C5a and C10=N1-C2 is observed during the reduction from Fl_{ox} to Fl_{radLi} and from Fl_{radLi} to Fl_{redLi₂}. Upon lithiation, asymmetric bonding of C4a=N5-C5a and C10=N1-C2 are successively altered into symmetric C4a–N5-C5a and C10-N1-C2 bonds. Moreover, the single bond between C4a and C10a becomes shorter, implying the conversion of a single bond to a double bond. In summary, the DFT results suggest the reversible redox reaction of riboflavin molecules during the electrochemical lithium insertion and extraction.

I further confirmed whether the lithium-coupled electron transfer reaction mechanism suggested in Figure 3.3 and 3.4 is commonly applicable to both riboflavin and lumiflavine, which is a lighter flavin molecule obtained by the substitution of ribityl side group by methyl group. Due to the lighter molecular weight, lumiflavine exhibits higher specific capacity and increased energy density. The differential capacity curves of lumiflavine electrodes exhibited two Faradaic reactions at two different voltage regions (Figure 3.6), which is in agreement with that of riboflavin.¹⁹

The results of DFT calculations conducted on the reduction behavior of the lumiflavine electrode during lithiation show that lumiflavine and riboflavin share common reduction mechanisms including the sequence of lithium occupying sites as shown in Figure 3.7 and 3.8.

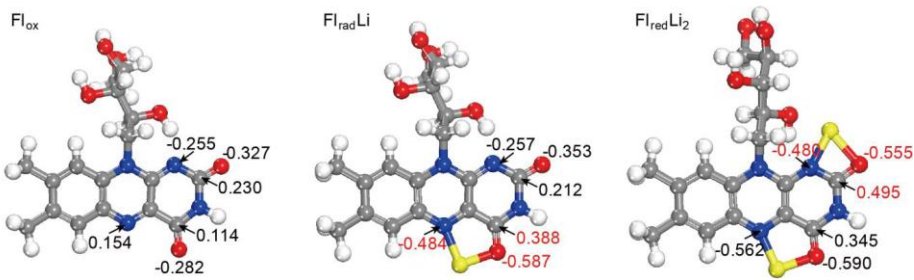


Figure 3.5. Calculated Mulliken charge changes of atoms in a riboflavin molecule during lithium coupled reduction process. As lithium inserted, the electron densities of nitrogen atoms dominantly increased indicating nitrogen atoms are the major active sites in the molecule.

Table 3.1. The major bond lengths measured from the DFT calculations.

With lithium uptake, consecutive bond-length alternation in the N5-C4a-C10a-N1 region is observed, indicating reduction.

	N5=C4a	N5-C5a	(1)-(2)	N1=C10	N1-C2	(3)-(4)	C4a-C10a
	(1)	(2)		(3)	(4)		
Fl _{ox}	1.295	1.363	0.068	1.309	1.383	0.073	1.452
Fl _{radLi}	1.366	1.368	0.002	1.325	1.369	0.044	1.416
Fl _{redLi₂}	1.394	1.374	-0.020	1.347	1.343	-0.003	1.384

The sites and sequences of lithium occupation in lumiflavine were also determined by DFT calculations following the same methods used for riboflavin. In accordance with the results of riboflavin, the most stable $\text{Fl}_{\text{rad}}\text{Li}$ and $\text{Fl}_{\text{red}}\text{Li}_2$ forms of lumiflavine have in-plane N5-Li1 bond and N5-Li1/N1-Li2 bonds as shown in Figure 3.7a and Figure 3.7b, respectively. The chemical potentials of Li in lumiflavine after the first and the second lithium insertion were determined to be 3.076 eV ($\Delta E_{\text{ox/rad}}$) and 2.275 eV ($\Delta E_{\text{rad/red}}$), respectively, based on the formation energy calculated for the most stable $\text{Fl}_{\text{rad}}\text{Li}$ and $\text{Fl}_{\text{red}}\text{Li}_2$ forms (Figure 3.8).

The common redox mechanism is also observed through the change of bonding nature within N5-C4a-C10a-N1 region (Table 3.2), and the increase in electron densities of nitrogen and oxygen atoms in the molecules (Figure 3.9). The changes in the major bond lengths in lumiflavine during lithiation/delithiation obtained from the DFT calculation clearly manifest the redox reaction of conjugated diazabutadiene in 7,8-dimethylisoalloxazine ring, consistent with the results for the riboflavin electrode (Table 3.2). With lithium insertion, C=N double bonds are reduced into single bonds changing asymmetric =N- bonds into –N- bonds. C4a-C10a single bond is oxidized into double bond with shortened bond length. Also, a slight increase in the C=O double bond lengths was observed.

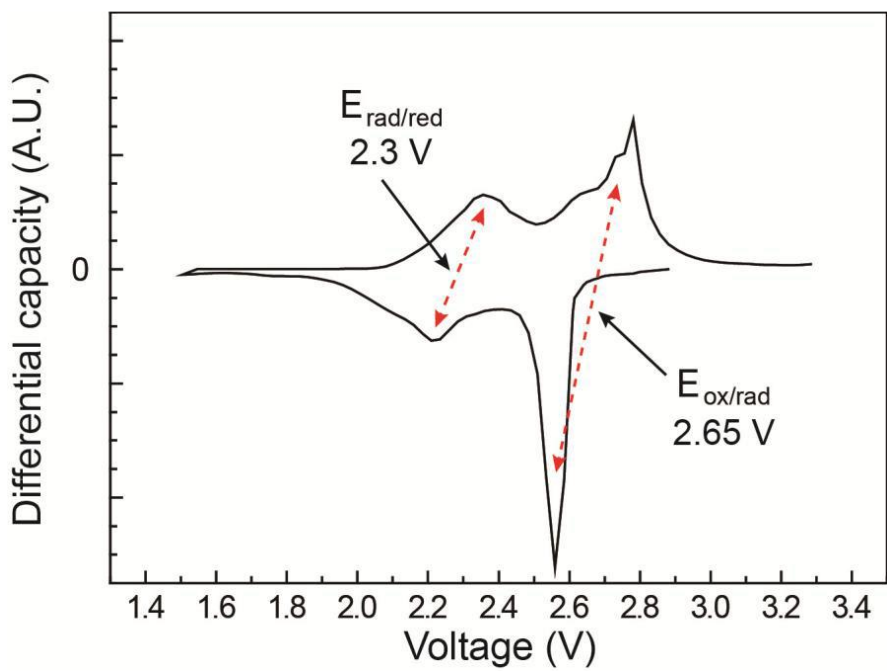


Figure 3.6. Differential capacity (dQ/dV) curves of Li/lumiflavine cell calculated from the data shown in ref.19 showing two distinctive redox peaks confirming that the redox behavior of lumiflavine follows that of riboflavin.

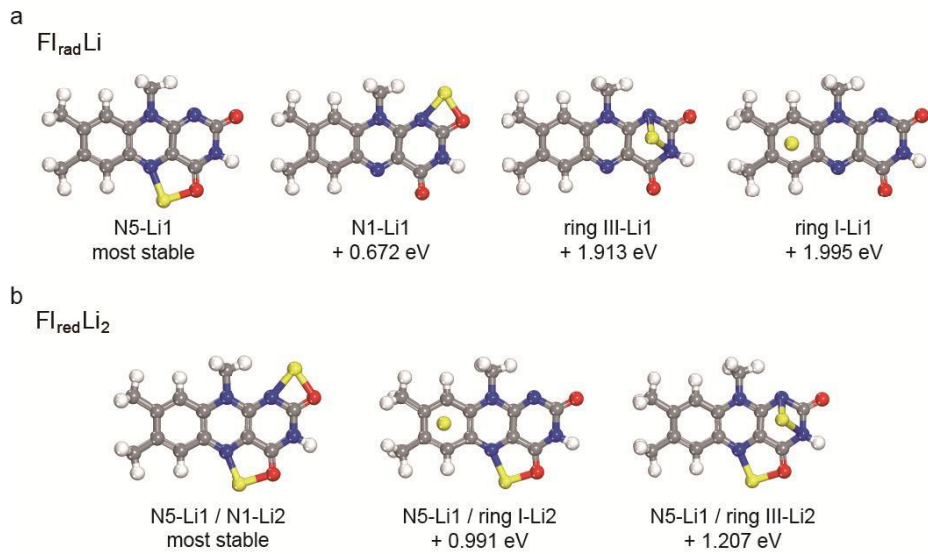


Figure 3.7. DFT energies calculated for various a) $\text{Fl}_{\text{rad}}\text{Li}$ and b) $\text{Fl}_{\text{red}}\text{Li}_2$ forms of lumiflavine. $\text{Fl}_{\text{rad}}\text{Li}$ with N5-Li1 bond and $\text{Fl}_{\text{red}}\text{Li}_2$ with N5-Li1/N1-Li2 bonds were energetically most stable for lumiflavine, in accordance with the results for riboflavin.

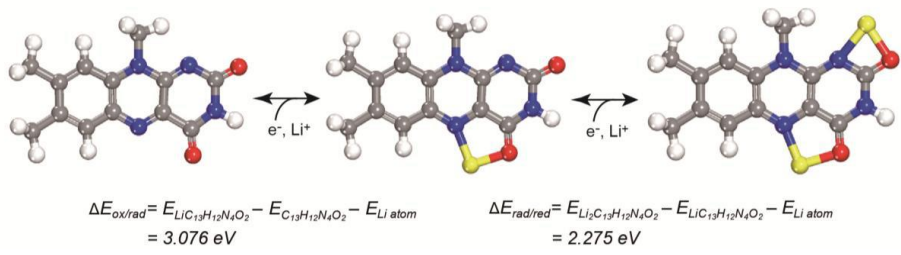


Figure 3.8. DFT calculation results on lumiflavin 3D structure and bonding nature during battery operation. Molecular structure of riboflavin upon discharge and charge calculated with relaxation process. The first Li binds to N5 and the second Li binds to N1 atom with the chemical potential values of 3.076 eV and 2.275 eV, respectively. The inserted lithium ions also interact with neighbored oxygen atoms making heterocyclic rings.

Table 3.2. The major bond length change in lumiflavine measured from the structures shown in Figure 3.8.

	N5=C4a (1)	N5-C5a (2)	(1) - (2)	N1=C10a (3)	N1-C2 (4)	(3) - (4)	C4a-C10a	C4=O	C2=O
Fl _{ox}	1.29413	1.36520	0.07107	1.30232	1.37936	0.07704	1.45754	1.21113	1.21254
Fl _{radLi}	1.36560	1.36547	-0.00013	1.31674	1.36588	0.04914	1.42083	1.26633	1.21732
Fl _{radLi₂}	1.39572	1.36995	-0.02577	1.36120	1.35173	-0.00950	1.39586	1.27219	1.27458
Fl _{ox} (ref)*	1.296	1.378		1.366			1.212	1.221	

* From M. Abe and Y. Kyogoku, Spectrochimica Acta, 1987, 43, 1027-1037



Figure 3.9. Mulliken charge changes in a lumiflavin molecule during Li-coupled reduction process. As a result of lithium-coupled electron insertions, the electron densities of nitrogen atoms where lithium attached significantly increased indicating the formation of Li-N bonds. At the same time, lithium interacts with the nearest oxygen atom causing minor increases in electron densities of oxygen. All electronic behaviors follow that of riboflavin.

Mulliken population of atoms in lumiflavine with three oxidation states was also analyzed to investigate the redox reaction of lumiflavine with lithiation (Figure 3.9). In accordance with riboflavin, the electron densities of nitrogen atoms where lithium attached drastically increased. This result indicates that the reduction of lumiflavine molecules was dominantly localized on N5 and N1 atoms.

There is one difference between the energy storage properties of riboflavin and lumiflavine in ref. 19. The greater accessibility of lithium to lumiflavine (1.67 Li per molecule) than to riboflavin (1.49 Li per molecule) implies that the kinetics of lithium diffusion should be faster in the lumiflavine electrode than in the riboflavin electrode. This can be explained by the different dynamic behaviors between ribityl and methyl side chains in each flavin observed by DFT calculation (Figure 3.5, v.s. 3.8). In case of riboflavin, the lithiation reaction causes the rotation of the ribityl group, possibly due to the electrostatic interaction between Li^+ and O^{2-} in the ribityl group, which was not observed in lumiflavine. Rigid crystalline frameworks of solid state riboflavin may kinetically hinder the distortion of the ribityl group, resulting in the limited lithium access to the active sites under moderate current flow.

3.1.4. Conclusion

In summary, the energy storage mechanism of riboflavin and lumiflavine molecules was understood by the detailed DFT calculations. Both flavin

molecules share common redox mechanisms, including the sites and the sequence of lithium insertion, the change of bonding nature within the N5-C4a-C10a-N1 region, and increases in electron densities at nitrogen (N5, N1) and oxygen atoms (O4, O2). The lithium-coupled electron transfer reactions in flavin molecules occur successively at N5 and N1 atoms due to the relatively stable intermediate phase of lithiated flavin radical compounds which is induced by the more severe strain of four-membered heterocyclic ring –C2-N1-Li2-O2-C2- compared to that of five-membered heterocyclic – C4a-C4-O4-Li1-N5-C4a- ring.

3.1.5. References

- 1 Liang, Y., Tao, Z. & Chen, J. Organic electrode materials for rechargeable lithium batteries. *Advanced Energy Materials* **2**, 742-769, doi:10.1002/aenm.201100795 (2012).
- 2 Song, Z. & Zhou, H. Towards sustainable and versatile energy storage devices: an overview of organic electrode materials. *Energy & Environmental Science* **6**, 2280-2301, doi:10.1039/C3EE40709H (2013).
- 3 Poizot, P. & Dolhem, F. Clean energy new deal for a sustainable world: from non-CO₂ generating energy sources to greener electrochemical storage devices. *Energy & Environmental Science* **4**, 2003-2019 (2011).
- 4 Chen, H. *et al.* From biomass to a renewable Li_xC₆O₆ organic electrode for sustainable Li-ion batteries. *ChemSusChem* **1**, 348-355, doi:10.1002/cssc.200700161 (2008).
- 5 Milczarek, G. & Inganäs, O. Renewable cathode materials from biopolymer/conjugated polymer interpenetrating networks. *Science* **335**, 1468-1471, doi:10.1126/science.1215159 (2012).
- 6 Liang, Y., Zhang, P., Yang, S., Tao, Z. & Chen, J. Fused Heteroaromatic Organic Compounds for High-Power Electrodes of Rechargeable Lithium Batteries. *Advanced Energy Materials* **3**, 600-605, doi:10.1002/aenm.201200947 (2013).
- 7 Huang, W. *et al.* Quasi-Solid-State Rechargeable Lithium-Ion Batteries with a Calix[4] quinone Cathode and Gel Polymer Electrolyte. *Angewandte Chemie* **125**, 9332-9336, doi:10.1002/ange.201302586 (2013).
- 8 Nishida, S., Yamamoto, Y., Takui, T. & Morita, Y. Organic Rechargeable Batteries with Tailored Voltage and Cycle

- Performance. *ChemSusChem* **6**, 794-797, doi:10.1002/cssc.201300010 (2013).
- 9 Morita, Y. *et al.* Organic tailored batteries materials using stable open-shell molecules with degenerate frontier orbitals. *Nat Mater* **10**, 947-951, doi:10.1038/nmat3142 (2011).
- 10 Lee, M. *et al.* Organic Nanohybrids for Fast and Sustainable Energy Storage. *Adv Mater* **26**, 2558-2565, doi:10.1002/adma.201305005 (2014).
- 11 Wu, H. *et al.* Flexible and Binder-Free Organic Cathode for High-Performance Lithium-Ion Batteries. *Adv Mater* **26**, 3338-3343, doi:10.1002/adma.201305452 (2014).
- 12 Nokami, T. *et al.* Polymer-bound pyrene-4,5,9,10-tetraone for fast-charge and -discharge lithium-ion batteries with high capacity. *Journal of the American Chemical Society* **134**, 19694-19700, doi:10.1021/ja306663g (2012).
- 13 Wang, S. *et al.* Organic Li₄C₈H₂O₆ Nanosheets for Lithium-Ion Batteries. *Nano letters* **13**, 4404-4409, doi:10.1021/nl402239p (2013).
- 14 Kaim, W., Schwederski, B., Heilmann, O. & Hornung, F. M. Coordination compounds of pteridine, alloxazine and flavin ligands: structures and properties. *Coordination Chemistry Reviews* **182**, 323-342, doi:10.1016/S0010-8545(98)00193-3 (1999).
- 15 Sakai, K.-i., Nagahara, K., Yoshii, Y., Hoshino, N. & Akutagawa, T. Structural and Spectroscopic Study of 6,7-Dicyano-Substituted Lumazine with High Electron Affinity and Proton Acidity. *The Journal of Physical Chemistry A* **117**, 3614-3624, doi:10.1021/jp401528c (2013).
- 16 Miura, R. Versatility and specificity in flavoenzymes: Control mechanisms of flavin reactivity. *The Chemical Record* **1**, 183-194, doi:10.1002/tcr.1007 (2001).

- 17 Joosten, V. & van Berkel, W. J. H. Flavoenzymes. *Current Opinion in Chemical Biology* **11**, 195-202, doi:10.1016/j.cbpa.2007.01.010 (2007).
- 18 Tan, S. L. J. & Webster, R. D. Electrochemically Induced Chemically Reversible Proton-Coupled Electron Transfer Reactions of Riboflavin (Vitamin B2). *Journal of the American Chemical Society* **134**, 5954-5964, doi:10.1021/ja300191u (2012).
- 19 Lee, M. *et al.* Redox Cofactor from Biological Energy Transduction as Molecularly Tunable Energy-Storage Compound. *Angew Chem Int Edit* **52**, 8322-8328, doi:10.1002/anie.201301850 (2013).
- 20 Kang, K. S., Meng, Y. S., Breger, J., Grey, C. P. & Ceder, G. Electrodes with high power and high capacity for rechargeable lithium batteries. *Science* **311**, 977-980, doi:10.1126/science.1122152 (2006).
- 21 Bréger, J. *et al.* High-resolution X-ray diffraction, DIFFaX, NMR and first principles study of disorder in the Li_2MnO_3 - $\text{Li}[\text{Ni}_{1/2}\text{Mn}_{1/2}]\text{O}_2$ solid solution. *Journal of Solid State Chemistry* **178**, 2575-2585, doi:10.1016/j.jssc.2005.05.027 (2005).
- 22 Lee, M. *et al.* Organic Nanohybrids for Fast and Sustainable Energy Storage. *Adv Mater* **26**, 2558-2565, doi:10.1002/adma.201305005 (2014).
- 23 Frisch, M. *et al.* Gaussian 09 Revision D. 01, 2009, Gaussian Inc. Wallingford CT.
- 24 Lee, C., Yang, W. & Parr, R. P. *Phys. Rev. B* 1988, 37, 785–789; c) PJ Stephens, FJ Devlin, CF Chabalowski, MJ Frisch. *J. Phys. Chem* **98**, 11623-11627 (1994).
- 25 Becke, A. D. Density-functional thermochemistry. III. The role of exact exchange. *The Journal of Chemical Physics* **98**, 5648-5652 (1993).
- 26 Schäfer, A., Huber, C. & Ahlrichs, R. Fully optimized contracted

- Gaussian basis sets of triple zeta valence quality for atoms Li to Kr.
The Journal of Chemical Physics **100**, 5829-5835 (1994).
- 27 Schäfer, A., Horn, H. & Ahlrichs, R. Fully optimized contracted Gaussian basis sets for atoms Li to Kr. *The Journal of Chemical Physics* **97**, 2571-2577, doi:10.1063/1.463096 (1992).
- 28 Klaumünzer, B., Kröner, D. & Saalfrank, P. (TD-) DFT Calculation of Vibrational and Vibronic Spectra of Riboflavin in Solution. *The Journal of Physical Chemistry B* **114**, 10826-10834 (2010).
- 29 Mulliken, R. S. Electronic Population Analysis on LCAO-MO Molecular Wave Functions. I. *The Journal of Chemical Physics* **23**, 1833-1840, doi:10.1063/1.1740588 (1955).

3.2 Pteridine redox cofactors for rechargeable batteries

(The essence of this chapter has been published in Nature Communications. Reprinted from [J. Hong *et al.* *Nat. Commun.*, 5, 5335 (2014) DOI:10.1038/ncomms6335]. Because this paper has been distributed under a Creative Commons license (Attribution-Noncommercial 2.5), one may reuse the contents for the paper for non-commercial/educational purposes without obtaining additional permission from Macmillan Publishers Ltd., providing that the author and the original source of publication are fully acknowledged.)

3.2.1. Research background

In our continuing efforts to pioneer biologically inspired energy materials in sustainable rechargeable batteries,^{1,2} herein we report a novel class of biological redox units as a high performance battery electrode, namely, *pteridine redox centers*, which are essential constituents in cellular energy metabolism, along with the novel strategy for tailoring these biological redox units to achieve one of the best electrochemical performances available at this time.

In this chapter, present a molecular simplification strategy to design a minimal redox-active unit of diazabutadiene redox cycle through electrochemical tailoring. In the pursuit of the minimization, the removal of the ribityl substituent from flavin molecules leads to a structural change from

isoalloxazines to alloxazines that possess distinct chemical and physical properties.³ The resulting pteridine derivatives in alloxazinic structure are firstly exploited in lithium and sodium rechargeable battery systems as a novel class of organic cathodes. The spectroscopic and computational studies unveil the differences of underlying energy storage mechanisms between isoalloxazic and alloxazinic systems. Furthermore, by introducing nanocarbons as a conductive scaffold for molecule immobilization during electrode preparation, we demonstrate that the pteridine derivatives exhibit outstanding electrochemical performance in terms of power and cyclability in battery operations. The molecular simplification strategy combined with the experimental and theoretical analyses augments the pool of organic electrode materials and provides guidance for rational design of organic redox centers.

3.2.2. Experimental and computational details

Electrochemistry. Electrochemical profiles of lumichrome, alloxazine and lumazine powder samples were measured versus a Li metal foil (Hohsen Corp., Japan) and a Na metal cube (Sigma Aldrich, USA) in coin-type cells (CR2016). The electrodes were fabricated by casting a slurry of 40 % w/w active materials, 40 % w/w conductive carbon (Super P[®]) and 20 % w/w sodium CMC (carboxymethyl cellulose) binder mixed in distilled water on Al foil. The electrodes were dried overnight at 60 °C under vacuum. In the modified electrode preparation, hybrid electrodes were produced by simply

mixing the organic compounds and single-walled carbon nanotubes in acetone using a sonicator followed by vacuum filtration. The resulting self-standing paper was used as itself as electrodes without current collectors and additives. A porous glass microfiber membrane (GF/F, Whatman) was used as separator in both the Li- and Na-ion cells. The electrolytes were 1M LiPF₆ in TEGDME (tetraethylene glycol dimethyl ether, Techno Semichem Co., Ltd., Korea) for Li-ion cells and 1M NaPF₆ in DEGDME (diethylene glycol dimethyl ether) for Na-ion cells respectively. The cells were assembled under inert atmosphere within Ar-filled glove box. The galvanostatic measurements were carried out at various constant current densities on a battery test system (Won-A Tech, Korea).

***Ex situ* electrode characterization.** For *ex situ* analyses, the electrodes were prepared by disassembling coin cells at the different states of charge (as-prepared, half-discharged, fully discharged to 1.6 V, half-charged, fully recharged to 3.6 V) followed by rinsing electrodes with DMC. To prevent exposure to air, all the samples were sealed in an Ar-filled glove box. X-ray photoelectron spectroscopy (XPS) measurements were conducted with a Thermo VG Scientific Sigma Probe spectrometer (U.K.) equipped with a microfocus monochromated X-ray source (90 W). Binding energies were referenced to C-C bond of C 1s region as 284.5 eV. FTIR spectra of pellets made of mixture of active powders scraped out of the electrodes and KBr powder were recorded on a FT/IR-4200 (Jasco Inc., Japan) at a resolution of 2 cm⁻¹ under vacuum. For fluorescence spectroscopy, samples were

immersed in degassed deionized water in nitrogen atmosphere, resulting in solubilized active molecules. Fluorescence spectra were obtained using a V/650 spectrophotometer (Jasco Inc., Japan) in the range of 400-600 nm.

Computational details. Geometry optimization and energy calculations on the all molecules were conducted with spin-unrestricted density functional theory (DFT) using the Gaussian 09 quantum chemistry package⁴ based on Becke-Lee-Yang-Parr (B3LYP) hybrid exchange-correlation functional^{5,6} and the standard TZVP basis set.⁷⁻⁹ The site and sequence of lithium occupation during redox reaction were determined by comparing DFT energies of possible reduced forms of molecules bonded to one or two lithium ions. Atomic charge was calculated with Mulliken population analysis.¹⁰ Detailed procedure and the results of DFT calculations are discussed in the Supplementary Information. The HOMO plots were generated with cubegen utility which is embedded in Gaussian 09⁴ and visualized with the Materials Studio program.

3.2.3. Results and discussion

Molecular tailoring of pteridine systems for lithium storage

To increase energy density, we simplified the chemical structure of flavin molecules by removing non-redox-active substituents from the molecules while maintaining the redox-active moiety (Figure 3.10). The center of redox reactivity in flavins is the isoalloxazine ring system, specifically the conjugated diazabutadiene (N5-C4a-C10a-Ni1) region that facilitates the

lithium-coupled electron transfer reaction *via* sequential reduction of N5 and N1 (Figure 3.11).¹ Without the ribityl substituents, that yields a simpler molecule lumichrome (7,8-dimethylalloxazine, LC), flavin could no longer maintain its isoalloxazinic form. Rather, LC formed an alloxazine-type structure, in which N1 and N3 (instead of N10 and N3) are substituted as shown in Figure 3.10.¹¹ Although the structures of isoalloxazines and alloxazines are closely related, the chemical and physical properties of these two systems differ significantly.¹²

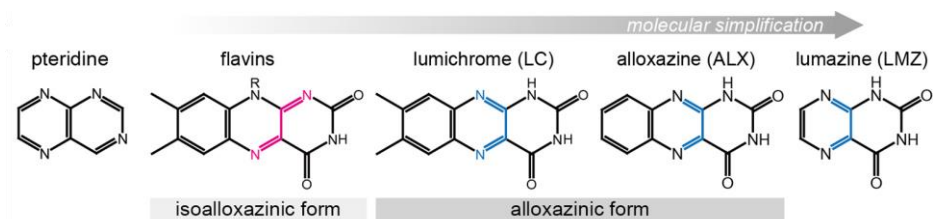


Figure 3.10. Molecular structures of pteridine derivatives as bioinspired redox compounds for energy storage.

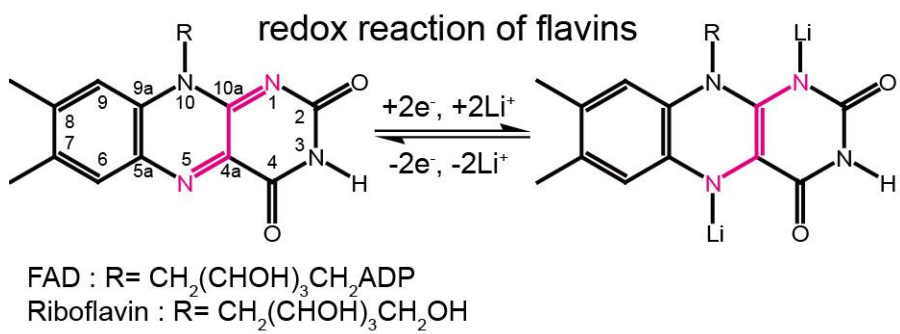


Figure 3.11. Redox mechanism of flavins inspired by biological energy transduction.

For example, each system shows different photoemission bands: the excited-state lifetime of the isoalloxazinic structure is longer than that of the alloxazines, and the isoalloxazinic structure exhibits stronger emission intensity. Based on these photophysical differences, previous studies on LC observed an interesting phenomenon called excited-state tautomerism, which is a structural isomerism from alloxazine to isoalloxazine (Figure 3.12).^{13,14} However, few studies have explored the redox chemistry of LC. To the best of our knowledge, the reversible tautomeric reaction of LC during electrochemical reactions has not been demonstrated previously, which will be discussed below. We further searched for simpler forms of the pteridine redox center by sequentially removing substituents which are alloxazine (ALX, without the methyl groups at C7 and C8 of LC) and lumazine (LMZ, without the anellated benzo ring of ALX).

The redox properties of pteridine derivatives were first investigated with cyclic voltammetry (CV) using percholate electrolytes in N,N-dimethylformamide (DMF) under N₂ atmosphere (Figure 3.13). In TBAP (tetrabutylammonium percholate) which contains (TBA⁺) as noninteracting cations, all the pteridine derivatives shows two well-defined reduction and oxidation peaks with high reversibility in CV curves, indicating two-step one-electron transfer processes. The use of LiClO₄ as the supporting electrolyte resulted in positive shifts of the redox potentials due to the ionic stabilization of the reduced molecules by lithium ions, suggesting the capability of lithium-coupled redox reactions in pteridine derivatives.^{15,16}

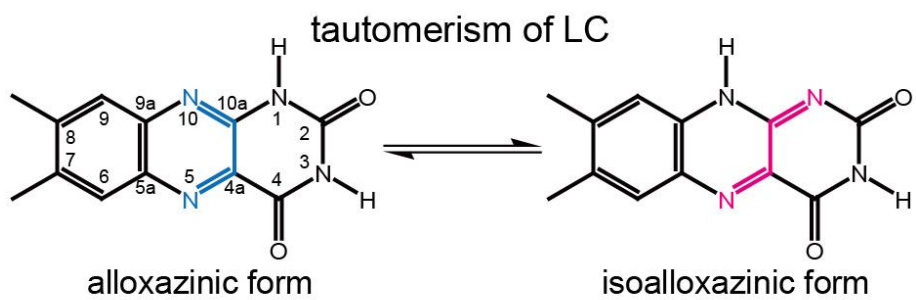


Figure 3.12. Reversible tautomerism of LC, which is a structural isomerism from alloxazine to isoalloxazine.

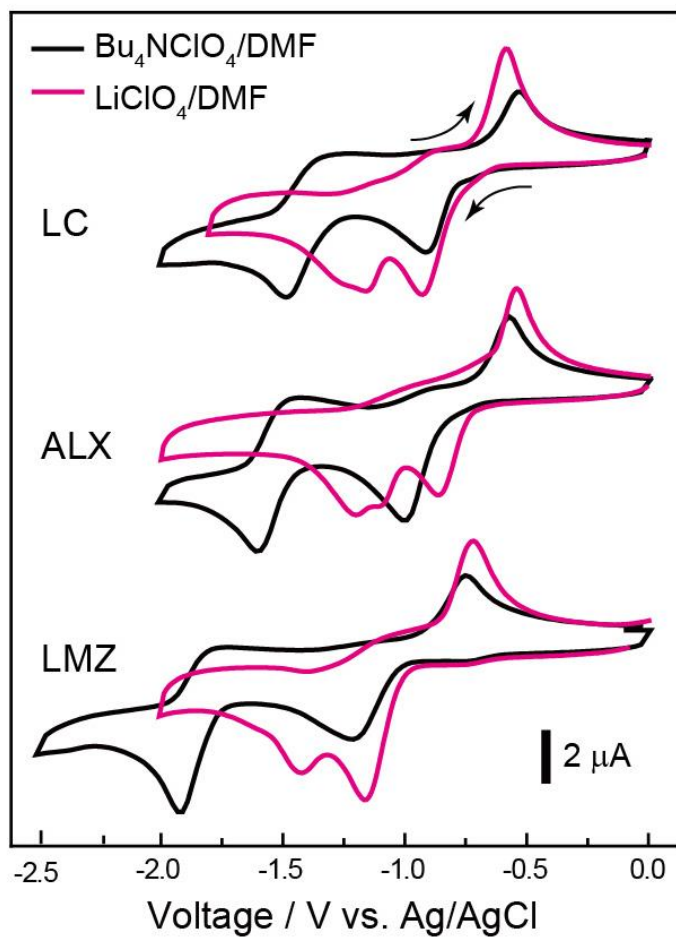


Figure 3.13. Cyclic voltammograms (CV) of pteridine derivatives measured in DMF solutions containing TBAP (black) and LiClO_4 (red) as electrolytes.

Lithium storage mechanism of LC

As the first step to utilize pteridine derivatives in lithium storage, we examined the electrochemical activity of the LC electrode versus lithium counter electrode in a coin-type cell. According to our galvanostatic measurements, LC/Li cells could reversibly take up and release two lithium ions and electrons. The specific capacity of LC/Li cell was approximately 169 mAh g^{-1} , equivalent to 1.53 Li atoms per molecule between 1.5 and 3.6 V at a current density of 20.0 mA g^{-1} (Figure 3.14). When we apply high temperature (60°C) to the battery operation of LC, its capacity reached to 181 mAh g^{-1} (Figure 3.15). The theoretical capacity corresponding to two Li atoms in the LC electrode is 221 mAh g^{-1} . Two sets of distinctive cathodic and anodic peaks were observed with average potentials of 2.50 and 2.35 V based on differential capacity curves (Figure 3.14, inset). The result indicated that the electrode reaction of LC followed two consecutive lithium insertion reactions with a relatively stable intermediate phase, which resembles the redox chemistry of riboflavins in lithium cells.¹ We also performed a galvanostatic intermittent titration technique (GITT) measurement under an intermittent discharge/charge for 1 hour at a low current rate of 10.0 mA g^{-1} with relaxation periods maintained for 5 hours.

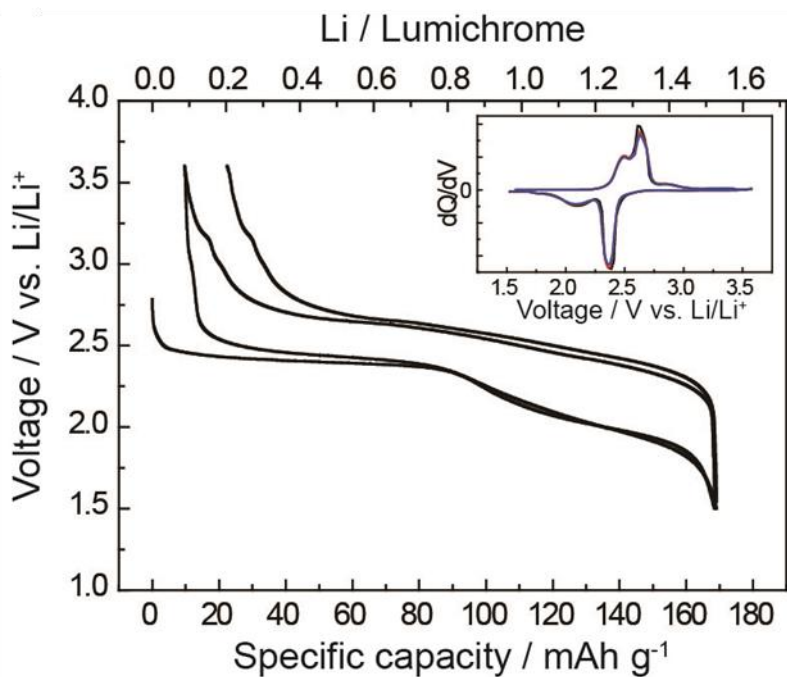


Figure 3.14. Capacity-voltage profiles and the corresponding differential capacity plots (inset) of LC/Li cells.

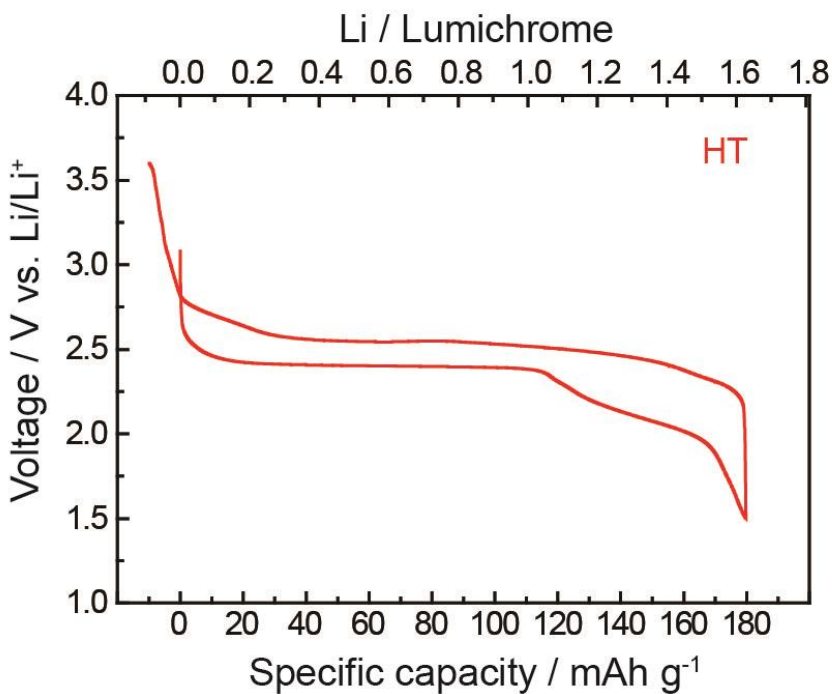


Figure 3.15. Capacity-voltage profile of a LC electrode obtained at high temperature (60°C). The LC electrode show higher capacity with lower polarization at high temperature compared to that at room temperature.

The GITT result in Figure 3.16 shows that the open circuit voltage (OCV) of LC was nearly unchanged at 2.50 V during the first reduction by lithiation, while the OCV continuously decreased during the second stage of the reduction. During the recharge period, the OCV continuously increased to 2.50 V, and then remained flat until the majority of lithium ions were extracted from LC. The flat potential in the electrochemical profile suggests that lithium insertion followed a two-phase-based reaction in the region, which is known to occur in conventional olivine LiFePO₄ electrodes.

To characterize the redox mechanism of LC, we performed *ex situ* experimental and computational studies of the electrode during battery operation. Changes in the crystal structure of LC were first investigated by comparing X-ray diffraction (XRD) patterns of LC electrodes at various states, including as-prepared, fully discharged, and fully recharged states (Figure 3.17). We found that the as-prepared electrode comprising crystalline LC powders became lost the long-range crystalline order on the first discharge and partially restored its original crystallinity on the recharge. The amorphization of the electrodes upon cation insertion is often observed for the organic active materials which is attributable to the relatively weak interactions (van der Waals force, hydrogen bond) among the molecules comprising the crystalline structure.^{17,18} Nevertheless, the electrodes still retained the redox activity for continuous battery operation which implies that the electrochemical activities are not dominated by the long-range crystalline order of organic electrode materials.

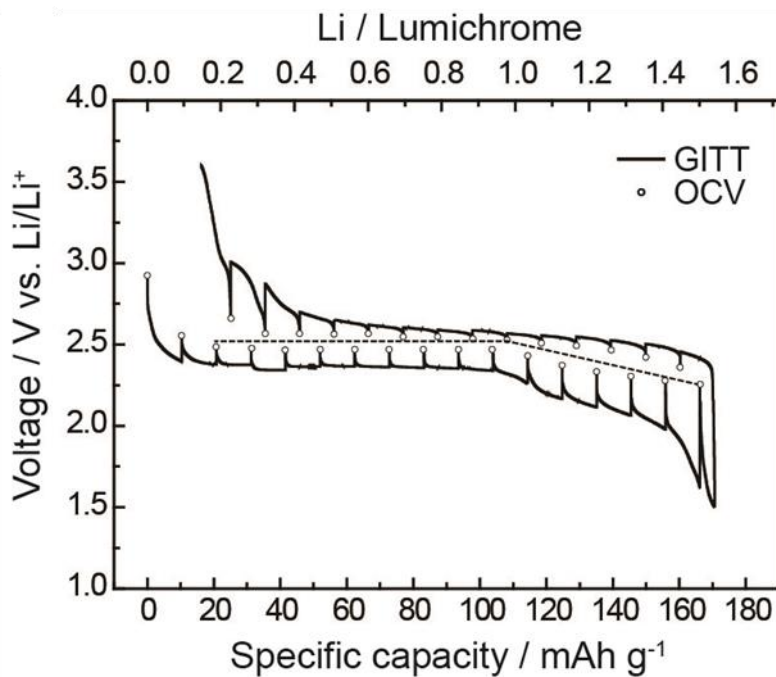


Figure 3.16. GITT profiles of the LC/Li cells under an intermittent discharge/charge for 1 hour at a low current rate of 10.0 mA g⁻¹ with relaxation periods maintained for 5 hours.

To identify the evolution of molecular structure during the electrochemical reactions, we performed various spectroscopic analyses. High-resolution XPS scans of the electrodes confirmed the reversible lithium insertion and extraction in LC during battery cycling (Figure 3.18). In the Li 1s spectra, the lithium peaks reversibly evolved with the discharge and disappeared with subsequent charging of the LC electrode. The electron density in nitrogen and oxygen atoms of LC changed according to lithiation and delithiation, suggesting that these atoms are redox-active centers. The peak in the N 1s spectra of the as-prepared electrode (full-width at half-maximum, FWHM: 2.23 eV) was broadened during the discharged state (FWHM: 2.57 eV) and then recovered after recharge (FWHM: 2.25 eV), which shifted the peak to lower energies and then back to the initial value. For the as-prepared electrode, the N 1s spectrum could be deconvoluted into two peaks with the same FWHM of 1.60 eV centered at 399.15 and 400.15 eV, which were assigned to conjugated (sp^2) $-N=$ and non-conjugated (sp^3) $-NH-$ groups, respectively.¹⁹ After discharge, an additional peak evolved at a lower binding energy, 398.40 eV, while the $-N=$ peak (399.15 eV) decreased, implying that reduction occurred at nitrogen atoms in the pyrazine ring. The new peak could be designated as N–Li, which was similar to that commonly observed in lithium azide.²⁰ For a recharged electrode, the reversible diminution of the N–Li peak at 398.40 eV, as well as restoration of the $-N=$ peak was observed, which is in agreement with the redox reaction of LC versus lithium. In the O 1s spectra, a slight downshift of the O 1s binding energy

peak was detected in the discharged state, which indicated that the electron density of oxygen atoms also increased during lithiation-involved reduction of LC.

Ex situ FTIR analysis shown in Figure 3.19 further confirmed the reversible change in the molecular structure of LC during the redox reaction involving lithium insertion/extraction. As LC/Li cells were discharged and recharged, peaks at 1278, 1561, and 1578 cm⁻¹ corresponding to the vibrational modes of C4a–C10a single bond and C=N double bonds²¹ [$\nu(N10=C10a)$, $\nu(N5=C4a)$] gradually disappeared and reappeared. This result represents that the conjugated diazabutadiene motif (-N=C–C=N-) participated in the redox reaction of LC, in agreement with the XPS results. In addition, we found that the vibrational modes of C=O bonds²² were reversibly eliminated and restored not only for C4 but also for C2 at 1697 and 1723 cm⁻¹, respectively, denoting that all lithium insertion reactions occur at the nitrogen atoms neighboring oxygen atoms. This observation points to an interesting configurational change of the molecule during lithiation. Since N10 does not neighbor a C=O bond, as shown in 3.12, it is expected that the N1 neighboring C=O participates in lithium insertion, although the N1 atom is already bound to a proton in the pristine alloxazine form. This strongly suggests that tautomerism to the isoalloxazinic structure occurred electrochemically to form the N1–Li–O–C2 heterocyclic structure by accompanying proton transfer from N1 to N10.

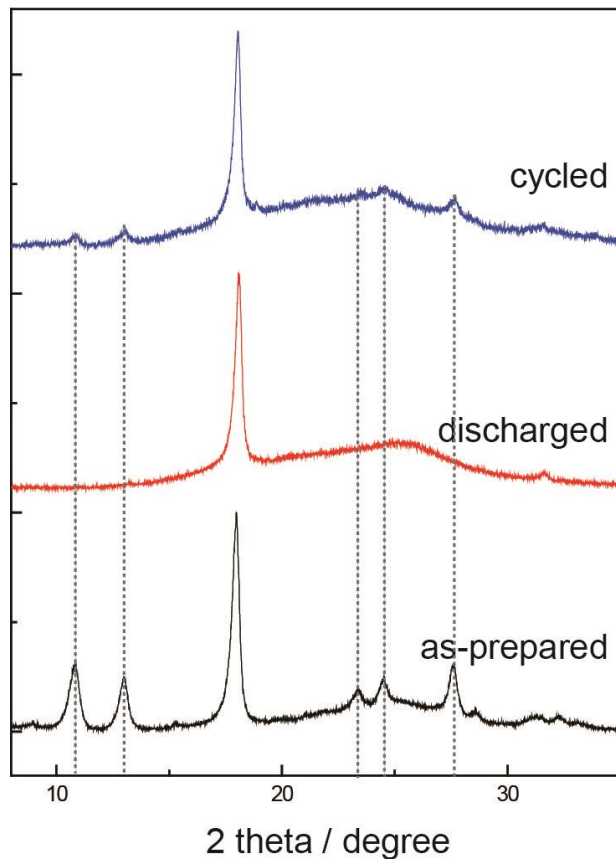


Figure 3.17. *ex situ* XRD analysis for LC electrodes at as-prepared (black), fully discharged (red), and fully recharged (blue) states. The amorphization of the crystal structure was observed for the first discharge process which was only partially recovered after the recharge.

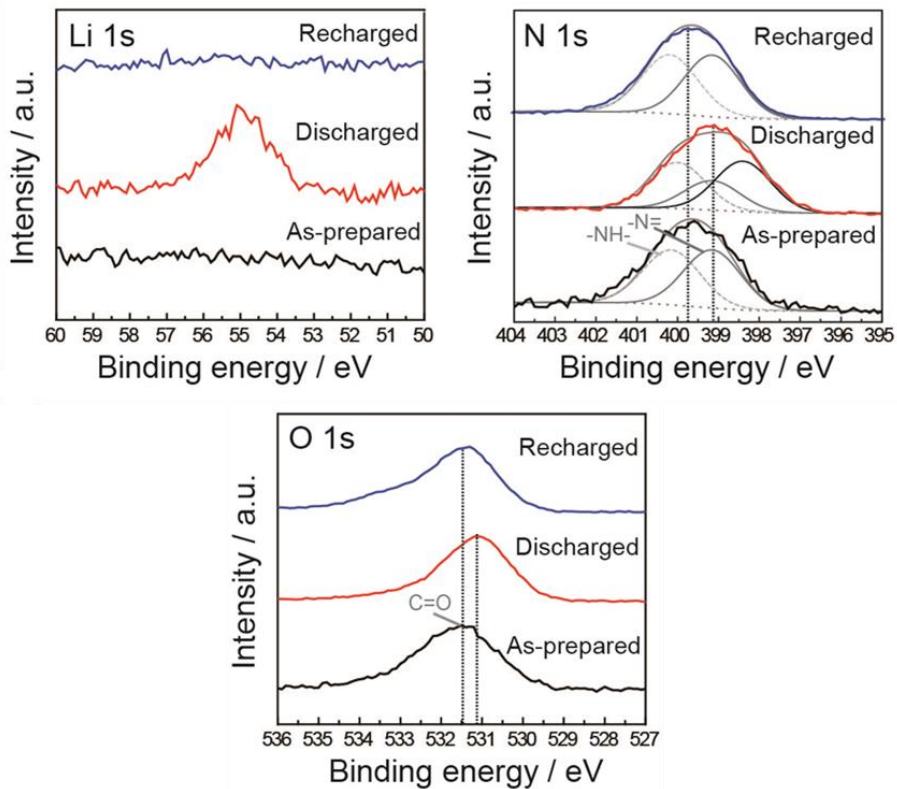


Figure 3.18. *Ex situ* XPS analysis of LC electrodes at different states of charge during battery cycling. XPS local scan spectra of Li 1s, N 1s, and O 1s regions reversibly switching upon reduction and oxidation of the LC.

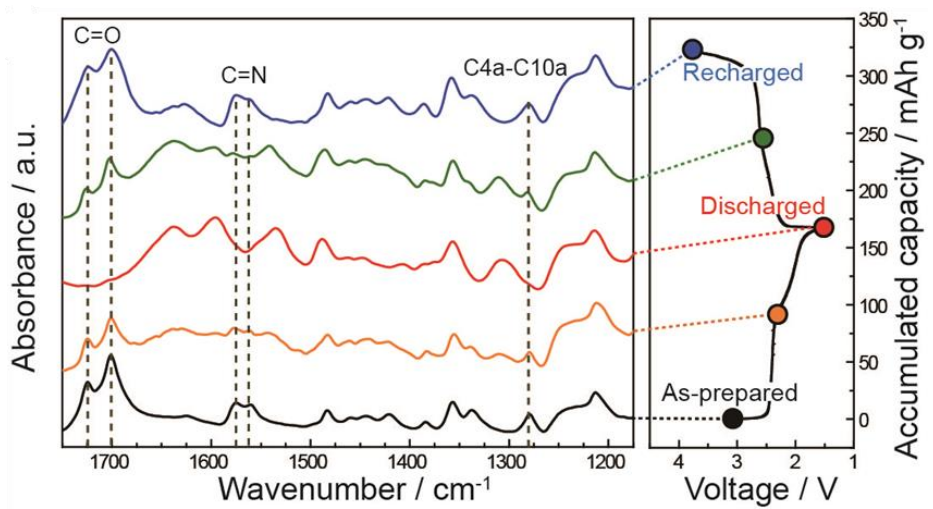


Figure 3.19. *Ex situ* FTIR spectra of LC electrodes during electrochemical cycling which is reversibly switching upon reduction and oxidation of the LC.

We further monitored the configuration change of LC during reduction and oxidation in battery using fluorescence spectroscopy (Figure 3.20). After reduction (*i.e.*, discharge), the appearance of isoalloxazinic fluorescence at 520 nm and the disappearance of alloxazinic fluorescence at 450 nm at the discharged state were clearly observed which agreed with previous reports on phototautomerism.^{13,14} After recharging, the LC showed fluorescence at 450 nm again, suggesting that the tautomerism of alloxazine to isoalloxazine was completely reversible during the lithium-coupled redox reaction. The photo-induced tautomerism of LC has been well-characterized,^{13,14} but the similar tautomerism to the isoalloxazinic structure that occurred electrochemically during lithium-coupled electron reduction was unexpected.

Our experimental results on the redox mechanism of LC accompanying tautomerism were supported by density-functional theory (DFT) calculations (B3LYP hybrid functional). First, we explored how many electrons could be maximally adopted and how they were distributed in LC by examining the highest occupied molecular orbitals (HOMO) of the molecule. The HOMO plot of a molecule provides qualitative information on its capability of accepting electrons in a given molecular structure.²³ When the LC molecule is reduced by accepting two electrons, effective electron delocalization occurs in the conjugated structure of reduced LC (LC^{2-}) (Figure 3.21). Further reduction, however, does not allow the molecule to stabilize the electrons (3.22), indicating that LC is capable of a two-electron redox reaction. It was further noted that reduced LC (LC^{2-}) was more stable in the

isoalloxazinic form than in the pristine alloxazine form by 0.299 eV.

To improve our understanding on the redox mechanism of LC, we compared DFT energies of possible lithium configurations for [LC]Li and [LC]Li₂ (Figure 3.23). It was found that [LC]Li containing N5–Li bond where the lithium ion also interacted with O4 was the most stable structure by more than 1.80 eV among various possible configurations, and the alloxazinic structure was favored over the isoalloxazinic tautomer by 0.23 eV under vacuum. In a more realistic simulation in the presence of electrolytes, however, I found notable distinction in preferred configuration (Figures 3.24, 3.25). While the alloxazinic form of [LC]Li was still preferred in a nonpolar solvent (ϵ : 3.04) by 0.101 eV similar to the result in vacuum condition, the isoalloxazinic form became more stable by 0.016 eV in a polar solvent (ϵ : 78.4). This result implies that the choice of electrolyte strongly affects the electrochemical reaction path of tautomeric redox compounds. For the fully discharged [LC]Li₂, the second Li prefered to be located between N1 and O2 more than other positions, which accompanied proton transfer from N1 to N10. Furthermore, the charge densities successively increased on nitrogen and oxygen atoms during two-step lithiation (Figure 3.25). These results agree with the aforementioned *ex situ* spectroscopy results and confirm that nitrogen and oxygen atoms work as collaborative centers for the tautomerism-involving redox reaction.

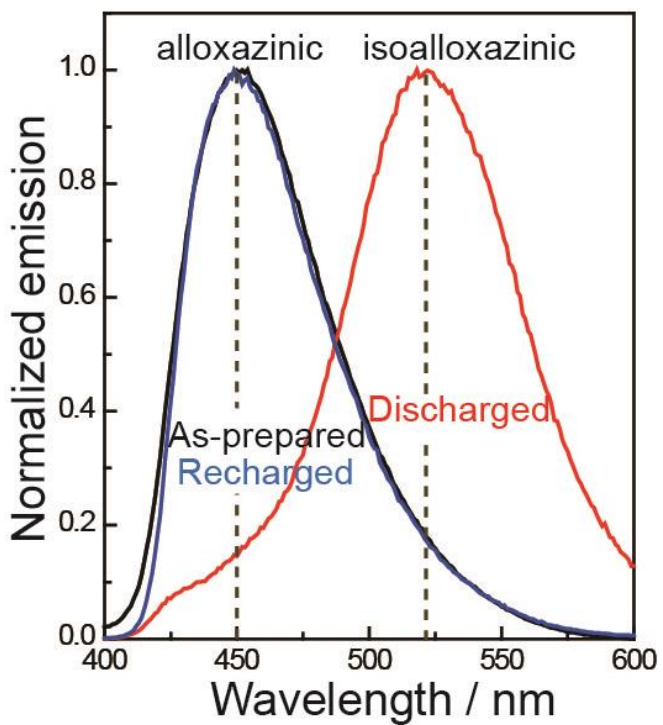


Figure 3.20. *Ex situ* emission spectra are reversibly switching upon reduction and oxidation of the LC which is indicative of the redox stability of alloxazinic systems and the tautomerism of LC during battery cycling.



Figure 3.21. DFT calculation on LC during redox reactions. HOMO plots of LC and doubly reduced LC tautomers.

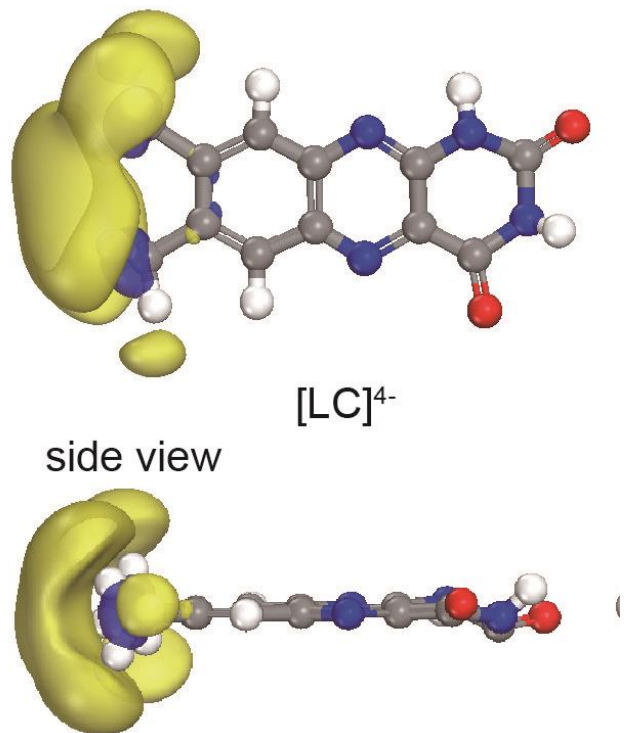


Figure 3.22. HOMO plots of tetravalent anion lumichrome (LC). LC molecule fails to retain the valence-shell electrons within the structure, indicating that irreversible chemical reactions possibly occur during four-electron reduction.

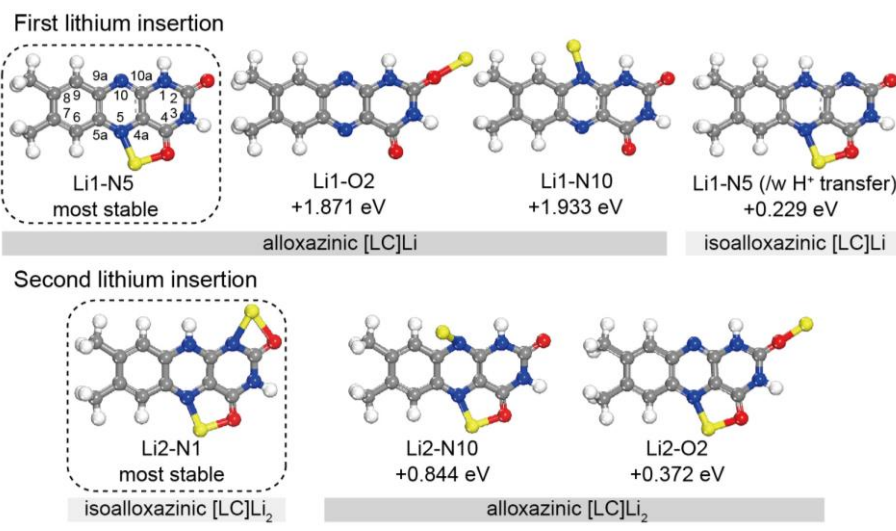


Figure 3.23. DFT energy comparison for various forms of [LC]Li (upper) and [LC]Li₂ (lower) upon two lithium coupled-two electron reduction.

Molecular simplification to a minimal unit of diazabutadiene cycling

Inspired by the remarkable electrochemical activity of LC, we further tested ALX and LMZ with theoretical capacities of 240 and 327 mAh g⁻¹, respectively, assuming that they store two lithium atoms per molecule similar to rivoflavin and LC electrodes. The feasibility of the electrochemical activity was first screened by computationally reducing each molecule. In the HOMO plot of the reduced ALX and LMZ, the effective delocalization of electron clouds was observed up to two electrons, suggesting that they can be utilized as redox centers for two lithium ion storage (Figure 3.26). DFT calculations with actual lithium occupancies in each molecule confirmed that two lithium ions could be stored in both ALX and LMZ by undergoing similar tautomerism-accompanied redox reactions as LC (Figures 3.27, 3.28). Similar to the LC, both ALX and LMZ were found to be not capable of accepting four electrons as shown in Figure 3.29.

I next explored the electrochemical activity of ALX and LMZ electrodes in Li cells. As predicted by our calculations, more than one lithium ion and electron were reversibly stored in each molecule of ALX and LMZ, respectively. The ALX/Li cell showed a specific capacity of 181 mAh g⁻¹ at 20.0 mA g⁻¹ current density, corresponding to 1.45 Li atoms per molecule (Figure 3.30). The GITT measurement with a lower current rate indicated that a capacity of 211 mAh g⁻¹ (1.69 Li/ALX) could be reversibly delivered. Analogous to the LC electrode, the electrochemical profile could be divided into two redox steps with average OCVs of 2.52 V and 2.42 V, respectively

which implied that two consecutive one-electron transfer reactions similarly occurred for ALX as well. In contrast, the LMZ electrode showed slightly different electrochemical profiles compared to LC and ALX with relatively larger polarizations (Figure 3.31). At room temperature, the LMZ/Li cell delivered a reversible capacity of 154 mAh g^{-1} , which is equivalent to only 0.94 Li atom per molecule. The limited capability of lithium storage accompanied with the large polarization of $\sim 1.6 \text{ V}$ (Figure 3.32), indicated that the relatively low capacity of the LMZ electrode may stem from the slow electrochemical reaction of LMZ. When we offered higher temperature (60°C) or sufficiently low current density (intermittent current of 10.0 mA g^{-1} , Figure 3.33, bottom) to LMZ/Li cells, the electrochemical activity of LMZ improved significantly. The LMZ/Li cells showed specific capacities of 251 mAh g^{-1} (1.54 Li/LMZ) and 193 mAh g^{-1} (1.18 Li/LMZ) under the high-temperature cycling and GITT test, respectively. It implies that two lithium ions may be stored in LMZ, which is in agreement with our calculations; however, the lithiation kinetics were slow. The underlying reason for the slow lithiation kinetics particularly for the LMZ electrode is not fully understood yet. However, we speculate that the smaller molecular framework of LMZ compared to other molecules may induce comparatively stronger electron repulsion within the molecules when accepting two electrons.

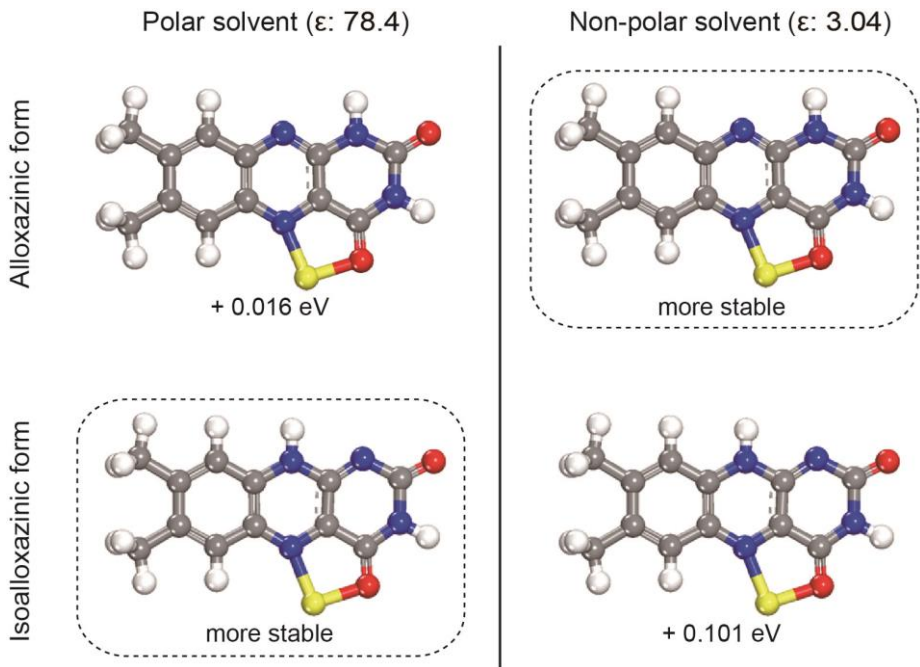
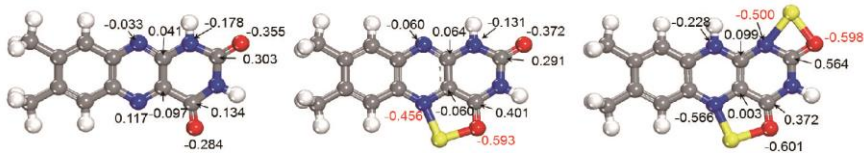
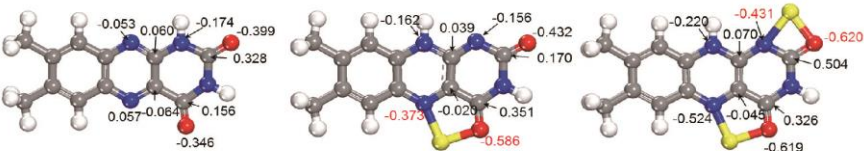


Figure 3.24. DFT calculation for comparing two tautomer forms of [LC]Li in solvents. In polar solvent, isoalloxazinic form of [LC]Li is more stable than alloxazinic form, and *vice versa* in non-polar solvent. The negligible energy difference between two tautomeric [LC]Li molecules in polar solvent indicates that co-presence of the both forms is possible.

a) non-polar



b) polar



c) bond lengths

non-polar	LC	$LC_{rad}Li$	$LC_{red}Li_2$	polar	LC	$LC_{rad}Li$	$LC_{red}Li_2$
$d_{C4a=N5}$	1.328	1.371	1.402	$d_{C4a=N5}$	1.314	1.367	1.406
$d_{C10a=N10}$	1.311	1.314	1.362	$d_{C10a=N10}$	1.311	1.364	1.367
$d_{C4a-C10a}$	1.430	1.417	1.392	$d_{C4a-C10a}$	1.425	1.414	1.392
$d_{C10a-N1}$	1.388	1.390	1.358	$d_{C10a-N1}$	1.382	1.332	1.350

Figure 3.25. Changes in Mulliken charge of atoms (a, b) and bond lengths (c) in lumichrome molecules during discharge in non-polar (ϵ : 3.04) and polar solvents (ϵ : 78.4) during Li-coupled reduction processes. Calculated values that are varied significantly are indicated with red letters and blue letters. As lithium inserted, the charge densities dominantly increased on nitrogen atoms in diazabutadiene motif indicating the nitrogen atoms are the major redox loci in the molecule.

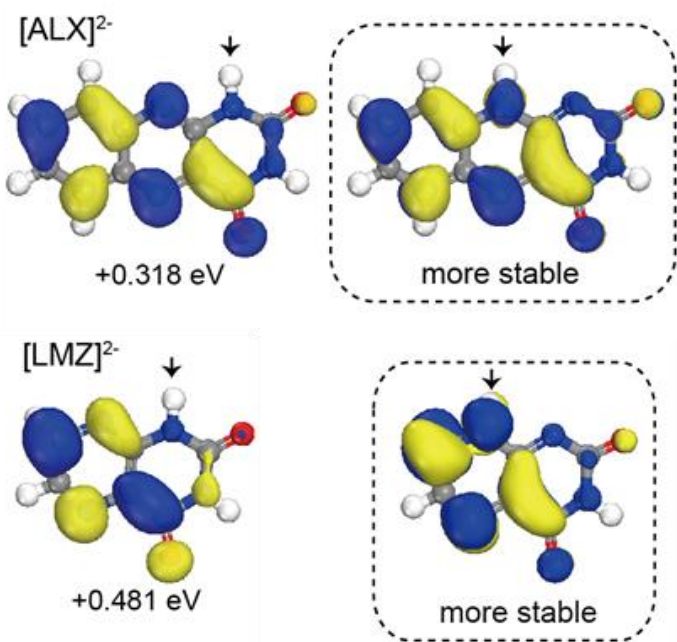


Figure 3.26. HOMO plots for the doubly reduced species of ALX and LMZ.

Black arrows indicate the proton which is bound to N1 or N10.

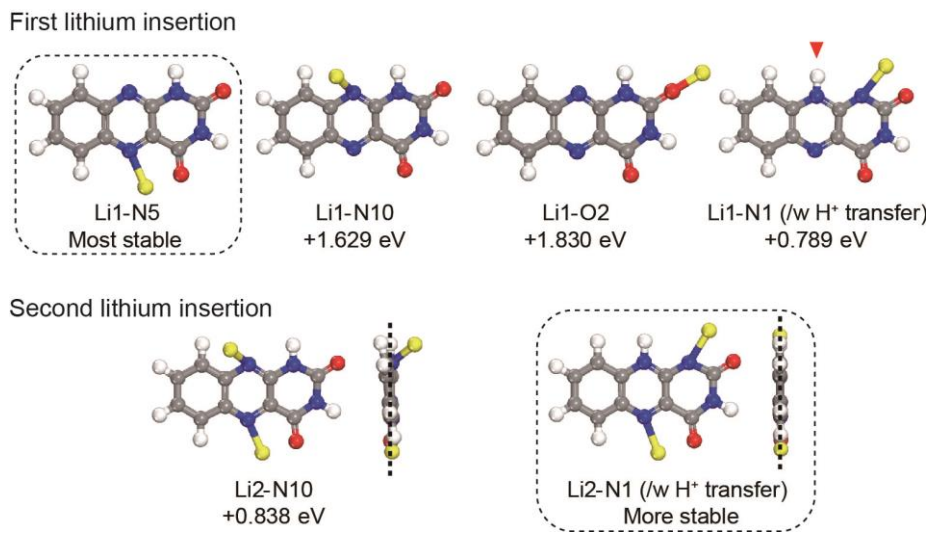


Figure 3.27. DFT energies for lithiated alloxazine molecules with various configurations. It is stable that the first lithium atom is inserted into N5 and the second is inserted to N1 accompanied with the tautomeric transformation of the alloxazine molecule into isoalloxazinic form.

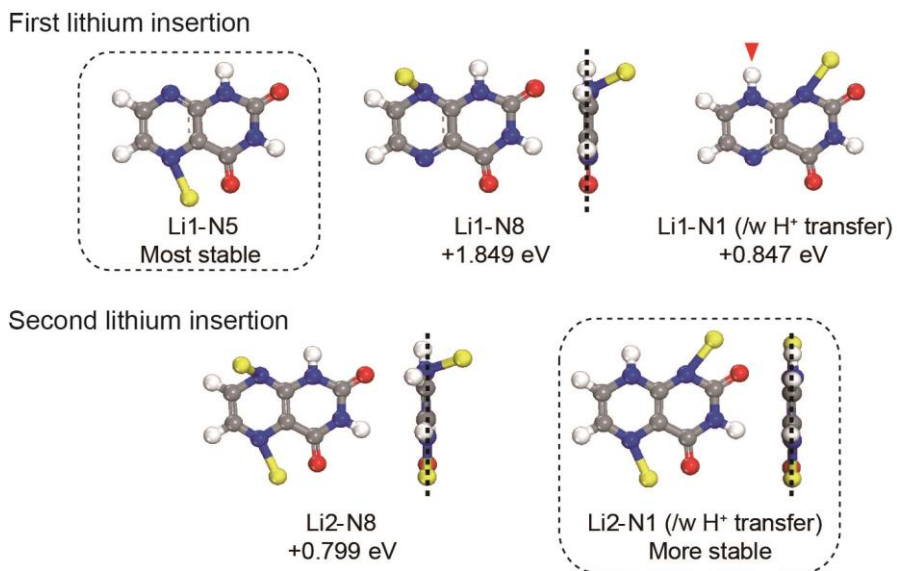


Figure 3.28. DFT energies for lithiated lumazine molecules with various configurations. It is stable that the first lithium atom is inserted into N5 and the second is inserted to N1 accompanied with the tautomeric transformation of the lumazine molecule.

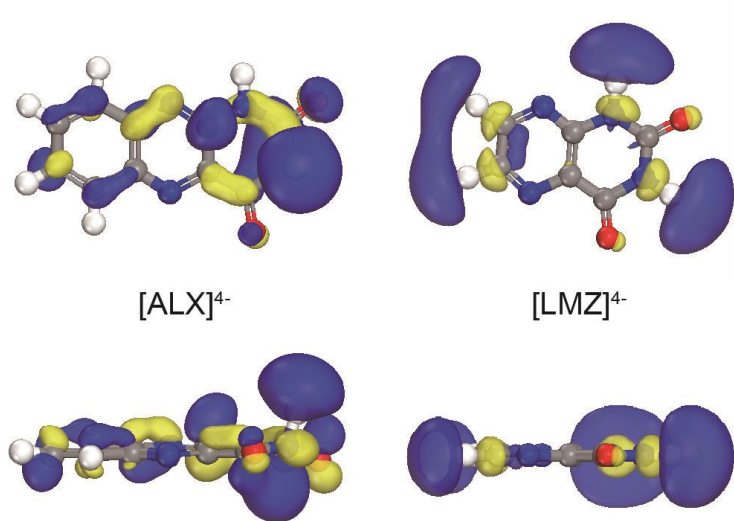


Figure 3.29. HOMO plots of tetravalent anion pteridine derivatives, ALX and LMZ. They fail to retain the valence-shell electrons within the structure, indicating that irreversible chemical reactions possibly occur during four-electron reduction.

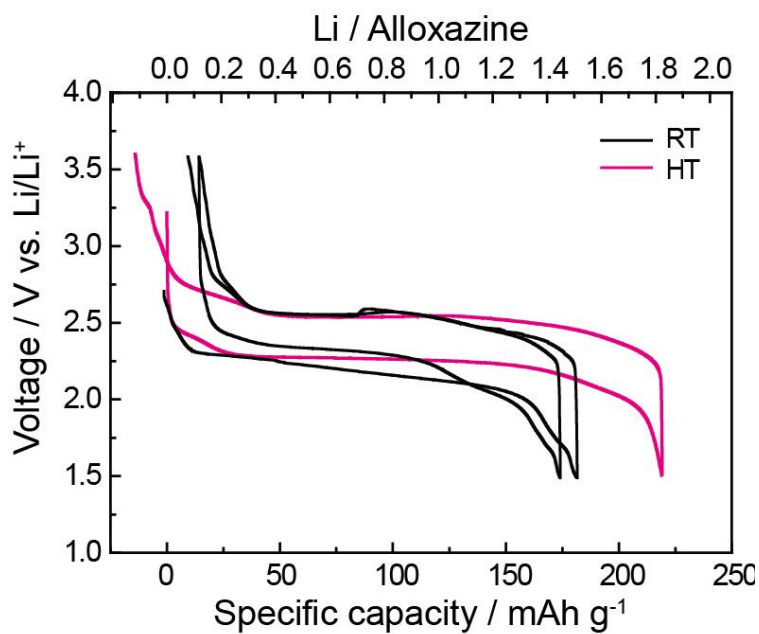


Figure 3.30. Capacity-voltage profiles of ALX electrode at room temperature (black) and 60°C (red).

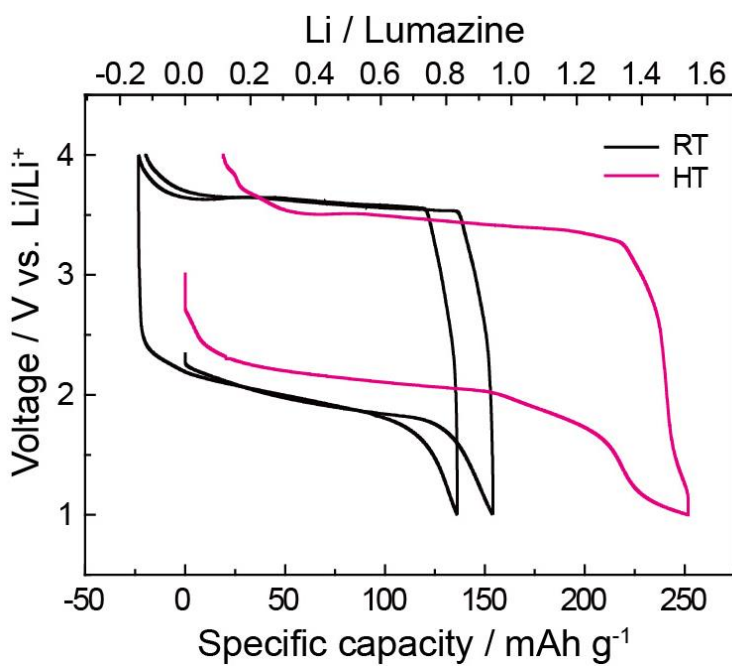


Figure 3.31. Capacity-voltage profiles of LMZ electrode at room temperature (black) and 60°C (red).

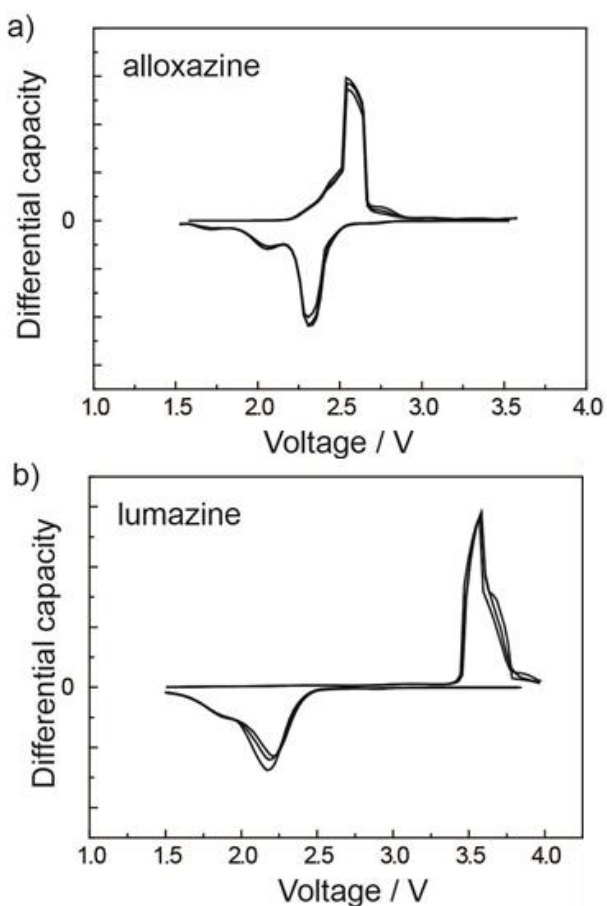


Figure 3.32. Differential capacity (dQ/dV) curves for alloxazine and lumazine electrodes. Two distinct steps of lithium-coupled single-electron transfer reaction occurred during redox reactions. Lumazine electrode shows larger polarization than alloxazine electrode.

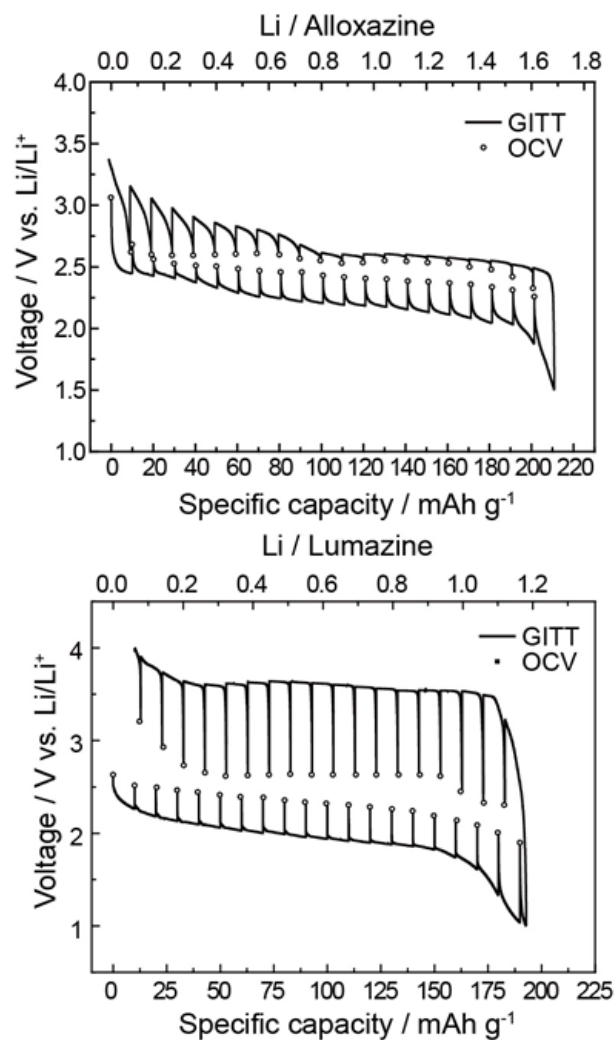


Figure 3.33. GITT profiles of the ALX/Li cells (top) and LMZ/Li cells (bottom).

In the absence of the anellated benzo ring, the small conjugated system of LMZ is likely to show less efficient accommodation of electrons and lithium ions at the diazabutadiene motif, thereby resulting in the large polarization. This suggests that in the molecular design of the organic electrode, the power density can be sacrificed to increase the energy density as the size of the molecule decreases. While the GITT measurement indicated that lithium insertion takes place at an average potential of 2.50 V and 2.20 V in the LMZ electrode, the large polarization makes it less appealing for practical batteries.

Enhanced battery performance with a modified electrode design

Another attractive aspect of pteridine derivative electrodes is that the electrochemical performance can be easily improved by employing a modified electrode preparation. Taking advantage of abundant electron clouds in *pi* orbitals of aromatic pteridines, graphitic nano-carbons can immobilize the molecules through strong *pi-pi* interaction which provide the redox centers with stable anchoring and a rapid electrical path. The simple solution-based process of mixing carbon nanotubes (CNTs) and organic powder followed by vacuum filtration produced highly conductive, free-standing paper, which is directly applicable as an additive-free electrode, in which the pteridine molecules were fixed onto the surface of CNTs (Figure 3.34).² As the result of the hybridization, the redox molecules are reassembled from crystalline particles to nanolayers on the surfaces of CNTs

losing their crystallinity (Figure 3.35). I found that the hybrid electrodes exhibited dramatically improved rate capability and cyclability without changes in redox potentials (Figure 3.36). The rate capabilities of the hybrid electrodes at different C rates are illustrated in Figure 3.37 and 3.38. At a current density of 220 mAh g⁻¹, which is equivalent to a 1C rate, the LC hybrid electrode showed a specific capacity of 215 mAh g⁻¹. Compared to the pristine electrodes made of powdered compounds, the charge/discharge profiles of hybrid electrodes are sloppier which is attributable to the reduced crystallinity and particle size of the active materials, as well as the extra capacity from CNTs (~18 mAh g⁻¹, Figure 3.39). Even at a high current density of 10.0 A g⁻¹ corresponding to a 45.5C rate, LC provided a specific capacity of 153 mAh g⁻¹, corresponding to 71.1% of the capacity at the 1C rate (Figure 3.37). The ALX hybrid electrode could deliver a specific capacity of 236 mAh g⁻¹ at the 1C rate (250 mA g⁻¹) and 168 mAh g⁻¹ at the 10C rate, as shown in Figure 3.38. Moreover, the LC and ALX hybrid electrodes showed remarkable capacity retentions compared to the pristine electrodes (Figure 3.40, Figure 3.41). After 200 cycles at 1.0 A g⁻¹ and 2.0 A g⁻¹, the LC hybrids showed 93% and 96% capacity retention, and the ALX hybrids showed 92% and 97% capacity retention, respectively. Even after cycling up to 500 times, the LC hybrid electrodes exhibited the capacity retention above 93% and 96% at a high rate of 5.0 A g⁻¹ and 10.0 A g⁻¹ (Figure 3.42), respectively. In addition, the ALX hybrid electrodes retained 93% and 91% of their initial capacity at 5.0 A g⁻¹ and 10.0 A g⁻¹, respectively.

To the best of our knowledge, the capacity retention of 96% up to 500 cycles at 10.0 A g^{-1} is the best and the longest cycling performance among the organic molecule-based cathode materials reported thus far.^{16,24-26}

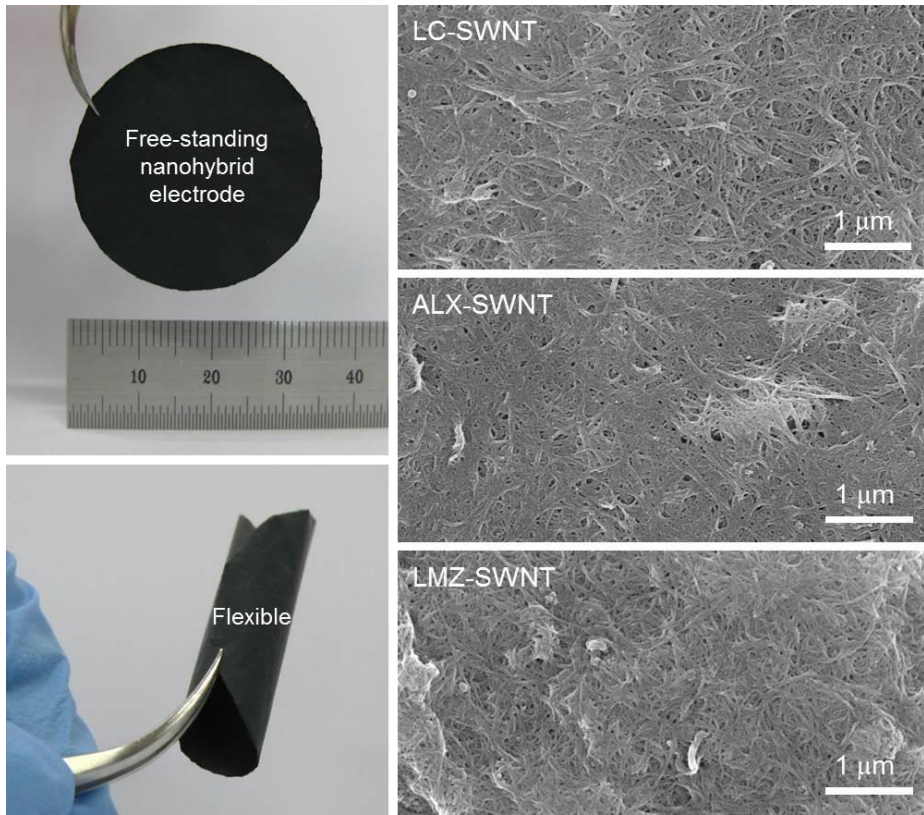


Figure 3.34. Photographs and SEM images for modified pteridine electrodes.

Free-standing and flexible films of pteridine-carbon nanotube hybrids were obtained. The particles of organic compounds were disassembled into molecular layer covering on the sidewalls of conductive carbon nanotubes. Detailed information on the hybrids of organic molecule and carbon nanotubes is described in ref 2.

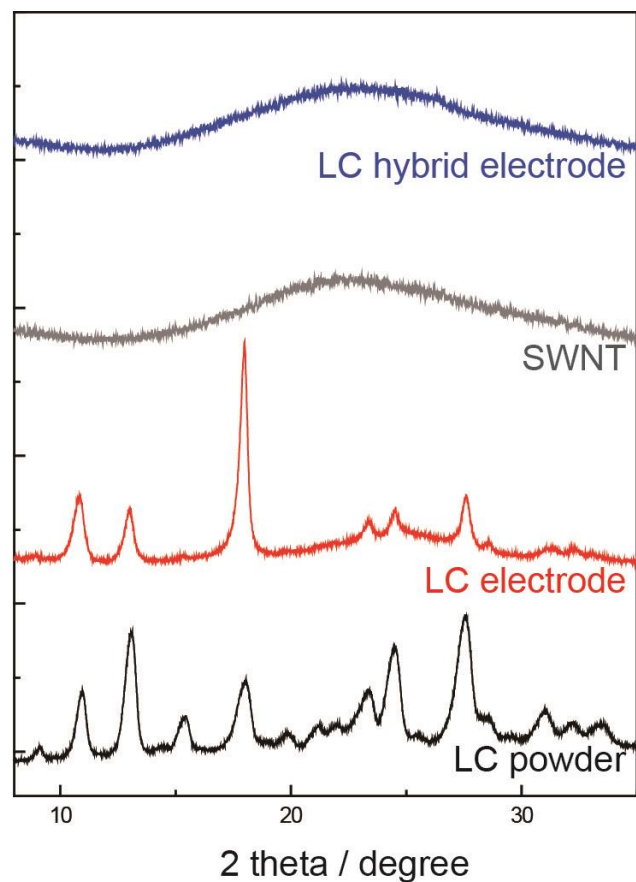


Figure 3.35. X-ray diffraction patterns of pristine LC powder, LC electrode made of PTFE and super P, SWNT film, and LC-SWNT hybrid electrode. LC loses its crystallinity by the hybridization with carbon nanotubes.

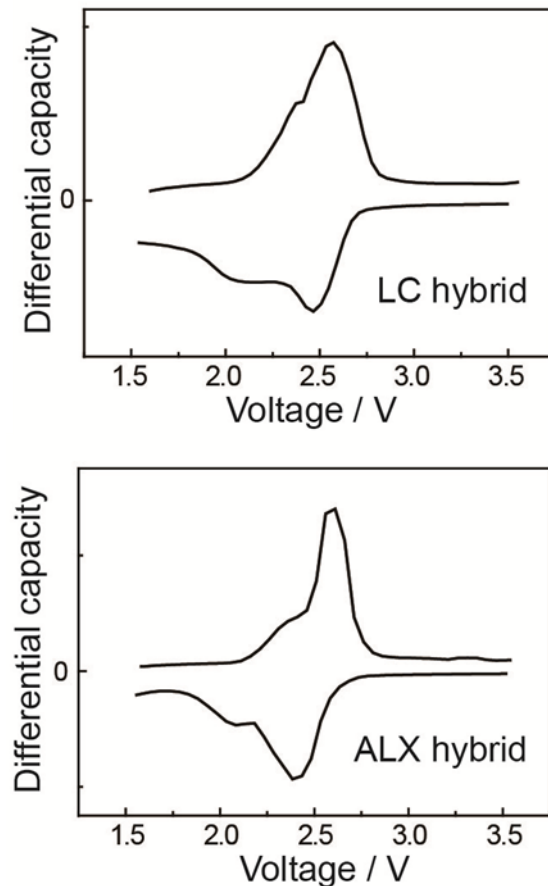


Figure 3.36. Differential capacity (dQ/dV) curves for LC and ALX hybrid electrodes. Two distinct steps of lithium-coupled single-electron transfer reaction occurred during redox reactions which is identical to the redox behavior of the pristine electrodes.

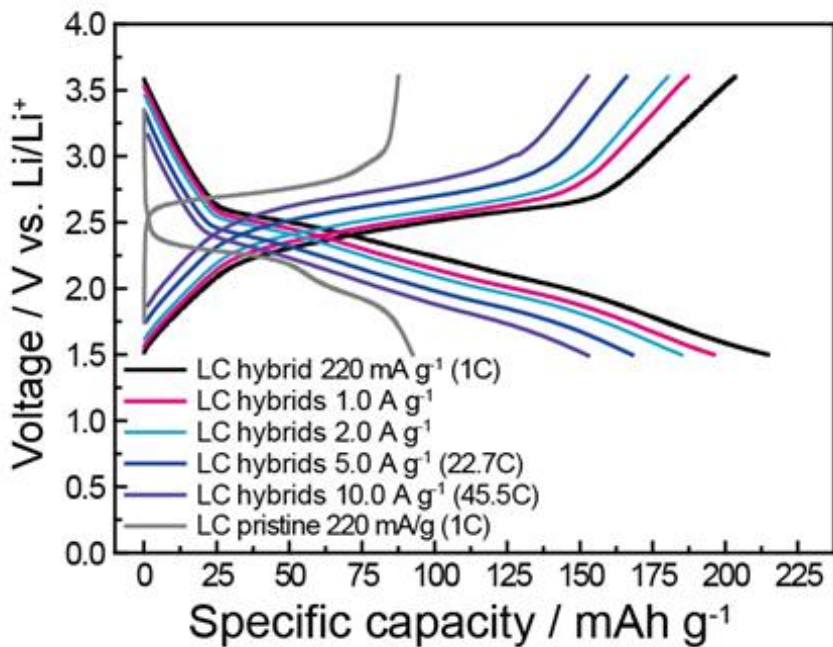


Figure 3.37. Capacity-voltage profiles of LC-CNT hybrid electrodes (LC hybrid) at various current rates and a pristine LC electrode at a 1C rate.

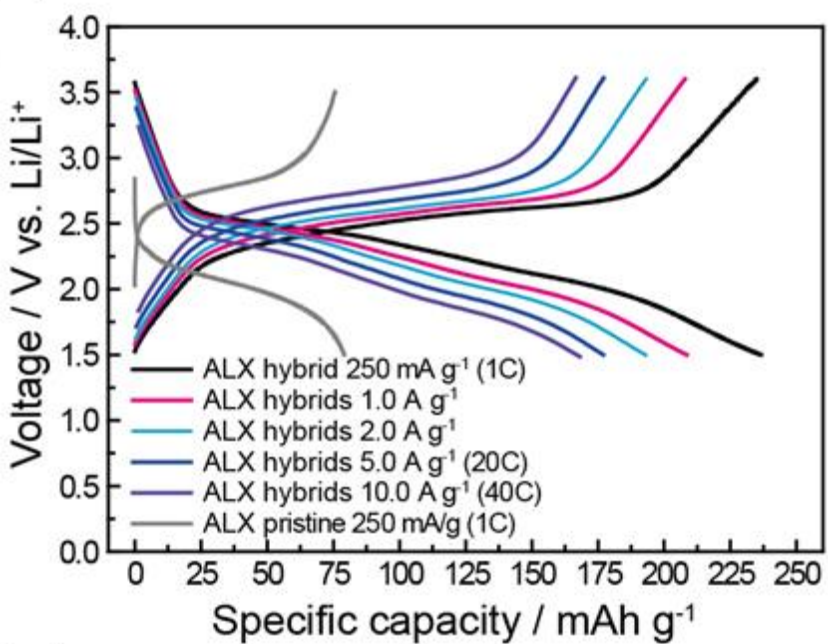


Figure 3.38. Capacity-voltage profiles of ALX-CNT hybrid electrodes (ALX hybrid) at various current rates and a pristine ALX electrode at a 1C rate.

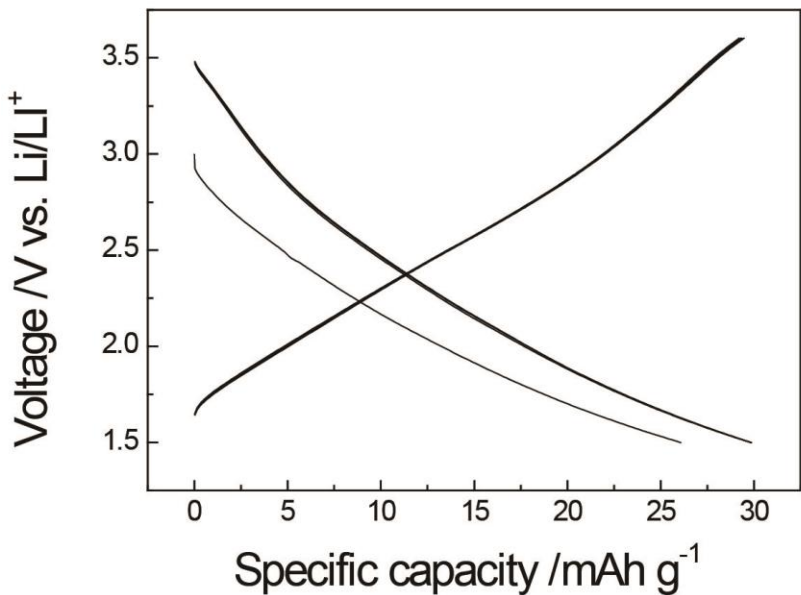


Figure 3.39. Capacity-voltage profile of the CNTs electrode without active materials at 250 mA g⁻¹. The CNTs electrodes show reversible capacity of 30 mAh g⁻¹ without notable decay.

Sodium storage in pteridine systems

As the limited abundance of lithium increases the need for alternative carrier ions in rechargeable battery systems,²⁷ I report that pteridine-based organic electrodes are also electrochemically active to sodium. As potential cathodes in sodium rechargeable batteries, we evaluated the electrochemical activity of pteridine derivatives to sodium using a half cell with sodium metal. Figure 3.43 shows that pteridine derivatives are capable of reversibly taking up and releasing two sodium ions, representing them as versatile electrodes in rechargeable batteries. In sodium batteries, LC and ALX exhibited a specific capacity of 138 and 168 mAh g⁻¹, respectively, and LMZ delivered a slightly lower capacity of 70 mAh g⁻¹ at a current density of 10.0 mA g⁻¹. By incorporating CNTs during electrode preparation, the deliverable capacities were significantly improved to 222, 255, and 220 mAh g⁻¹ even at 50.0 mA g⁻¹ for LC, ALX, and LMZ, respectively (Figure 3.44), although the capacity could not be stably retained during repeated cycling (approximately 50% retention after 20 cycles for all compounds). The limited cyclability could be attributable to the non-optimized Na electrolytes of the cell and the large strain of the electrode materials during the insertion of large sodium ions which may induce the isolation of the active materials from the electrodes.

While further studies are required, the sodium-organic battery system is promising for sustainable energy storage systems, since it is based on earth abundant sodium elements and does not contain transition metals.²⁸⁻³⁰ The utilization of the diazabutadiene redox cycling should provide potential

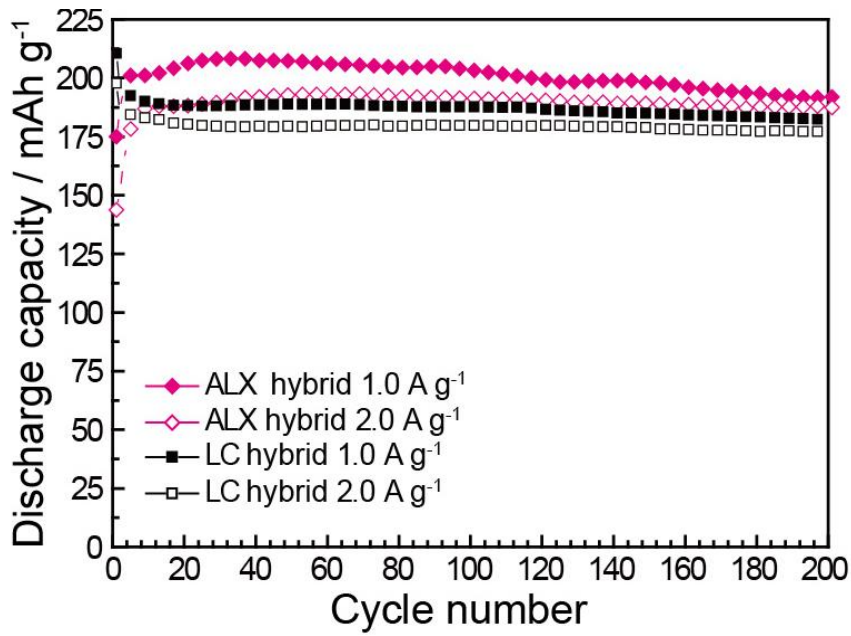


Figure 3.40. Capacity retention of the LC hybrid and ALX hybrid at 1.0 A g^{-1} and 2.0 A g^{-1} for 200 cycles.

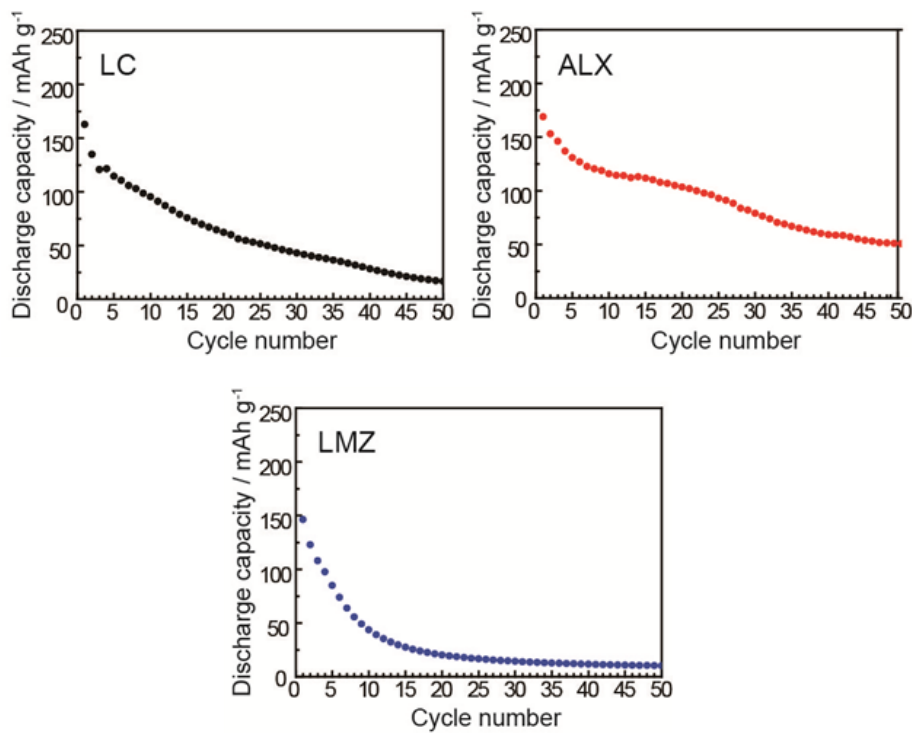


Figure 3.41. Capacity retentions of pristine electrodes of LC, ALX, and LMZ. The pristine electrodes show poor capacity retentions due to the dissolution of active materials into the organic liquid electrolytes.

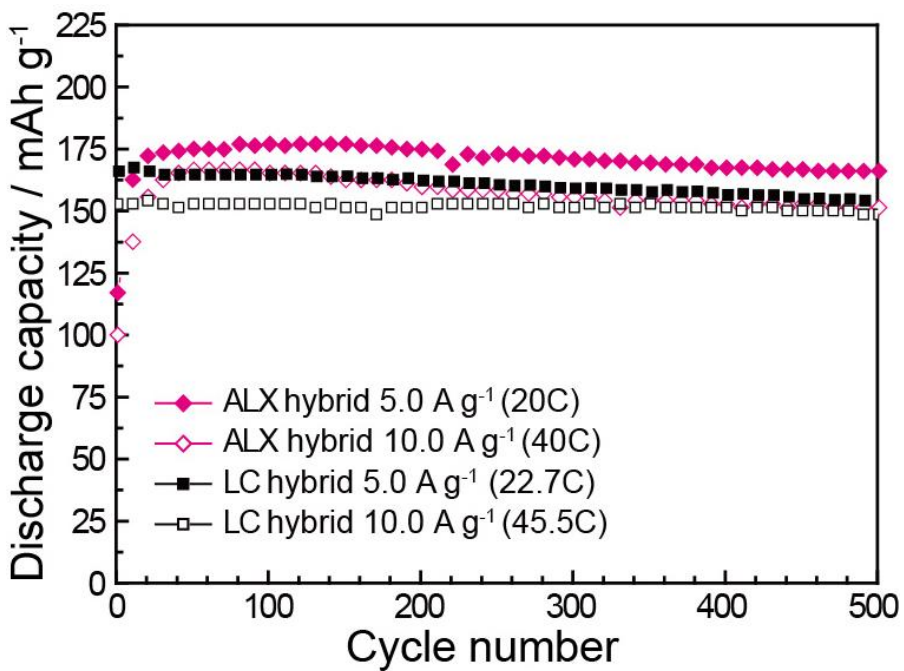


Figure 3.42. Capacity retention of the LC hybrid and ALX hybrid at 5.0 A g^{-1} and 10.0 A g^{-1} for 500 cycles.

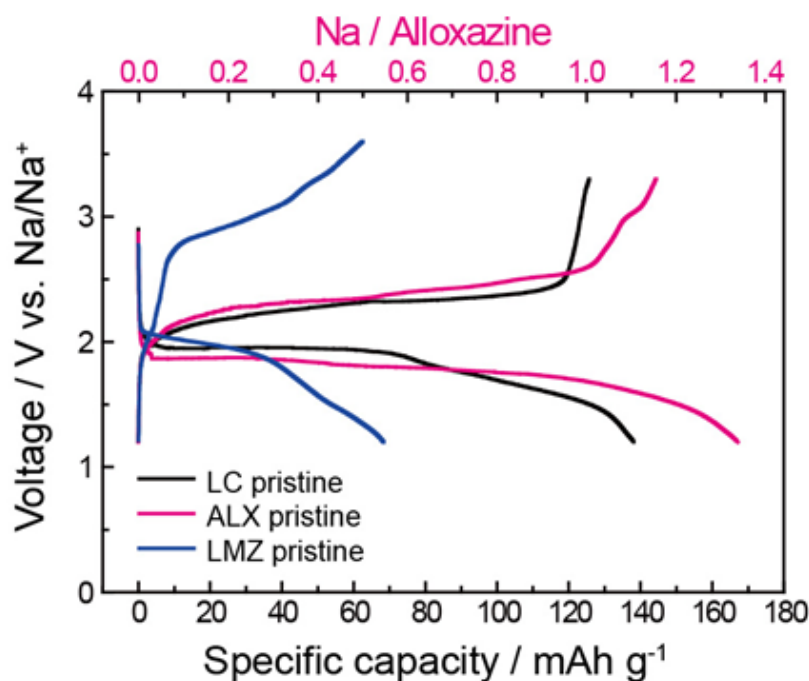


Figure 3.43. Capacity-voltage profiles of pristine pteridine derivatives at 20 mA g⁻¹ in sodium rechargeable batteries.

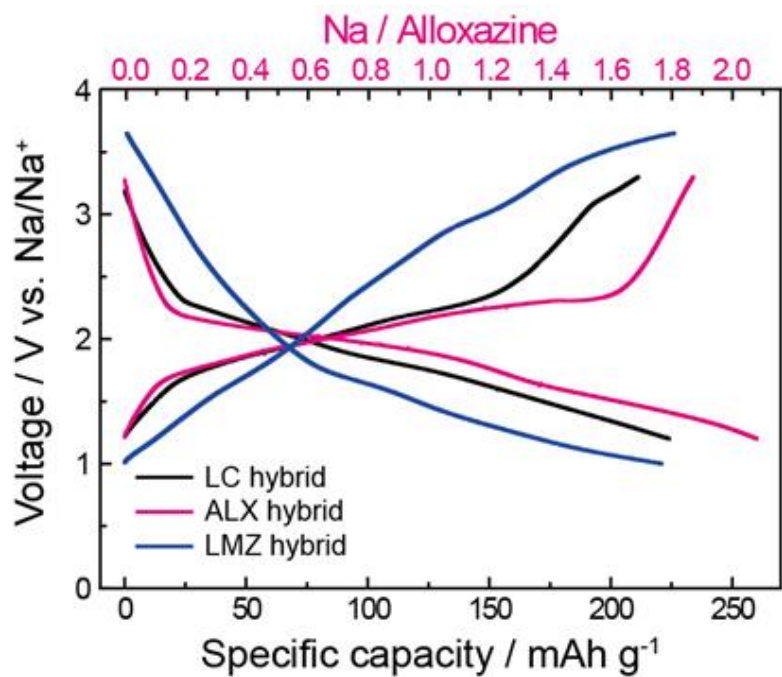


Figure 3.44. Capacity-voltage profiles pteridine hybrid electrodes at 50 mA g^{-1} in sodium rechargeable batteries.

opportunities for sodium-organic battery systems.

3.2.4. Conclusion

This chapter described a molecular simplification approach using tailored pteridine derivatives that contain redox-active diazabutadiene motif of flavins to develop green and high-performance energy storage systems. For the first time, reversible tautomerism between alloxazinic and isoalloxazinic structures in pteridine derivatives during lithium-coupled electron uptake and donation has been demonstrated through analyses of both *ex situ* characterizations and DFT calculations. The pteridine-based electrode having conductive CNT scaffolds exhibited high gravimetric energy density up to 533 Wh kg⁻¹ within 1-hour discharge, and even at the very high powers greater than 20 kW kg⁻¹, high gravimetric energy density of 348 Wh kg⁻¹ was demonstrated. Up to 96% of capacity was retained in the pteridine-based hybrid electrode after cycling for 500 times at 10.0 A g⁻¹, which is the best and longest cycling performance at such high rate among organic molecule-based cathode materials. Furthermore, the utilization of diazabutadiene redox cycling in sodium-ion batteries was first proposed, while more study is needed to overcome the capacity fading. The current study implies that various unexplored redox molecules from energy transduction systems in nature can offer unlimited opportunities to design sustainable electrodes with superior performances beyond the conventional electrode materials in rechargeable lithium/sodium ion batteries.

The thesis exploits biological pteridine derivatives of alloxazine structures as high-performance electrodes in rechargeable batteries. Combined *ex situ* spectroscopic analyses and density-functional theory-based calculations revealed that pteridine systems can store two lithium ions and two electrons *via* a reversible tautomerism between alloxazine and isoalloxazine forms. To the best of our knowledge, this is the first demonstration of a reversible tautomeric reaction of molecules during electrochemical reaction. By applying a molecular simplification strategy combined with in-depth analyses of the redox mechanism, the tailored pteridine electrodes showed outstanding performances, delivering 533 Wh kg⁻¹ of energy within 1 hour (236 mAh g⁻¹ ≈ 94.5% of theoretical capacity) and 348 Wh kg⁻¹ even within 1 minute with 96% capacity retention after 500 cycles, which is the best and longest cycling performance among the organic cathode materials reported at this time, and even comparable to state-of-the-art inorganic electrodes. Moreover, we demonstrate that redox cycling of the tailored pteridine electrodes is universally applicable to other energy storage systems with alternative carrier ions, *e.g.*, sodium rechargeable batteries.

Our results apply unexplored biological redox compounds in synthetic energy storage systems, and advance our understanding of their energy storage mechanisms. We believe that this manuscript suggests a general guidance to design high-performance sustainable batteries beyond conventional rechargeable batteries.

3.2.5. References

- 1 Lee, M. *et al.* Redox Cofactor from Biological Energy Transduction as Molecularly Tunable Energy-Storage Compound. *Angewandte Chemie International Edition* **52**, 8322-8328, doi:10.1002/anie.201301850 (2013).
- 2 Lee, M. *et al.* Organic Nanohybrids for Fast and Sustainable Energy Storage. *Adv Mater* **26**, 2558-2565, doi:10.1002/adma.201305005 (2014).
- 3 Sikorska, E. *et al.* Spectroscopy and Photophysics of Lumiflavins and Lumichromes. *The Journal of Physical Chemistry A* **108**, 1501-1508, doi:10.1021/jp037048u (2004).
- 4 Frisch, M. *et al.* Gaussian 09 Revision D. 01, 2009, Gaussian Inc. Wallingford CT.
- 5 Lee, C., Yang, W. & Parr, R. P. *Phys. Rev. B* 1988, **37**, 785–789; c) PJ Stephens, FJ Devlin, CF Chabalowski, MJ Frisch. *J. Phys. Chem* **98**, 11623-11627 (1994).
- 6 Becke, A. D. Density-functional thermochemistry. III. The role of exact exchange. *The Journal of Chemical Physics* **98**, 5648-5652 (1993).
- 7 Schäfer, A., Huber, C. & Ahlrichs, R. Fully optimized contracted Gaussian basis sets of triple zeta valence quality for atoms Li to Kr. *The Journal of Chemical Physics* **100**, 5829-5835 (1994).
- 8 Schäfer, A., Horn, H. & Ahlrichs, R. Fully optimized contracted Gaussian basis sets for atoms Li to Kr. *The Journal of Chemical Physics* **97**, 2571-2577, doi:doi:10.1063/1.463096 (1992).
- 9 Klaumünzer, B., Kröner, D. & Saalfrank, P. (TD-) DFT Calculation of Vibrational and Vibronic Spectra of Riboflavin in Solution. *The Journal of Physical Chemistry B* **114**, 10826-10834 (2010).

- 10 Mulliken, R. S. Electronic Population Analysis on LCAO-MO Molecular Wave Functions. I. *The Journal of Chemical Physics* **23**, 1833-1840, doi:doi:10.1063/1.1740588 (1955).
- 11 Sikorska, E. *et al.* Hydrogen-Bonded Complexes of Lumichrome. *The Journal of Physical Chemistry A* **109**, 1785-1794, doi:10.1021/jp045550o (2005).
- 12 Moyon, N. S. & Mitra, S. Fluorescence Solvatochromism in Lumichrome and Excited-State Tautomerization: A Combined Experimental and DFT Study. *The Journal of Physical Chemistry A* **115**, 2456-2464, doi:10.1021/jp1102687 (2011).
- 13 Sikorska, E. *et al.* Ground- and Excited-State Double Proton Transfer in Lumichrome/Acetic Acid System: Theoretical and Experimental Approach. *The Journal of Physical Chemistry A* **109**, 11707-11714, doi:10.1021/jp053951d (2005).
- 14 Vieira Ferreira, L. F. *et al.* Surface photochemistry: alloxazine within nanochannels of Na⁺ and H⁺ ZSM-5 zeolites. *Physical Chemistry Chemical Physics* **11**, 5762-5772, doi:10.1039/B903013A (2009).
- 15 Hernández-Burgos, K., Rodríguez-Calero, G. G., Zhou, W., Burkhardt, S. E. & Abruña, H. D. Increasing the Gravimetric Energy Density of Organic Based Secondary Battery Cathodes Using Small Radius Cations (Li⁺ and Mg²⁺). *Journal of the American Chemical Society* **135**, 14532-14535, doi:10.1021/ja407273c (2013).
- 16 Nokami, T. *et al.* Polymer-bound pyrene-4,5,9,10-tetraone for fast-charge and -discharge lithium-ion batteries with high capacity. *Journal of the American Chemical Society* **134**, 19694-19700, doi:10.1021/ja306663g (2012).
- 17 Castillo-Martínez, E., Carretero-González, J. & Armand, M. Polymeric Schiff Bases as Low-Voltage Redox Centers for Sodium-Ion Batteries. *Angewandte Chemie International Edition* **53**, 5341-

- 5345, doi:10.1002/anie.201402402 (2014).
- 18 Armand, M. *et al.* Conjugated dicarboxylate anodes for Li-ion batteries. *Nature Materials* **8**, 120-125 (2009).
- 19 Bhargava, G., Ramanarayanan, T. A. & Bernasek, S. L. Imidazole–Fe Interaction in an Aqueous Chloride Medium: Effect of Cathodic Reduction of the Native Oxide. *Langmuir* **26**, 215-219, doi:10.1021/la9020355 (2009).
- 20 Lee, T. H., Colton, R. J., White, M. G. & Rabalais, J. W. Electronic structure of hydrazoic acid and the azide ion from x-ray and ultraviolet electron spectroscopy. *Journal of the American Chemical Society* **97**, 4845-4851, doi:10.1021/ja00850a011 (1975).
- 21 Takahashi, M., Ishikawa, Y., Nishizawa, J.-i. & Ito, H. Low-frequency vibrational modes of riboflavin and related compounds. *Chemical Physics Letters* **401**, 475-482, doi:10.1016/j.cplett.2004.11.108 (2005).
- 22 Wolf, M. M. N., Schumann, C., Gross, R., Domratcheva, T. & Diller, R. Ultrafast Infrared Spectroscopy of Riboflavin: Dynamics, Electronic Structure, and Vibrational Mode Analysis. *The Journal of Physical Chemistry B* **112**, 13424-13432, doi:10.1021/jp804231c (2008).
- 23 Liang, Y., Zhang, P. & Chen, J. Function-oriented design of conjugated carbonyl compound electrodes for high energy lithium batteries. *Chemical Science* **4**, 1330-1337, doi:10.1039/C3SC22093A (2013).
- 24 Song, Z. *et al.* Polymer-graphene nanocomposites as ultrafast-charge and -discharge cathodes for rechargeable lithium batteries. *Nano letters* **12**, 2205-2211, doi:10.1021/nl2039666 (2012).
- 25 Huang, W. *et al.* Quasi-Solid-State Rechargeable Lithium-Ion Batteries with a Calix[4]quinone Cathode and Gel Polymer Electrolyte. *Angewandte Chemie* **125**, 9332-9336,

- doi:10.1002/ange.201302586 (2013).
- 26 Wu, H. *et al.* Flexible and Binder-Free Organic Cathode for High-Performance Lithium-Ion Batteries. *Adv Mater* **26**, 3338-3343, doi:10.1002/adma.201305452 (2014).
- 27 Kim, S.-W., Seo, D.-H., Ma, X., Ceder, G. & Kang, K. Electrode Materials for Rechargeable Sodium-Ion Batteries: Potential Alternatives to Current Lithium-Ion Batteries. *Advanced Energy Materials* **2**, 710-721, doi:10.1002/aenm.201200026 (2012).
- 28 Yao, M. *et al.* Indigo carmine: An organic crystal as a positive-electrode material for rechargeable sodium batteries. *Sci. Rep.* **4**, doi:10.1038/srep03650 (2014).
- 29 Sakaushi, K. *et al.* Aromatic porous-honeycomb electrodes for a sodium-organic energy storage device. *Nat Commun* **4**, 1485, doi: 10.1038/ncomms2481 (2013).
- 30 Wang, S. *et al.* All organic sodium-ion batteries with $\text{Na}_4\text{C}_8\text{H}_2\text{O}_6$. *Angewandte Chemie*, 126, 6002-6006, doi:10.1002/ange.201400032 (2014).

Chapter 4. Conclusion

In the continuous scientific efforts to explore new cathode materials that can substitute current cathode materials including LiCoO_2 and LiFePO_4 , in this thesis, two types of high-capacity cathode materials for next-generation lithium rechargeable batteries were studied: Layered Li-excess transition metal oxides and transition metal-free organic compounds containing pteridine redox center. Both classes of materials have attracted a great attention to the material scientists due to their excellent properties and potentials such as high-capacity and energy density exceeding those of commercially available electrode materials. However, their energy storage mechanisms have not been clearly understood, which limits their practical applications. Thus, I performed in-depth study by using combined experiments and DFT calculations to investigate the underlying energy storage mechanisms and reactions of both classes of electrode materials.

In case of the layered Li-excess compounds, I revealed the detailed reactions which take place at both surface and the bulk of the active materials during the electrochemical cycling. First, in chapter 2.1, I found that the oxygen evolution from the layered Li-excess transition metal oxides plays a critical role in lithium rechargeable battery system. The evolved oxygen is reduced to oxygen radicals that decompose the electrolytes into lithium carbonate and other acidic species. The formed lithium carbonate

participates in the reversible electrochemical reactions at the surface of active materials and the acidic byproducts damages the surface of active materials inducing the manganese dissolution into the electrolyte which deteriorate the electrochemical properties of the layered Li-excess materials such as rate capability and cycle stability. In chapter 2.2, I revealed the structural evolution of the bulk region of the layered Li-excess nickel-manganese oxide. The systematic study was performed which compared the electrochemical properties and the related structural evolution of three different Li-excess nickel-manganese oxides with altered composition. I found that the chemical composition (the ration of nickel to manganese) is a critical factor that determines the voltage decay of the layered Li-excess nickel-manganese oxides during repeated electrochemical cycling. This result proposes that the compositional alteration by substituting manganese into other transition metal species is effective to suppress the voltage decay problem and increase the energy density.

In case of the high-capacity organic compounds, we developed a novel class organic active compound by the inspiration from biological energy transduction. Here, I report a novel class of biological redox units as a high performance battery electrode, namely, pteridine redox centers, which are essential constituents in cellular energy metabolism, along with the effective strategy for tailoring these biological redox units to achieve excellent electrochemical performances. The combined *ex situ* spectroscopic analyses and density-functional theory-based calculations revealed that pteridine

systems can store two lithium ions and two electrons *via* a reversible tautomerism between alloxazine and isoalloxazine forms. By applying a molecular simplification strategy combined with in-depth analyses of the redox mechanism, the tailored pteridine electrodes showed outstanding performances, delivering 533 Wh kg⁻¹ of energy within 1 hour (236 mAh g⁻¹ ≈ 94.5% of theoretical capacity) and 348 Wh kg⁻¹ even within 1 minute with 96% capacity retention after 500 cycles, which is the best and longest cycling performance among the organic cathode materials reported at this time, and even comparable to state-of-the-art inorganic electrodes.

For the practical applications of the high-capacity materials such as the layered Li-excess transition metal oxides and organic pteridine compounds, some problems should be solved. For example, the rate capability and cycle stability of the layered Li-excess transition metal oxides need to be improved. The combined strategy of protecting the surface of active materials by coating conductive and stable polymer and tailoring chemical composition could be applied to address the present challenges. In case of organic compound cathodes, the synthesis of lithium containing active compounds which can be charged at the pristine state should be accomplished. Moreover, the contents of active materials in the electrode also need to be increased. The development of p-type organic compounds with high conductivity which can accommodate anion by charge process might be an effective solution.

While this thesis cannot solve all the challenges and questions on the way

to the practical applications of the two types of promising alternative cathode materials, I believe that this thesis can contribute to improve the scientific understanding on the intrinsic properties and the unveiled reactions of the high-capacity electrode materials in the energy storage devices. Based on the results documented in this thesis, I hope that the practical applications of the layered Li-excess materials and biologically inspired organic compounds could be realized in the near future.

Chapter 5. Abstract in Korean

리튬 이차전지는 타 에너지 저장 소재보다 높은 밀도로 에너지를 저장할 수 있어 오늘날 대부분의 휴대용 전자기기의 전원 공급장치로 이용되고 있다. 최근에는 리튬 이차전지의 응용 범위가 대용량 장치인 전기자동차 및 대용량 전력 저장장치로 점차 확대되어 가고 있다. 그러나 현재 수준에서 상용화되어 있는 리튬 이차전지는 대용량 장치들의 전원을 공급하기에는 에너지 밀도, 가격, 수명 특성, 안정성 등의 특성이 필요 조건을 충족 시키지 못하고 있다. 이에 따라, 현재 사용되고 있는 리튬 코발트 산화물이나 리튬 철 인산염 양극 소재를 대체하는 새로운 양극 소재를 개발하려는 노력이 지속적으로 이루어지고 있다.

그 동안 개발된 다양한 양극 소재들 중, 층상 구조의 리튬 과잉 전이금속 산화물과 유기 화합물 기반의 양극 소재가 높은 용량과 에너지 밀도로 크게 각광받고 있다. 그러나 이 소재들의 높은 에너지 밀도에도 불구하고 여전히 에너지 저장 기작이 명확히 밝혀지지 않았고 소재 자체의 특성에 대한 이해가 깊지 않아 이러한 전극 소재들의 전기 화학 특성을 근본적으로 향상시키는데 어려움을 겪고 있다. 이러한 측면에서, 본 논문에서는 실험과 제일 원리 계산을 이용한 심도 깊은 연구를 통하여 이 두 가지 고용량 전극 소재의 에너지 저장 기작을 규명한다. 더 나아가, 이러한 이해를 바탕으로 소재의 전기화학 특성을 개선하는 전략을 제시한다.

충상구조의 리튬 과잉 전이금속 산화물은 230 mAh g^{-1} 가 넘는 매우 높은 용량 특성을 나타낸다. 이러한 높은 용량은 소재의 사용 가능한 산화/환원 작용을 모두 이용한다고 가정했을 때 계산한 이론 용량보다 훨씬 큰 값이다. 이러한 용량은 소재를 4.5 ~ 4.6 V에서 나타나는 평탄 전위 구간 이상으로 충전 시켰을 경우에 산소 기체가 발생하고 나면 가역적으로 나타난다. 더욱이 이 소재는 큰 용량으로 충전 및 방전이 거듭 진행되는 도중에 평균 전압이 점점 감소하는 특성을 보인다. 그러나 이때 발생한 산소가 리튬 이차전지 내부에서 어떠한 영향을 미치는지 명확한 규명이 되지 않았으며, 전압 강하의 원인 또한 명확히 규명되지 않았다. 본 논문에서는 충상구조 리튬 과잉 전이금속 산화물의 충전 시 발생한 산소가 리튬 이차전지 내부에서 어떠한 역할을 하는지 규명하고 그 때 발생하는 전기화학 감소를 막는 방법에 대해 간단히 소개한다. 또한 충상구조 리튬 과잉 전이금속 산화물의 전압 강하와 화학적 조성의 상관관계를 밝히고 조성의 최적화를 통한 전압 강하 방지에 대한 연구 결과를 소개하였다.

유기 화합물은 무거운 전이금속을 포함하고 있지 않고 여러 개의 전자를 주고 받을 수 있는 능력을 갖고 있어 높은 용량을 가져 잠재적인 미래형 양극 소재로 주목 받고 있다. 본 연구에서는 자연계에 존재하는 생명체의 에너지 대사 시스템으로부터 영감을 받아 새로운 종류의 유기물 전극 소재를 개발하였다. 프테리딘 (pteridine) 산화/환원 센터를 포함하는 친환경 양극 소재인 플라빈 (flavin) 소재들을 새로운 양극 소재로 제시하고 이 종류의

소재들의 에너지 저장 기작을 밝혔다. 더 나아가 제일 원리 계산을 통하여 프테리딘 단위체를 포함하는 보다 단순한 유기 화합물인 알록사진과 루마진을 디자인하였고 이를 실험으로 구현하였다. 마지막으로 이러한 생체 기반의 유기 화합물 전극 소재의 출력 특성과 수명 특성을 획기적으로 향상시키는 방법을 제시하였다.